Dedicated to:

This dissertation is dedicated to my late parents, my beloved mother and father, whose memory remains a constant source of strength and inspiration.
To my family and friends, thank you for your enduring support and belief in me.
I further dedicate this work to the humanitarians who devote their lives to improving the conditions of the less fortunate.

DEPARTMENT OF MATERIALS TECHNOLOGIES

FACULTY OF MATERIALS ENGINEERING AND DIGITALISATION OF INDUSTRY

Doctoral Thesis

Hot corrosion behaviour of a new type of thermal barrier coating materials

Muhammad Jahangir Khan, M.Sc.

Supervisor:

Dr hab. inż. Grzegorz Moskal, prof. of SUT, Silesian University of Technology, Poland

Co- Supervisor:

Dr inż. Marta Mikuskiewicz, Silesian University of Technology, Poland

Katowice, 2026

Acknowledgement

I would like to express my sincere gratitude to my supervisor, **Prof. Grzegorz Moskal**, and my co-supervisor, **Dr. Marta Mikuśkiewicz**, for their invaluable guidance, continuous support, and constructive feedback throughout the course of my doctoral studies. Their expertise and encouragement have been essential in shaping the quality and direction of this research.

I am also grateful to **Prof. Amirhossein Pakseresht** for his collaboration and valuable contributions during the project, which have significantly enriched this work.

Acronyms

TBCs	Thermal Barrier Coating Systems
APS	Atmospheric Plasma Spray
BC	Bond Coat
TC	Top Coat
TGO	Thermally Grown Oxide
CTE	Coefficient of Thermal Expansion
TCF	Thermal Cycling Fatigue
CMAS	Calcia-Magnesia-Alumino-Silicate
EB-PVD	Electron Beam Physical Vapor Deposition
PS-PVD	Plasma Spray Physical Vapour Deposition
HVOF	High Velocity Oxy Fuel
SPS	Solution Plasma Spraying
YSZ	Yttria-Stabilized Zirconia
NZO	Neodymium zirconate
NCO	Neodymium Create
XRD	X-ray Diffraction
SEM	Scanning Electron Microscope
EDS	Energy Dispersive X-ray Spectroscopy
PSD	Particle Size Distribution

List of Published Articles

1. Khan, M. J., Moskal, G., Pakseresht, A., Parchoviansky, M., & Pęcak, K. (2025). Complex sulphate vanadate salt induced hot corrosion and thermal shock performance of $Nd_2Zr_2O_7$ + 8YSZ composite thermal barrier coating system. *Ceramics International, 51*(24B), 42551–42564. https://doi.org/10.1016/j.ceramint.2025.07.001
2. Khan Muhammad Jahangir, Moskal Grzegorz, Iqbal Amjad *[et al.],* Coatings, 2023, vol. 13, no. 8, pp.1-14, Article number:1311. Go to the document by digital IDDOI:10.3390/coatings13081311
3. Khan Muhammad Jahangir, In: Interdyscyplinarne badania młodych naukowców / Balon Barbara (*eds.*), Monografia / Politechnika Śląska, 2024, no. 1045, Wydawnictwo Politechniki Śląskiej, pp.239-250, ISBN 978-83-7880-983-8.
4. Khan Muhammad Jahangir, Iqbal Amjad, Moskal Grzegorz, In: Interdyscyplinarne badania młodych naukowców / Balon Barbara (*eds.*), Monografia / Politechnika Śląska, 2023, no. 987, Wydawnictwo Politechniki Śląskiej, pp.223-231, ISBN 978-83-7880-905-0.
5. Iqbal, A., Moskal, G., Cavaleiro, A., Amjad, A., & Khan, M. J. (2024). The current advancement of zirconate-based dual-phase systems in thermal barrier coatings (TBCs): New modes of the failures: Understanding and investigations. *Alexandria Engineering Journal, 91*, 161–196. https://doi.org/10.1016/j.aej.2024.01.063
6. Iqbal Amjad, Khan Muhammad Jahangir, In: Materiały i technologie XXI wieku : XXIV Międzynarodowa studencka sesja konferencja naukowa, Katowice, 24 maj 2023. Książka abstraktów / Maciąg Tomasz (*eds.*), 2023, pp.9-9.

Streszczenie

Przedstawiona praca dotyczy problemu odporności na korozję wysokotemperaturową powłokowych barier cieplnych na bazie cyrkonianów $Nd_2Zr_2O_7$ (powłoki jednofazowe), oraz powłok kompozytowych typu $Nd_2Zr_2O_7$+8YSZ i $Nd_2Ce_2O_7$+8YSZ, w środowiskach zawierających ciekłe osady solne na bazie siarczanów sodu i magnezu oraz pięciotlenku dwuwanadu,

Przeprowadzone badania wykazały, że odporność badanych systemów powłokowych na korozję w środowisku ciekłych osadów Na_2SO_4 jest zadowalająca w przypadku powłoki $Nd_2Zr_2O_7$. Wprowadzenie dodatkowej soli $MgSO_4$ powoduje intensyfikację procesów niszczenia korozyjnego, co wynika z powstawania eutektyk solnych o niższej temperaturze topnienia niż Na_2SO_4. Wprowadzenie do układu tlenku V_2O_5 gwałtownie przyspieszy proces niszczenia korozyjnego, co związane z tworzeniem się wanadianów neodymu. Ze względu na intensywność procesów korozyjnych badana powłoka uległa destrukcji i całkowitemu odpadnięciu od podłoża na bazie stopu IN-625.

Celem zwiększenia trwałości systemów TBC, dalszym badaniom poddano bariery o charakterze kompozytowym typu $Nd_2Zr_2O_7$+ 8YSZ, które w założeniu miały wykazywać większą ogólna trwałość na oddziaływanie agresywnego środowiska korozyjnego. Analizy wykazały, że zmodyfikowany system $Nd_2Zr_2O_7$+ 8YSZ nie wykazywał skłonności do odpadania w trakcie przeprowadzonych testów odporności korozyjnej. Badania w środowisku ciekłych osadów Na_2SO_4 oraz Na_2SO_4 + $MgSO_4$ wykazały zjawisko dekompozycji fazy pirochlorowej $Nd_2Zr_2O_7$ do form niestechiometrycznych faz fluorytowych, co jest efektem bądź zubożenia fazy pirochlorowej w tlenek Nd_2O_3, bądź wprowadzenia do pirochloru tlenku Y_2O_3. Spowodowało to zmniejszenie wartości stosunku średniego promienia kationów neodymu i itru w stosunku do promienia kationów cyrkonu do zakresu odpowiadającego stabilności fazy fluorytowej. Wprowadzenie do środowisku tlenku V_2O_5 spowodowało tworzenie się wanadianów neodymu oraz itru, co dodatkowo spowodowało tworzenie się monoklinicznego tlenku ZrO_2.

W przypadku powłoki kompozytowej na bazie cerianu neodymu, przeprowadzone analizy wykazały, że wytworzone systemy charakteryzują się wysoka stabilnością fazową. Nie obserwowano efektu dekompozycji sieci fluorytu $Nd_2Ce_2O_7$ do form niestechiometrycznych. Głównym objawem przebiegu procesów korozyjnych było tworzenie się oksysiarczanów neodymu. W przypadku obecności tlenku V_2O_5, stwierdzono produkty interakcji w postaci wanadianów neodymu oraz zubożone w tlenek neodymu ceriany $Nd_{0.4}Ce_{0.6}O_{1.8}$.

Abstract

This work addresses the problem of high-temperature corrosion resistance in environments containing liquid salts based on sodium and magnesium sulfates, as well as vanadium pentoxide. It also explores thermal barrier coatings based on $Nd_2Zr_2O_7$ zirconates (single-phase coatings) and composite coatings of the $Nd_2Zr_2O_7$+8YSZ and $Nd_2Ce_2O_7$+8YSZ types.

The conducted studies demonstrated that the corrosion resistance of the tested coating systems in a liquid Na_2SO_4 environment is satisfactory for the $Nd_2Zr_2O_7$ coating. The addition of the $MgSO_4$ salt intensifies the corrosion processes, which result from the formation of salt eutectics with a lower melting point than Na_2SO_4. The introduction of V_2O_5 oxide to the system dramatically increases the corrosion process, associated with the formation of neodymium vanadate. Due to the intense corrosion processes, the tested coating cracked and completely fell off the IN-625 alloy-based substrate.

To increase the durability of the TBC systems, further testing was performed on $Nd_2Zr_2O_7$ + 8YSZ composite barriers, which were intended to demonstrate greater overall durability against aggressive corrosive environments. Analyses showed that the modified $Nd_2Zr_2O_7$ + 8YSZ system did not exhibit any tendency to fall off during the corrosion resistance tests. Tests in liquid Na_2SO_4 and Na_2SO_4 + $MgSO_4$ deposits revealed the decomposition of the $Nd_2Zr_2O_7$ pyrochlore phase into non-stoichiometric fluorite phases, which is the result of either the depletion of the pyrochlore phase in Nd_2O_3 oxide or the introduction of Y_2O_3 oxide into the pyrochlore. This resulted in a reduction in the ratio of the average radius of the neodymium and yttrium cations to the radius of the zirconium cations to the range corresponding to the stability of the fluorite phase. The introduction of V_2O_5 oxide into the environment resulted in the formation of neodymium and yttrium vanadate, which additionally resulted in the formation of monoclinic ZrO_2 oxide.

For the second type of composite coating based on neodymium cerate, the analyses conducted showed that the resulting systems were characterized by high phase stability. No decomposition of the $Nd_2Ce_2O_7$ fluorite network into non-stoichiometric forms was observed. The main symptom of the corrosion process was the formation of neodymium oxysulphates. In the presence of V_2O_5 oxide, interaction products in the form of neodymium vanadate and neodymium oxide-depleted $Nd_{0.4}Ce_{0.6}O_{1.8}$ cerates were observed.

Table of Contents

List of Figures

List of Tables

Chapter 1: Overview

1.1 Background and Significance of Thermal Barrier Coatings (TBCs)

The need for greater efficiency and extended service life of components subjected to extreme conditions has had far-reaching impacts on the study of materials in manufacturing industries of all types, including aerospace, power generation, and nuclear power. The degradation of structural materials under the influence of high temperature, oxidative and corrosive environments, and thermal cycling results in degradation mechanisms which pose a challenge to the reliability of engineering systems. As service temperatures increase, these thermally activated degradation processes also increase, thus necessitating the design of durable protection strategies. One of the most practical and widely adopted approaches to mitigate these challenges is the application of thermal barrier coatings (TBCs), which provide thermal insulation and environmental protection for structural substrates used in turbines, reactors, and engine components.

Thermal barrier coatings (TBCs), a form of ceramic coatings, are widely used to protect structural materials in gas turbines, nuclear power plants, and other high-temperature systems. TBCs not only restrict heat loss from the environment into the substrate, thus ensuring greater thermal efficiency, but also help sustain lower temperatures within the substrate, thereby allowing for increased operating temperatures. TBCs for combustion engines and power plants are available for use in future nuclear technologies. High-ranking temperature materials and advanced, robust high-temperature coatings must be developed. Over the past few decades, thermal barrier coatings (TBCs) have been under consideration, and critical research has enabled researchers and industries to build superior-quality multilayer TBC coatings that are more promising than conventional mono-layer ceramic coatings.

YSZ (Yttria-Stabilised Zirconia) has been the benchmark ceramic for TBCs due to its low thermal conductivity, phase stability, and transformation toughening. However, it is known to become unstable and unreliable at temperatures above 1200°C due to phase transformations and sintering effects. To overcome these limitations, other materials, such as pyrochlores (RE2Zr2O7), perovskites (LaTi2Al9O19), monazite (LaPO4), and garnets (Y3Al5O12), have been investigated for their high-temperature stability, lower thermal conductivity, and improved phase retention.

In modern engineering applications, especially in gas turbines and nuclear reactors, the use of thermal barrier coatings (TBCs) is essential not only for thermal insulation but also for protection against hot corrosion caused by molten salts such as Na_2SO_4 and V_2O_5. These

aggressive species compromise the integrity of the protective oxide scales and accelerate the degradation of the coating system. Interfaces between the topcoat of the ceramic and the thermally grown oxide (TGO) or bond coat, which is often used, are usually the starting point of degradation, leading to delamination, spallation, or the extension of microcracks under cyclic oxidation or mechanical load**s.**

1.2 Structure of the Thesis

The findings of the present work are organised in chapters.

In Chapter I, Background and Significance of Thermal Barrier Coatings (TBCs), and report outline were reviewed.

Chapter II presents a literature review that addresses a brief introduction to TBCs and their applications, advanced TBC materials, deposition techniques, and different degradation mechanisms.

Chapter III: Materials and Methods. This chapter describes the materials used and the experimental methods employed to evaluate the performance, structure, and degradation behaviour of thermal barrier coatings.

Chapter IV Thesis and Objectives of the Work present the thesis statement and research objectives, highlighting the knowledge gaps in two-phase composite TBCs. It introduces the hypothesis regarding enhanced corrosion resistance of $Nd_2Zr_2O_7$ + 8YSZ and $Nd_2Ce_2O_7$ + 8YSZ systems. The chapter outlines the planned corrosion studies and phase analyses, and defines the key goals focused on understanding durability, microstructural changes, and degradation mechanisms.

Chapter V Effect of Molten Sulfate and Vanadate Salts on the Hot Corrosion Behaviour of Single-Layered $Nd_2Zr_2O_7$ Thermal Barrier Coatings. It presents the phase evolution, microstructural changes, and degradation processes observed under Na_2SO_4, Na_2SO_4–$MgSO_4$, and Na_2SO_4–V_2O_5 deposits. The chapter outlines the reactions responsible for coating instability and identifies the corrosion products formed. It also examines the deterioration pathways that govern coating performance in aggressive salt conditions.

Chapter VI presents the study of complex sulphate vanadate induced hot corrosion of the $Nd_2Zr_2O_7$ + 8YSZ composite thermal barrier coating system. It introduces the corrosion behaviour of the as-sprayed coatings and examines their phase composition and microstructural evolution under molten Na_2SO_4, Na_2SO_4–$MgSO_4$, and Na_2SO_4–V_2O_5 environments. The chapter outlines the degradation mechanisms, the formation of non-stoichiometric fluorite compounds, and the influence of vanadium-containing salts on coating stability. It further

details the development of corrosion products, microcracks, and voids, providing insight into the failure pathways of the composite system.

Chapter VII presents the hot corrosion behaviour of the $Nd_2Ce_2O_7$ + 8YSZ composite thermal barrier coating in molten Na_2SO_4, Na_2SO_4–$MgSO_4$, and Na_2SO_4–V_2O_5 environments. It introduces the phase stability, surface reactions, and microstructural degradation observed at 920 °C, supported by XRD, SEM, and EDS analyses. The chapter outlines the evolution of corrosion products, the response of the dual-phase fluorite–YSZ structure, and the contrasting effects of sulfate versus vanadate attack.

Chapter VIII: Conclusion and future work

Chapter 2: Introduction

2.1 Thermal Barrier Coating System

Thermal barrier coatings (TBCs) are advanced, multilayer ceramic coatings engineered to protect metallic components from extreme thermal and chemical environments. These systems are essential in modern high-temperature systems, such as aeroplane gas turbines, industrial power generation turbines, automotive engines, and advanced nuclear reactors. The TBCs eliminate or lower the operating temperature of the underlying metallic component by providing a thermal insulation layer between the hot gas stream and the metal, which consequently increases the component's life, decreases oxidation, and improves energy efficiency **[1-2]**.

A TBC system consists of a metallic substrate (typically a nickel-based superalloy) with a bond coat, an intermediate thermally grown oxide (TGO) layer on top, and a ceramic topcoat. These layers act in synergy to create thermal insulation, allow for thermal expansion differences, and protect against hot corrosion and high-temperature oxidation. The substrate forms the load-bearing base, while the bond coat—commonly made of MCrAlY alloys (where M = Ni, Co, or both) enhances adhesion and acts as a reservoir for oxidation-resistant elements, particularly aluminium. When subjected to high temperatures, a thin and stable alumina (Al_2O_3) film forms at the interface, known as the TGO **[3-5]**. The oxide coating serves as a diffusion barrier, restricting both the influx of oxygen and the outward movement of metal ions. The topcoat is a ceramic composed of yttria-stabilised zirconia (YSZ), which is a low thermal conductor with a high melting temperature and thermal shock resistance. These properties, combined, enable surface temperature reductions of 150-300 °C on key engine components **[6]**.

The multi-layered design of TBCs ensures that the components can withstand thermal gradients, cyclic fatigue, and corrosive atmospheres standard in high-performance turbines and propulsion systems **[7]**. The TBC structure incorporates all these layers into a functional coating, as shown in Fig. 2.1, which insulates and protects the underlying metal in the event of prolonged exposure to combustion gases. In addition to the material used, the microstructural design and integrity of the interfaces between the layers also play a role in the performance of a TBC system. Properly designed TBCs allow for prolonging the service life and reducing the maintenance expenses, as well as increasing the thermal loads, making stable, clean, and efficient energy systems more likely to happen.

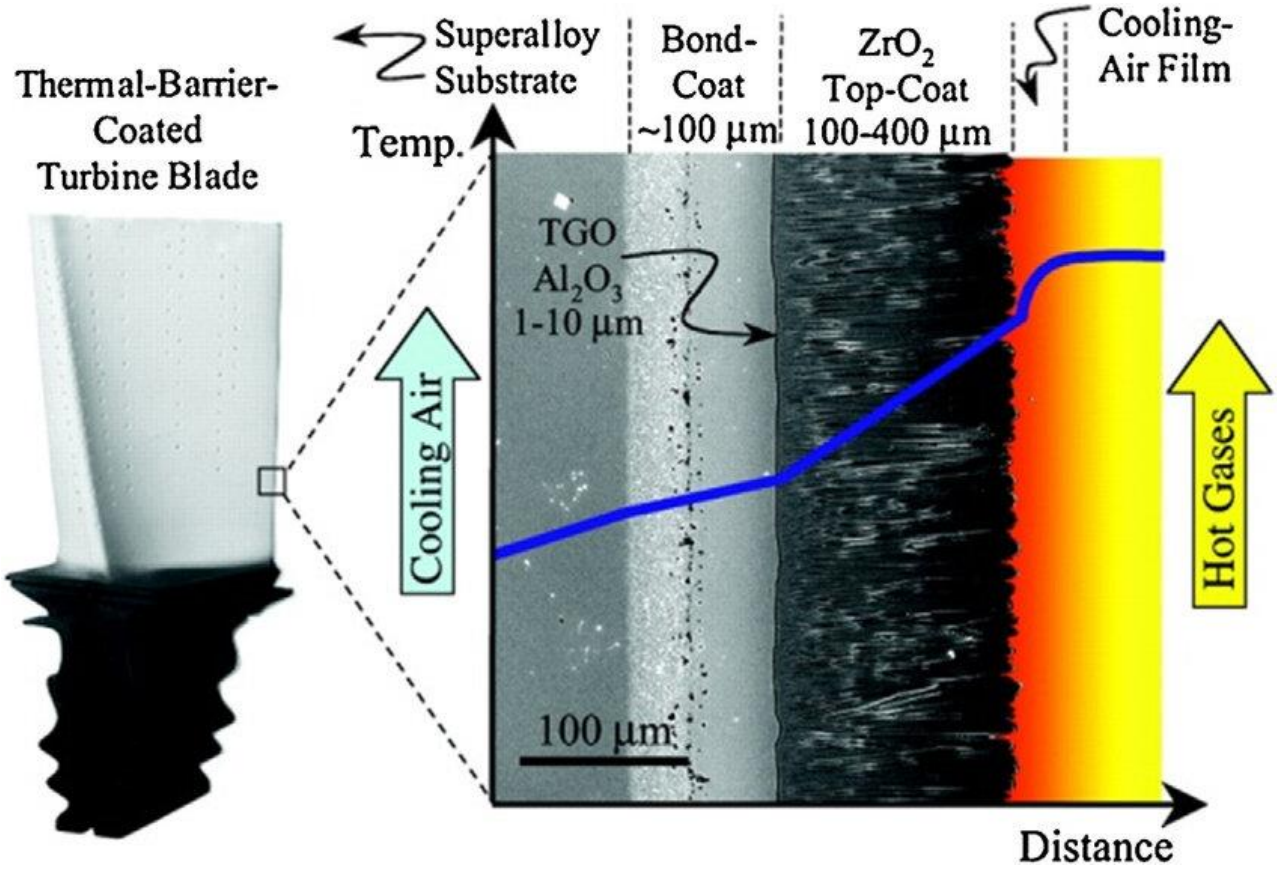

Figure 2.1: Schematic of a multilayer TBC system showing thermal insulation and protection under combustion conditions **[8]**.

2.2 Overview of ceramic Topcoat materials and their corresponding properties

Thermal barrier coatings (TBCs) are based on ceramic materials and play a significant role in safeguarding the metallic components in high temperature scenarios (i.e. gas turbine, jet engines, aerospace propulsion systems and high temperature nuclear reactors). These ceramics serve as a key component of insulating topcoats, which can significantly reduce the heat transfer rate to the underlying metallic material, allowing engines to operate at higher temperatures with increased efficiency and longer life. Yttria-stabilised zirconia (YSZ) is one of the most well-established ceramic materials. It has been widely utilised due to its relatively low thermal conductivity, high melting temperature (around 2700 °C), high phase stability at temperatures below 1200 °C, and compatibility with nickel-based superalloys in terms of thermal expansion. However, as the time duration increases to higher than 1200 °C, YSZ undergoes sintering and a disastrous phase transformation that changes the tetragonal phase to a monoclinic phase, causing volumetric change, cracking, and ultimate breakage of the coating **[9-11]**. As a result

of these constraints, other types of ceramics that show better thermal and structural performance have been explored.

Rare-earth zirconates, including gadolinium zirconate ($Gd_2Zr_2O_7$), lanthanum zirconate ($La_2Zr_2O_7$), Neodymium zirconates ($Nd_2Zr_2O_7$), and samarium zirconate ($Sm_2Zr_2O_7$) have become interesting options because they do not exhibit degradation behavior during long-term thermal cycling; due to their high phase stability, low oxygen ion conductivity, and low thermal conductivity (down to the lowest possible 1 W/ Their low thermal diffusivity and oxygen transport resistance, both promoted via their pyrochlore crystal structures, makes them have long-term performance at harsh environments. Additionally, other rare-earth oxides, such as ceria (CeO_2), lanthana (La_2O_3), praseodymia (Pr_6O_{11}), neodymia (Nd_2O_3), and europia (Eu_2O_3), are used as dopants or stabilisers to improve thermal expansion behaviour, strengthen fracture toughness, and inhibit sintering **[12-14]**.

In addition to the rare-earth oxides, many other ceramic systems have been found to have considerable potential. A case in point is alumina (Al_2O_3), which has a high melting point (>2050 °C), is chemically stable, exhibits high thermal shock durability, and can be used as an excellent protective coating in hostile environments. Hafnia (HfO_2), which is structurally related to zirconia, is more phase stable and has an even higher melting point (around 2800 °C), as well as a low thermal conductivity, making it suitable for use at ultra-high temperatures. Other thermophysical properties of lanthanum magnesium hexaaluminates ($LaMgAl_{11}O_{19}$), garnets such as the yttrium aluminium garnet ($Y_3Al_5O_{12}$), and perovskites (general formula (ABO_3) are also examined due to their stable thermophysical characteristics, low oxygen diffusivity, and negligible sintering at high temperatures. The other candidate, monazite ($LaPO_4$), also has a minimal set of properties, namely a high thermal expansion coefficient, low thermal conductivity, and chemical inertness, which render it a possible candidate for special use **[15-17]**.

These materials can be broadly classified based on their crystal structures, as shown in **Figure 2.2**, which categorises TBC ceramics into fluorite-type (e.g., YSZ, CeO_2), pyrochlore-type (e.g., $Gd_2Zr_2O_7$, $La_2Zr_2O_7$, $Nd_2Zr_2O_7$), perovskite-type (e.g., $LaAlO_3$), hexaaluminates-type (e.g., $LaMgAl_{11}O_{19}$), garnet-type (e.g., $Y_3Al_5O_{12}$), and monazite-type (e.g., $LaPO_4$) families. The thermal and mechanical characteristics of each type of structure are characteristically different, influencing performance factors such as compatibility with thermal expansion, phase stability, and resistance to sintering or corrosion. The choice of a suitable ceramic material in a TBC system is thus based on several important considerations: thermal conductivity, oxidative resistance, hot corrosion resistance, stability in the high-temperature phase during thermal

cycling, and mechanical integrity. Higher-grade ceramics should also resist molten salt attacks, such as vanadates, sulphates, and calcium-magnesium-alumina-silicate (CMAS), which tend to penetrate and chemically corrode the coating. In response, multi-component and composite ceramics are being increasingly developed to combine the strengths of different phases, offering enhanced durability and performance in the severe thermal and chemical environments faced by next-generation propulsion and power systems **[18-19]**.

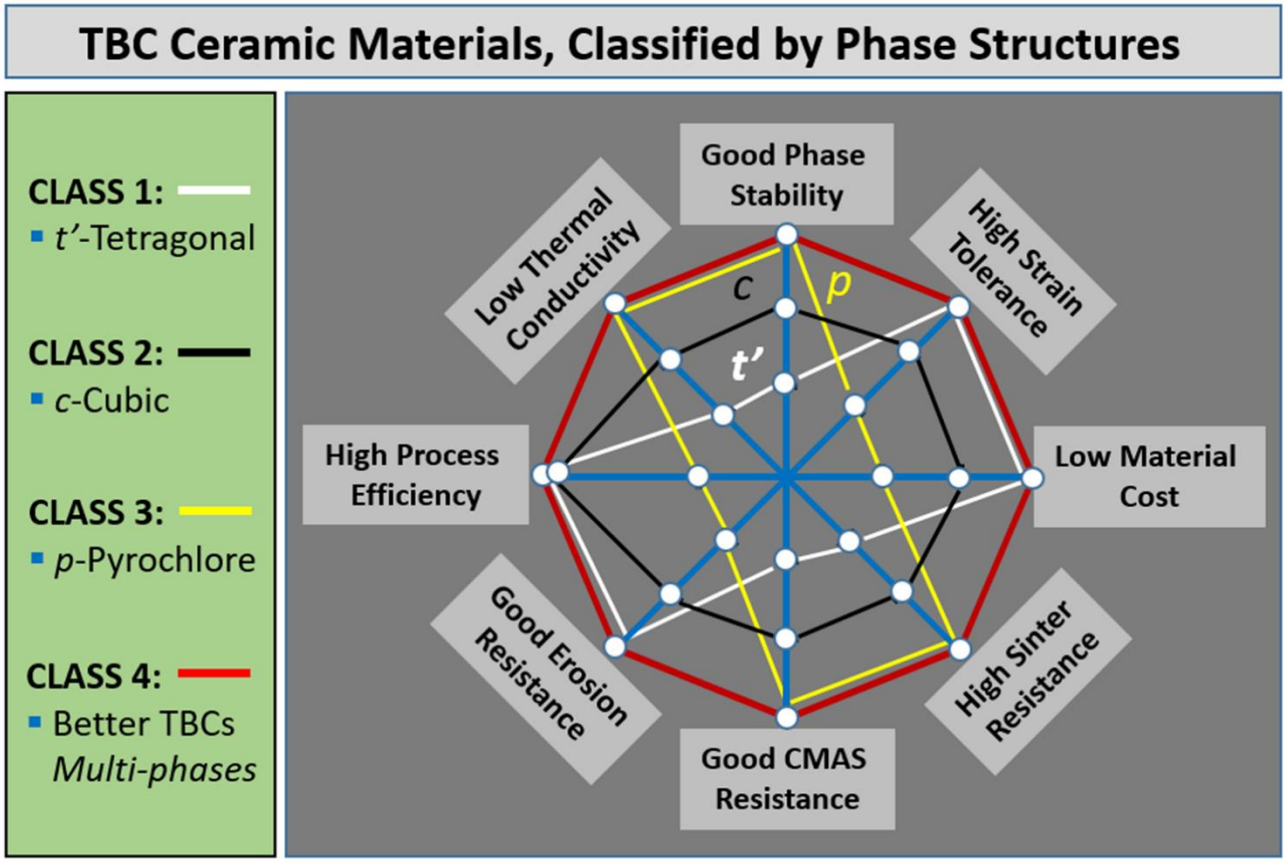

Figure 2.2: Structural classification and property evaluation of advanced TBC ceramics **[20]**.

2.3 Bond Coat materials

The bond coat (BC) in thermal barrier coating (TBC) systems serves as a critical metallic intermediate layer between the ceramic topcoat and the metallic substrate, primarily designed to enhance adhesion, accommodate thermal expansion mismatch, and offer oxidation and corrosion protection during high-temperature operation. Commonly, the bond coat is composed of MCrAlY alloys, where M represents nickel (Ni), cobalt (Co), iron (Fe), or combinations thereof. These alloys are particularly valued for their ability to form a stable and continuous

alumina (Al_2O_3) scale during thermal exposure, which acts as a thermally grown oxide (TGO) layer. The TGO is created due to the diffusion of oxygen through the topcoat of the ceramic and acts as a crucial diffusion barrier, which slows down the further oxidation of the bond coat and substrate. This TGO layer has a significant impact on the life and lifetime of the entire TBC system. Nevertheless, the bond coat can be degraded by prolonged exposure to high-temperature conditions, particularly those that contain corrosive species, such as vanadium, sulphur, calcium, and magnesium, and can react through complex reactions, such as acidic or basic fluxing. To improve the high-temperature corrosion and oxidation resistance, the properties of MCrAlY bond coats have been modified by alloying with noble metals like platinum (Pt) and hafnium (Hf), which enhance thermal cycling life and resistance to environmental attack. In addition, other materials, such as Cr_2AlC and CoCrAlY-TiB_2 have demonstrated good performances in the resistance to oxidation and the inhibition of diffusion of elements. Practical methods, such as electroplating using ionic liquids, have also been explored for depositing alumina-enriched diffusion coatings to achieve better oxidation resistance in aluminides. Overall, the selection and engineering of bond coat materials are crucial in managing thermomechanical stresses, maintaining coating adhesion, and ensuring the long-term performance of TBCs in harsh gas turbine and propulsion environments **[1],[19-22]**.

2.4 Deposition Techniques of TBCs

There are several methods for producing thermal barrier coatings (TBCs), each with its own advantages. Atmospheric Plasma Spray (APS) is economical for large-scale production, typically yielding a lamellar microstructure. Suspension Plasma Spray (SPS) utilises a columnar microstructure in the formation of the coating, which is strain-tolerant and resistant to thermal shock. Electron Beam Physical Vapour Deposition (EB-PVD) coating has a more columnar structure, which is better suited for thermal cycling, but is more expensive. Plasma Spray-Physical Vapour Deposition (PS-PVD) is a combination of plasma spraying and vapour deposition, resulting in the development of both laminar and columnar growth, and providing a mixture of controlled deposition and high performance. **Fig. 2.3** presents a schematic diagram of TBC preparation, including the working principle of the equipment, a cross-sectional view of the coatings, and surface SEM images **[23]**.

2.4.1 Atmospheric Plasma Spraying (APS)

Atmospheric Plasma Spraying (APS) is one of the most popular methods for depositing thermal barrier coatings (TBCs) because it is both versatile and cost-effective, and able to coat components of any size. APS is a method that involves introducing ceramic feedstock particles into a high-temperature plasma jet, which then partially melts and propels them onto the substrate. The outcomes of this process include the formation of coatings with a lamellar microstructure, where the splats exhibit perpendicular porosity to the heat flow. The main benefit of this structure is that it reduces thermal conductivity, and the values can be as low as 1.0 W/mK when stabilised with yttria, which is suitable for thermal insulation. Although APS offers very high flexibility regarding deposition area and equipment cost, the resulting coating typically exhibits less thermal shock resistance than a columnar microstructure created by other processes, such as EB-PVD. Although the lamellar structure has the advantage of decreasing thermal conductivity, it may lead to a weakening of the mechanical properties, including reduced fracture toughness; hence, APS-deposited TBCs are more likely to fail in extreme thermal cycling conditions. Additionally, the porous nature of APS coatings may lead to increased susceptibility to degradation and high-temperature oxidation in the environment. Depositions formed by this method are usually porous in nature, and the particles are not in a homogeneous distribution, a characteristic of partially molten splats, which are formed during the spray stage. This structure may be due to the oxidation and cooling of the sprayed particles before they fully fuse. The agglomerated particles can be seen in the coatings, which are rough and irregular, which is expected in the case of rapid cooling and incomplete melting during the spraying process. This results in rough surfaces with high levels of porosity, which may influence the mechanical properties and performance of the coating in critical conditions. Nevertheless, the APS technique remains one of the preferred methods for producing TBCs on a large scale, particularly for components that are less prone to mechanical and thermal stresses. The reason why APS is the best is because of its comparatively low cost and its capacity to deposit thick coatings, which is very suitable in power generation, and large turbines used in industries. However, the continuous investigation of the optimisation of the APS parameters, including the spray distance, the rate of gas flow, and the properties of the feedstock, is the key to the further enhancement of the durability and operation of the TBCs deposited through this technique **[24-26]**.

2.4.2 Electron Beam Physical Vapour Deposition (EB-PVD)

Electron Beam Physical Vapour Deposition (EB-PVD) is a widely used technique for depositing thermal barrier coatings (TBCs), particularly in high-performance applications such as gas turbines and aerospace components. This is achieved by vaporising the target material with a high-energy electron beam and condensing the resulting vapour onto a substrate under vacuum. It is particularly noted for its capability to produce TBCs with a columnar microstructure, which is highly strain-tolerant. This microstructure is crucial in enhancing the coating's resistance to thermal cycling and mechanical stress in high-temperature conditions, thereby increasing the lifespan of the coated parts. The benefits of EB-PVD TBCs include better thermal cycling resistance and lower thermal conductivity, which enhance the energy efficiency of turbines and engines by maintaining the thermal gradient between the hot gases and the substrate. The vertical alignment of the ceramic grains enables this columnar construction to be more resistant to spallation and delamination than other coating methods, such as those made by atmospheric plasma spraying (APS) **[27]**.

The coating exhibits a more compact and layered structure with vertical growth, a characteristic typical of high-energy deposition in EB-PVD. The effect of this approach is smoother and more unified coatings. In this case, the layers are more transparent and have a finer texture, allowing for the observation of columnar grain growth in the microstructure. Such behaviour is typical of directional solidification, as the rate of deposition in the EB-PVD method is relatively low. Nevertheless, the price of EB-PVD equipment and the deposition rate are higher, which makes it less economical in specific applications, although it offers better performance. The recent developments have been aimed at streamlining the EB-PVD process to make it efficient and minimise the costs of its operation. This capability to accurately regulate the thickness and microstructure of the coating can be used to create coatings of customised properties, including enhanced resistance to molten salts and resistance to environmental degradation. As demand for high-temperature, corrosion-resistant materials grows, EB-PVD remains a leading technique for fabricating TBCs that meet the stringent requirements of modern engineering applications**[12],[28-30]**.

2.4.3 Suspension Plasma Spraying (SPS)

Suspension Plasma Spray (SPS) is a superior deposition method that is extensively applied in the production of thermal barrier coatings (TBCs) with exceptional thermal performance. In SPS, a liquid suspension containing ceramic particles is sprayed into a high-temperature plasma flame, where the particles are heated, melted, and deposited on a substrate very quickly. The

major strength of SPS over other traditional techniques, such as Atmospheric Plasma Spray (APS), is its capability to form coatings with a columnar microstructure, similar to the microstructure present in Electron Beam Physical Vapour Deposition (EB-PVD), but at a faster deposition rate and with reduced operational costs. The columnar microstructure enhances the strain-tolerant and thermal shock-resistant capacity of the TBCs, making them suitable for high-temperature applications such as gas turbines and aero-engine parts. The sintering process, which occurs when molten particles settle on the substrate and interconnect with one another, also contributes to the uniformity of the coating and its density. The result is that a stronger structure possesses better mechanical properties. The SPS process enables the focused control of coating properties, including thickness, porosity, and microstructure, by adjusting various process parameters, such as spray distance, plasma power, and suspension viscosity. This control is necessary to maximise the thermal conductivity of the TBCs, which can be reduced through precise control of the coating porosity. Unlike APS, which tends to develop lamellar structures and interlamellar cracks that can lead to spallation in the case of thermal cycling, SPS coating has a more robust and continuous microstructure that is unlikely to fail through the exact same mechanisms.

The coating made using this method exhibits good bonding between the upper and bond coat layers as well as less porosity than APS. The pressure sintering process tends to produce denser and uniform structures. The tight packing of the particles and the smooth surfaces indicate efficient sintering, leading to high-density microstructures with few voids and pores. Such a combination of high deposition rates, controllable microstructure, and enhanced performance in extreme thermal and environmental loads makes SPS a very appealing method for developing robust TBCs that can support the growing demands of high-temperature engineering methods **[27],[29],[31]**.

2.4.4 Plasma Spray Physical Vapour Deposition (PS-PVD)

PS-PVD combines the aspects of both plasma spraying and physical vapour deposition, and it is a highly effective method of obtaining thermal barrier coatings (TBCs) with unique microstructures. PS-PVD vaporises feedstock material by low-pressure plasma and deposits it on a substrate as a dense and uniform coating. The technology is especially well-known for producing a columnar microstructure, which offers high strain resistance and mechanical strength compared to other standard procedures, such as Atmospheric Plasma Spray (APS). The products are TBCs that are very suitable in high temperature applications like gas turbines and aero-engines, where thermal cycling and mechanical strain are paramount.

Among the significant benefits of PS-PVD, the ability to control the deposition parameters (e.g., plasma power and feedstock material) and, consequently, the microstructure and properties of the coating should be noted. The columnar microstructure obtained using PS-PVD enhances the coating's fracture toughness and thermal shock resistance, thereby improving its durability compared to coatings developed using APS, which are prone to interlamellar cracks and increased porosity. The PS-PVD also offers non-line-of-sight deposition, making it suitable for complex geometries, and the coatings are more resistant to erosion as well as thermal cyclic fatigue. This is a combination of better life and performance in extreme conditions that makes PS-PVD a popular method of producing TBCs capable of surviving the demanding applications in advanced high-temperature engineering systems. The resultant coating produced by this method resembles APS in terms of porosity and roughness, but features a more controlled and uniform deposition process, with splats being finer and improved bonding between layers. The coating structure is a combination of both laminar and columnar growth. There are some columnar features observed in the finer texture. Still, the overall structure exhibits characteristics of both laminar layering and columnar growth, indicating a balance between controlled deposition and rapid solidification **[29],[32-33]**.

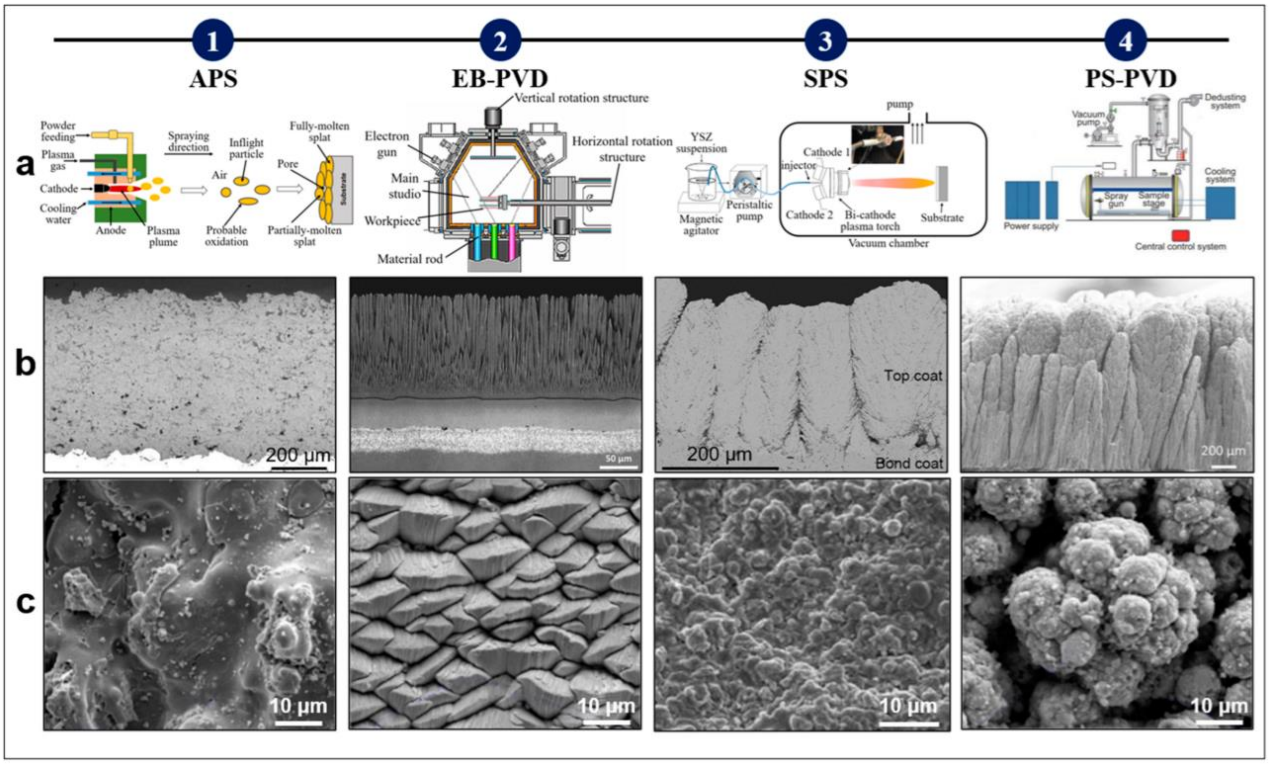

Figure 2.3: Schematic diagram of the preparation process of TBCs: (a) equipment working principle (b) cross-section (c) surface SEM images **[23]**.

2.5 TBCs Failure Mechanisms

Thermal barrier coating (TBC) structural integrity and durability have critical roles in the performance and life of gas turbine components operating in conditions characterised by high temperature. The mechanisms of TBC failure, which depend on the coating architecture and operating conditions, can have a significant impact on turbine life. TBC degradation generally causes a slow decrease in performance when used as a life extension technique, but can cause catastrophic damage by failing to provide a graceful shutdown of the underlying substrate to excessive thermal loads when they are part of the component design boundary. In TBCs, failure is defined as the point at which the coating system ceases to perform its protective thermal insulation or structural roles, most typically indicated by topcoat spallation. Such spallation can be initiated by thermal fatigue, corrosion, erosion, or a combination of these factors, including the attack by calcium-magnesium-alumina-silicate (CMAS), the growth of oxide scales at the thermally grown oxide (TGO) interface, or the development of hot corrosion by fuel impurities. This is further complicated by the fact that various degradation modes, such as thermal cycling, sintering, phase instability, and thermomechanical mismatch, may occur concomitantly, thus causing accelerated failure behaviour and making life prediction more difficult. Therefore, the mechanisms of multifaceted degradation of TBCs are still key to their successful design, qualification, and use in advanced gas turbines **[25],[34-35]**.

2.5.1 Thermal Fatigue

Thermal fatigue is a phenomenon that results in damage due to periodic thermal stresses that are caused by variations in temperature. This is typically due to frequent start-stop cycles in land-based gas turbines. The vulnerability to thermal fatigue increases as turbine technologies operate at higher temperatures and cycle faster. These conditions enhance degradation processes that decrease the life and performance of the coating. There is generally a combination of interacting mechanisms that contribute to the degradation of thermal barrier coatings (TBCs) under thermal fatigue conditions, which are described as follows.

2.5.1.1 Mismatch in the coefficient of thermal expansion

A notable factor contributing to the premature failure of thermal barrier coatings (TBCs) is the mismatch in the coefficient of thermal expansion (CTE) between the ceramic topcoat, thermally grown oxide (TGO), and metallic bond coat or substrate. The CTE of the topcoat, such as 7–8 mol% yttria-stabilised zirconia or advanced rare-earth zirconates, is typically ~10.5×10^{-6} 1/K, for α-Al_2O_3 TGO it is ~8×10^{-6} 1/K, while Ni-based superalloy substrates reach ~16.6×10^{-6}

1/K. This disparity generates cyclic tensile and compressive stresses during heating and cooling, which promote the initiation and propagation of cracks at or near the TGO/topcoat interface. Under service conditions, these stresses are further intensified by topcoat sintering, bond coat oxidation, and infiltration of molten salts or CMAS deposits, which reduce strain tolerance and accelerate spallation **[36-37]**.

To isolate the effect of CTE mismatch, thermal shock tests (burner rig tests) are often conducted, where heating and cooling rates are much higher than in furnace cycling, and dwell times at peak temperature are minimal. In such cases, TGO growth is negligible, and failure is primarily driven by the rapid accumulation of thermal stress between layers. In contrast, furnace cycling tests with dwell times of 10–60 minutes result in degradation due to a combination of CTE mismatch, sintering, oxidation, and interdiffusion. Literature also highlights that tailoring the CTE through rare-earth doping, dual-phase composite topcoats, or functionally graded layers, as well as employing microstructural designs such as columnar EB-PVD coatings, can significantly enhance thermal fatigue resistance. The influence of this mismatch is often visualised through temperature–expansion curves for the topcoat, TGO, and substrate, clearly marking interfacial stress peaks where cracking is most likely to occur **[38-39]**.

2.5.1.2 Sintering of topcoat

Sintering refers to a process in which the densification of the material occurs through the closure of pores and the healing of microcracks. The deposition mechanism results in APS TBCs having a mixture of micro-cracks, small pores, and irregularly shaped openings, which reduce both the thermal conductivity and the elastic modulus. At higher temperatures, especially above 1200 °C, sintering of these structural defects occurs, leading to increased thermal conductivity and elastic modulus. Different levels of thermal conductivity are undesirable because they compromise the thermal grading along the coating, thereby reducing the thermal insulation properties and overall performance of the TBC. Both the density of micro-cracks in the coating and its porosity determine the elastic modulus (stiffness). Coatings with lower elastic moduli exhibit the best thermal cycling lifetimes compared to stiffer coatings, as they can better absorb thermal mismatch stresses. The values of the elastic modulus of APS coatings reported lie within a wide range, averaging between 10 and 60 GPa, due to variations in spraying parameters, the size of the feedstock powder, and the measuring methods used. An example would be a bending test with results (lower) of the global stiffness, but an indentation test with (higher) local stiffness.

The increase in elastic modulus due to sintering is rapid during the initial exposure period, followed by a slower rate with extended time, eventually reaching a plateau. This time, temperature dependence can be described by a linear function of the Larson–Miller parameter (LMP) as

$$E = m.LMP + c \quad (1)$$

$$LMP = T.(logt + C_k) \quad (2)$$

where T is the absolute temperature (K), t is the exposure time (h), C_k is a constant (often ~20), E is the elastic modulus, and m and c are the slope and intercept, respectively.

An alternative description of elastic modulus evolution with time is given by:

$$\frac{E_c - E_c^0}{E_c^{inf} - E_c^0} = C_E(1 - e^{-\frac{t}{\tau}}) \quad (3)$$

Where E_c is the modulus at any time t, E_c^0 is the initial modulus, E_c^{inf} is the modulus at infinite time, τ is the relaxation time, and C_E is a constant related to temperature and coating stress state. These models demonstrate the significant impact of sintering on the mechanical properties of TBCs. Strategies to mitigate sintering, such as the use of rare-earth zirconates, dual-phase composites, and vertical segmentation microstructures, can slow densification rates, retain strain tolerance, and extend TBC lifetime under aggressive turbine operating conditions **[40-42]**.

2.5.1.3 Bond coat oxidation and inter-diffusion

Oxidation of the bond coat during high-temperature exposure is a significant contributor to TBC failure. During the high-temperature dwell period in a thermal cycling fatigue (TCF) cycle, the bond coat oxidises, and a thermally grown oxide (TGO) layer develops at the bond coat/topcoat interface. Initially, the TGO is a continuous α-Al_2O_3 layer, which is desirable due to its slow growth rate and good adherence. With prolonged exposure, the oxide layer thickens, and its morphology becomes irregular due to localised aluminium depletion, incorporation of impurities, and microstructural defects. The stresses within the TGO arise from (1) growth stress caused by the transformation of dense metal into a less dense oxide, and (2) CTE mismatch between the TGO and adjacent coating layers. The total residual stress in the TGO is the sum of these contributions**[43]**. For alumina at room temperature, growth stresses are about 1 GPa, representing roughly 10% of the total residual stress. When the oxide layer reaches a

critical thickness, typically 6–10 μm, it can spall off together with the topcoat, signalling the end of the coating's service life.

Premature failure can also occur at a lower TGO thickness, known as **chemical failure**. This arises when the aluminium content in the bond coat drops below the threshold needed to sustain α-Al_2O_3 formation. In such cases, other oxides form, often from alloying elements in the bond coat, resulting in the formation of chromia and spinel phases. These transformations can proceed either directly from the bond coat alloy or by decomposition of alumina, as expressed by:

$$Al_2O_3 + 2Cr \rightarrow Cr_2O_3 + 2Al \quad (4)$$

$$Al_2O_3 + \frac{1}{2}O_2 + Ni \rightarrow NiAl_2O_4 \quad (5)$$

The protective alumina scale is then replaced by faster-growing oxides such as Cr_2O_3, NiO, CoO, and mixed spinels $(Ni,Co)(Cr,Al)_2O_4$. Without a continuous α-Al_2O_3 barrier, oxygen can diffuse deeper into the bond coat, causing internal oxidation. In APS coatings, internal oxidation can produce "island-like" oxide distributions that reduce interfacial stress and, in some cases, lower the effective CTE of the bond coat, thereby reducing mismatch stresses with the ceramic topcoat **[44-45]**.

Interdiffusion between the bond coat and the substrate also contributes to the depletion of aluminium. Aluminium activity in the bond coat is greater than that of the superalloy substrate, resulting in the diffusion of Al inwards. Hence, the bond coat is not able to create a protective oxide scale. This can be affected by the bond coat composition, the deposition process (e.g. LPPS, HVOF, EB-PVD), as well as the substrate chemistry. Not only do high interdiffusion rates accelerate the oxide transitions, but they also favour the formation of an interdiffusion zone (IDZ) rich in brittle topologically close-packed (TCP) phases that reduce substrate strength. Refractory elements such as W, Ta, and Mo can also diffuse out of the substrate into the bond coat, affecting the kinetics of TGO growth while increasing oxidation resistance. The selection of coating–substrate systems with minimal aluminium activity differences, combined with the use of reactive element doping (Hf, Y, Zr), can suppress both oxidation and interdiffusion, thereby extending the coating lifetime under severe cyclic conditions **[46-47]**.

2.5.2 Hot Corrosion

Hot corrosion is a high-temperature degradation mechanism that takes place when molten salts come into contact with materials under the influence of an oxidising atmosphere, causing a faster rate of deterioration than pure oxidation. This is particularly acute in thermal barrier coatings (TBCs) used in gas turbines, aeroengines, marine propulsion systems, and other high-temperature applications. The causes of the salts are typically fuel impurities, air particulates, marine aerosols, and combustion products. They are capable of penetrating the microstructure of the TBC and chemically destabilising the ceramic topcoat, as well as the metallic bond coat, leading to cracking, spallation, and early failure **[2],[25],[48]**.

There are two main types of hot corrosion identified based on temperature regime: Low-Temperature Hot Corrosion (LTHC or Type II). This is a type of corrosion that occurs between temperatures of approximately 650-850 °C, when sodium sulfate (Na_2SO_4) is solid at the initial stages. In the long run, reactions of the protective scale by the solid state of the oxide result in low-melting eutectic mixtures. These mixtures gain corrosive power when they are melting, which eventually speeds up the corrosion process. LTHC usually correlates with SO3-induced corrosion and exhibits a maximum in corrosion rate at intermediate temperatures. High Temperature Hot Corrosion (HTHC or Type I): This occurs at temperatures higher than those of Na2SO4 (≈ approximately 884 °C). Here, the initial reaction involves molten Na_2SO_4, and an active corrosive reaction occurs instantly. The attack is fast and harsh, which is catalysed by acidic and basic fluxing **[4][49]**.

The distinct behaviours of LTHC and HTHC are illustrated in **Fig. 2.4**, which shows the variation in corrosion rate with temperature for both types, as well as for pure oxidation. In LTHC, the rate peaks around 700–750 °C, whereas in HTHC, the attack accelerates rapidly above ~900 °C **[50-52]**.

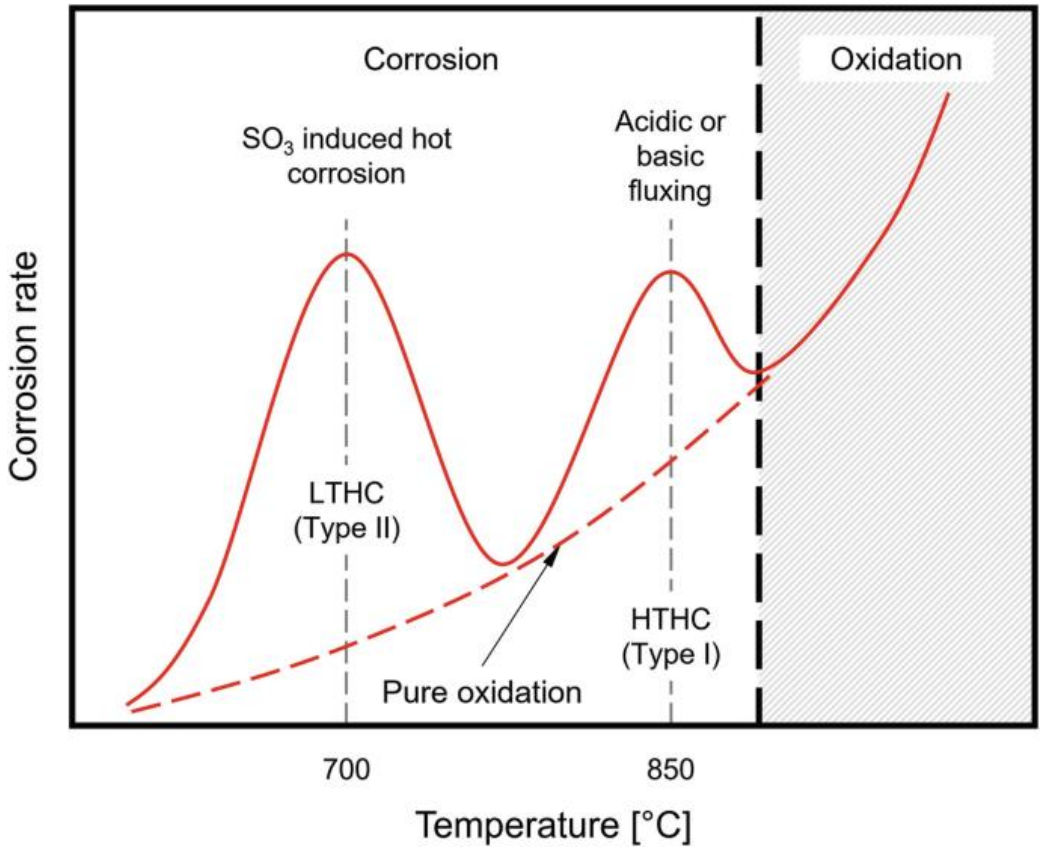

Figure 2.4: Schematic comparison of high-temperature hot corrosion (Type I) and low-temperature hot corrosion (Type II) behaviour compared to oxidation rate as a function of temperature **[51][53].**

The corrosive atmosphere usually includes sodium sulfate (Na_2SO_4), potassium sulfate (K_2SO_4), calcium sulfate ($CaSO_4$) and vanadium pentoxide (V_2O_5). The salts may co-exist to form binary and ternary eutectic mixtures, which melt at lower temperatures than the respective salts. These mixtures become highly mobile in their molten form and may penetrate the microstructure of the coating, reacting aggressively with protective phases. The melting points of relevant corrosive sulfate and eutectic mixtures are summarised in **Table 1**. Compounds such as $Na_2S_2O_7$ (400.9 °C) and $K_2S_2O_7$ (325 °C) are especially hazardous, as they can melt well below the operational temperatures of turbines, enabling corrosion in regions once thought safe from molten salt attack **[54]**.

Table 2.1: Liquification Temperatures of Potentially Corrosive Sulphates **[3],[54]**.

Number	Molten Salt	Melting Temperature (T_m)
1.	Na_2SO_4	884 °C
2.	K_2SO_4	1069 °C
3.	$Na_2S_2O_7$	400.9 °C
4.	$K_2S_2O_7$	325 °C
5.	$Na_3Fe(SO_4)_3$	624 °C
6.	$K_2Fe(SO_4)_3$	618 °C
7.	Na_2SO_4–$CoSO_4$	575 °C
8.	K_2SO_4–$CoSO_4$	535 °C
9.	$CaSO_4$	1460 °C
10.	$MgSO_4$	1124 °C
11.	$CoSO_4$	735 °C
12.	Na_2SO_4–$MgSO_4$	660 °C

When molten, these salts react with oxides in the TBC. For instance, vanadium pentoxide reacts with Na_2SO_4, K_2SO_4, $CaSO_4$ and $MgSO_4$ to form low-melting vanadates via:

$$xNa_2SO_4 + yV_2O_5 \rightarrow xNa_2O \cdot yV_2O_5 + xSO_3 \quad (6)$$

$$xK_2SO_4 + yV_2O_5 \rightarrow xK_2O \cdot yV_2O_5 + xSO_3 \quad (7)$$

$$xCaSO_4 + yV_2O_5 \rightarrow xCaO \cdot yV_2O_5 + xSO_3 \quad (8)$$

$$xMgSO_4 + yV_2O_5 \rightarrow xMgO \cdot yV_2O_5 + xSO_3 \quad (9)$$

These vanadates dissolve protective alumina layers and destabilize tetragonal zirconia (t-ZrO_2) into monoclinic zirconia (m-ZrO_2). This transformation involves an approximate 5% volume expansion, which induces stresses and promotes cracking. An example of such destabilization is:

$$t - ZrO_2(Y_2O_3)(s) + 2NaVO_3(S) \rightarrow m - ZrO_2(s) + 2YVO_4(S) + Na_2O \quad (10)$$

In **HTHC**, Na_2SO_4 is molten from the outset and dissociates into acidic and basic components according to:

$$Na_2SO_4 \rightarrow Na_2O\ (\text{Basic}) + SO_3\ (\text{Acidic}) \quad (11)$$

The formation of Na_2SO_4 from elemental sodium and sulphur follows:

$$2\,Na + ½\,O_2 \rightarrow Na_2O\ \text{Acidic} \quad (12)$$

$$S + O2 \rightarrow SO_2;\ SO_2 + ½\,O_2 \rightarrow SO_3\ \text{Basic} \quad (13)$$

$$SO_3 + Na_2O \rightarrow Na_2SO_4\ \text{Slat Formation} \quad (14)$$

In **LTHC**, Na_2SO_4 remains solid initially, but through reactions with oxides it generates low-melting eutectics that eventually liquefy and initiate rapid attack. Potassium and calcium participate in analogous reactions:

$$2\,K + ½\,O_2 \rightarrow K_2O\ \text{Acidic} \quad (15)$$

$$S + O_2 \rightarrow SO_2;\ SO_2 + ½\,O_2 \rightarrow SO_3\ \text{Basic} \quad (16)$$

$$SO_3 + K_2O \rightarrow K_2SO_4\ \text{Slat Formation} \quad (17)$$

$$Ca + ½\,O_2 \rightarrow CaO\ \text{Acidic} \quad (18)$$

$$S + O_2 \rightarrow SO_2;\ SO_2 + ½\,O_2 \rightarrow SO_3\ \text{Basic} \quad (19)$$

$$SO_3 + CaO \rightarrow CaSO_4\ \text{Salt Formation} \quad (20)$$

Rare-earth zirconates in advanced TBCs also react with SO_3, producing corresponding sulphates and destabilising zirconia:

$$ZrO_2\ (Y_2O_3) + 3SO_3\ (\text{gas}) \rightarrow Y_2(SO_4)3 + m - ZrO_2 \quad (21)$$

$$ZrO_2\ (La_2O_3) + 3SO_3\ (\text{gas}) \rightarrow La_2(SO_4)3 + m - ZrO_2 \quad (22)$$

$$ZrO_2\ (Gd_2O_3) + 3SO_3\ (\text{gas}) \rightarrow Gd_2(SO_4)3 + m - O_2 \quad (23)$$

$$ZrO_2\ (Sm_2O_3) + 3SO_3\ (\text{gas}) \rightarrow Sm_2(SO_4)3 + m - ZrO_2 \quad (24)$$

$$ZrO_2\ (Nd_2O_3) + 3SO_3\ (\text{gas}) \rightarrow Nd_2(SO_4)3 + m - ZrO_2 \quad (25)$$

Hot corrosion is one of the most harmful degradation processes in high-temperature materials, which is a combination of molten salt chemistry, oxide dissolution, and phase destabilisation **[54-55]**. To prevent it, special attention should be paid to regulating fuel and environmental

contaminants, as well as developing corrosion-resistant coatings that can withstand both LTHC and HTHC conditions **[56]**.

Besides hot corrosion, CMAS (calcia–magnesia–alumino silicate) attack can also be extremely aggressive to thermal barrier coatings, and it starts as a result of absorbed airborne siliceous substances like sand, volcanic ash or dust. When deposited on turbine components, these particulates melt at engine operating temperatures (~1200–1300 °C) to form a glassy phase that infiltrates the porous topcoat microstructure. Upon penetration, molten CMAS reacts with yttria-stabilised zirconia, dissolving stabilising yttria and leading to destabilisation of the tetragonal zirconia phase into monoclinic zirconia, accompanied by volume expansion and cracking. Unlike hot corrosion caused by sulphates and vanadates, CMAS degradation is primarily infiltration-driven, resulting in the rapid loss of strain tolerance and spallation of the protective ceramic layer, thereby severely limiting the lifetime of TBCs **[57-58]**.

2.6 Hot Corrosion Behaviour of Rare-Earth Zirconates in Dual-Phase 8YSZ Coatings

The application of rare earth zirconates as co-phases with yttria-stabilised zirconia (8YSZ) has emerged as one of the most promising approaches to overcoming the chemical and thermal limitations of conventional TBCs. Not only are their thermal conductivities naturally low, but they are also higher melting and structurally stable. Their behaviour in hostile, hot, corrosive conditions, however, varies significantly with the character of the rare-earth cation. Under realistic conditions, the coating is often subjected to sodium sulfate depositions, the sources of which are fuel impurities, which promote chemical destabilisation and phase transformations. Understanding the resistance of different rare-earth zirconates in dual-phase systems is therefore crucial for identifying the most reliable candidate for long-term applications. The further details of the hot corrosion performance of $La_2Zr_2O_7$+8YSZ, $Gd_2Zr_2O_7$+8YSZ, and $Sm_2Zr_2O_7$+8YSZ are provided below, with a primary emphasis on the test environments, observed degradation mechanisms, and the development of the microstructure **[55],[59]**.

2.6.1 Hot Corrosion Behaviour of $La_2Zr_2O_7$+8YSZ and $Gd_2Zr_2O_7$+8YSZ Coatings

The literature on the behaviour of rare-earth zirconate-based dual-phase thermal barrier coatings under attack by sodium sulfate has been widely discussed. Two such systems, $La_2Zr_2O_7$+8YSZ and $Gd_2Zr_2O_7$ +8 YSZ, have undergone extensive comparative research, as both exhibit low thermal conductivity and high temperature, but vary significantly in their susceptibility to corrosive degradation.

$La_2Zr_2O_7$+8YSZ has generally been recognised as the most corrosion-resistant among the rare-earth zirconate composites. Reports describe that, during exposure to Na_2SO_4 deposits at 950

°C, the system retains the pyrochlore $La_2Zr_2O_7$ and tetragonal zirconia phases, with no significant formation of monoclinic zirconia. The representative XRD patterns reproduced in **Fig. 2.5** illustrate this retention of crystallographic stability, showing only minor secondary compounds, such as La–Cr–O, after extended exposure. Such stability is considered unusual compared to conventional YSZ, which typically undergoes tetragonal-to-monoclinic transformation in similar conditions **[60-61]**.

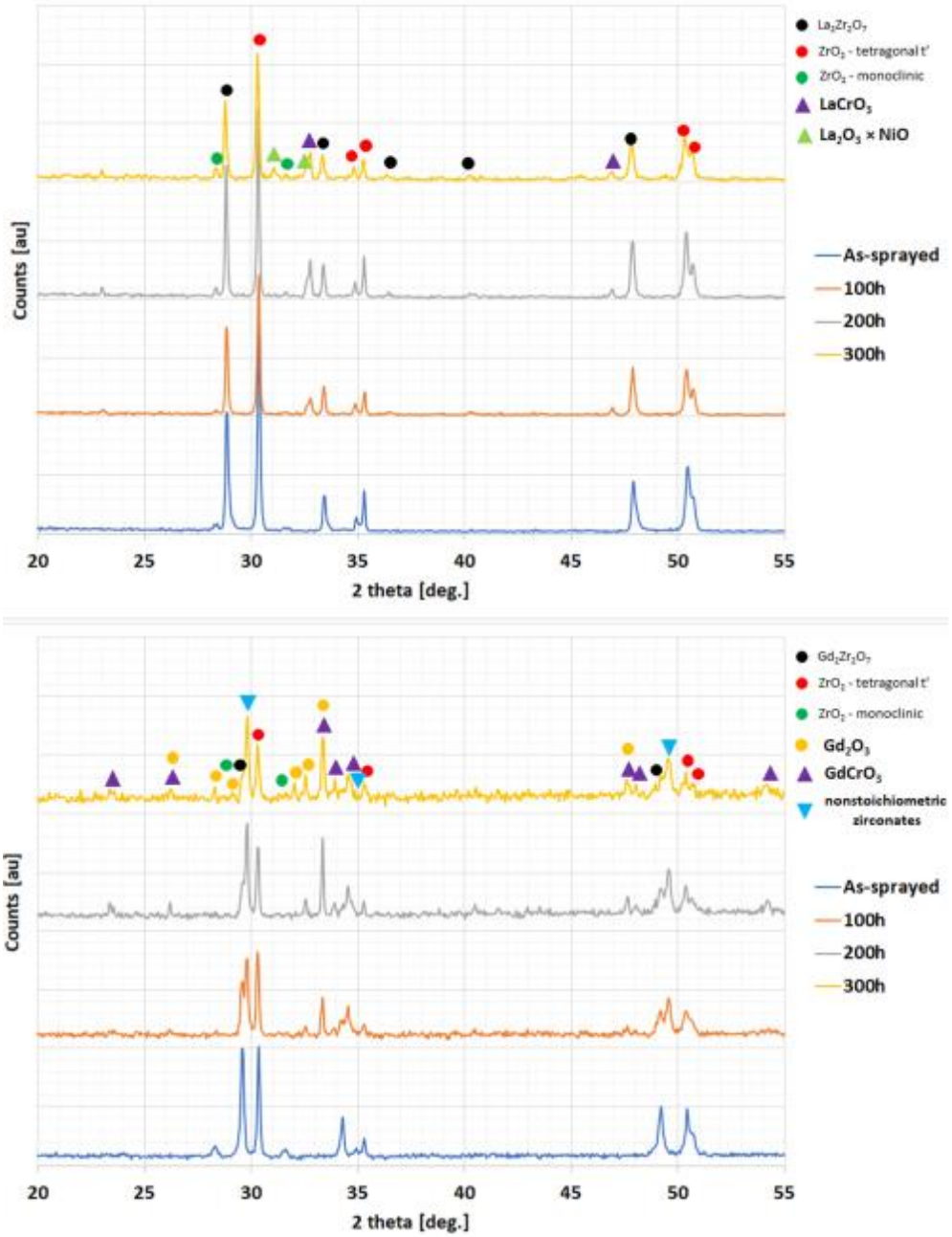

Figure 2.5: Results of phase constituent analysis of composite TBC systems under the condition of hot corrosion tests **[55]**.

Microstructural examinations of corroded $La_2Zr_2O_7$ +8YSZ have also been consistently reported to show good preservation of the lamellar splat morphology. Only localised pore growth and limited surface roughness have been described, while features such as deep cracking or bulk salt penetration are absent. As shown in **Fig. 2.6**, the microstructure after hot corrosion remains relatively intact, a feature attributed to the chemical compatibility of the La-containing pyrochlore with sodium salts.

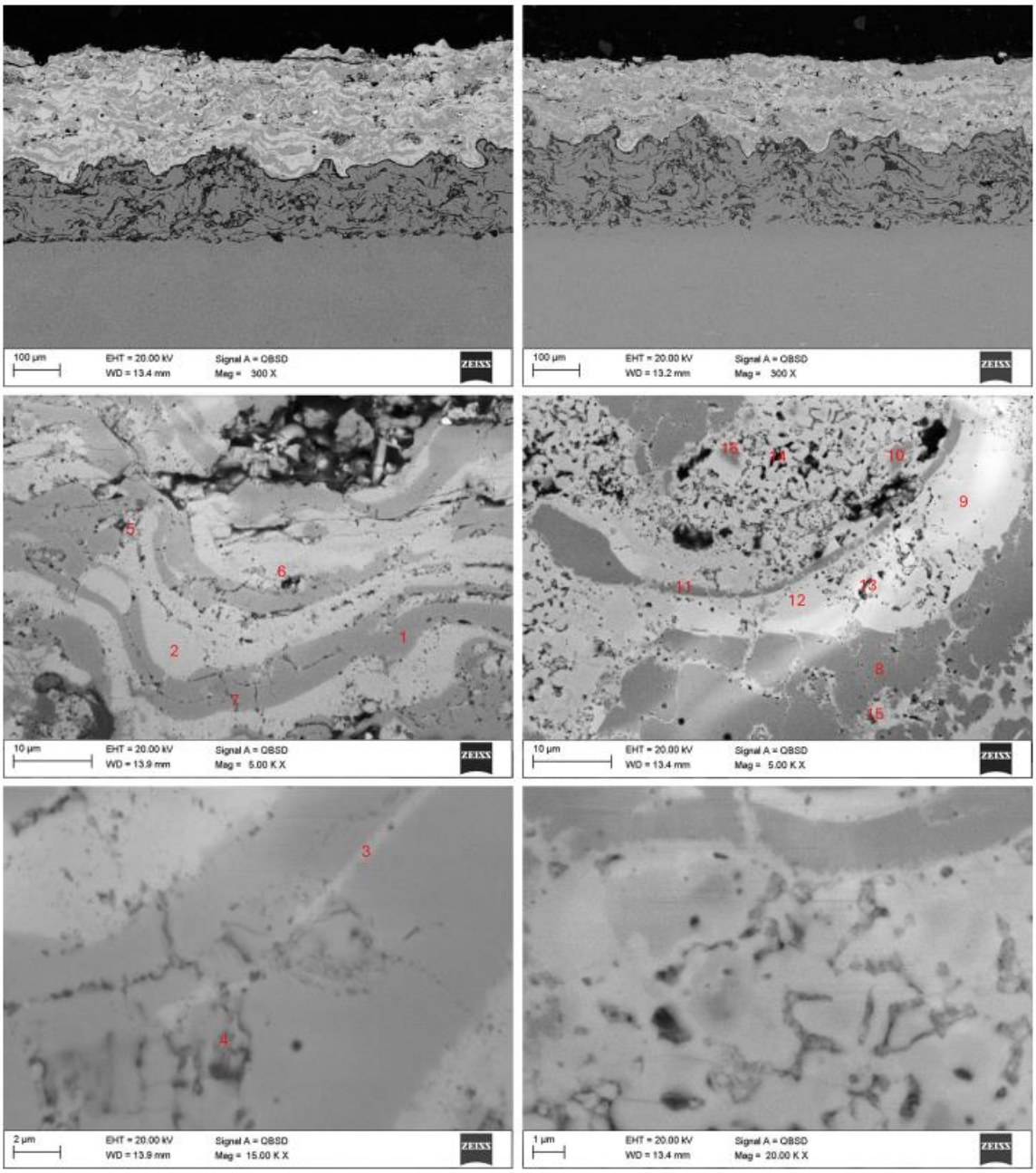

Figure 2.6: Microstructural details of composite TBC systems after hot corrosion test at pure liquid sodium sulphate salt **[55]**.

In contrast, the hot corrosion resistance of $Gd_2Zr_2O_7$+8YSZ has been reported to be less favourable. Literature accounts describe that sodium sulfate exposure at 950 °C promotes partial destabilisation of the $Gd_2Zr_2O_7$ phase, leading to the formation of fluorite-like non-stoichiometric compounds. The XRD data in **Fig. 2.5** provide an example of this behaviour, where additional phases emerge after exposure that are not observed in $La_2Zr_2O_7$+8YSZ. Microstructural changes of $Gd_2Zr_2O_7$+8YSZ are also worse. Following hot corrosion, the emergence of interplay cracks, horizontal fissures, and localised chemical heterogeneity is always observed. The **Fig. 2.6** SEM images indicate this trend, with the degradation being more widespread than in the La-based system. Elemental analysis also reveals that the penetration of sodium in $Gd_2Zr_2O_7$+8YSZ is considerably higher, which encourages local disintegration of the pyrochlore structure **[55],[62]**.

2.5.2 Hot Corrosion Behaviour of $Sm_2Zr_2O_7$+8YSZ Coatings

The family of rare-earth zirconates, $Sm_2Zr_2O_7$, has been considered a co-phase with 8YSZ due to its low thermal conductivity and structural resemblance to other pyrochlore systems. When applied as a dual-phase coating, $Sm_2Zr_2O_7$ + 8YSZ was initially considered a promising candidate for thermal barrier coatings operating in high-temperature gas turbine environments. It has, however, been reported that this system is significantly deteriorated, especially in the presence of corrosive salts such as Na_2SO_4, particularly against $La_2Zr_2O_7$-based composites. The X-ray diffraction measurements following exposure to hot corrosion processes consistently show that the pyrochlore form of $Sm_2Zr_2O_7$ is less stable in interaction with molten sodium sulfate. Several studies have shown a gradual weakening of the characteristic pyrochlore reflections accompanied by the appearance of new peaks corresponding to fluorite-like or other destabilised phases. This behaviour indicates that the Sm-containing pyrochlore is more reactive towards sodium salts, causing chemical destabilisation and structural change. **Fig. 2.7** illustrates a typical example of this behaviour, in which post-corrosion testing XRD patterns clearly reveal the following: pyrochlore peaks decrease, and there is the development of secondary phases. These results indicate that the phase stability of $Sm_2Zr_2O_7$+8YSZ in the presence of corrosive conditions is inferior to that of the $Sm_2Zr_2O_7$+8YSZ coating, which, in most cases, retains its main phases even after prolonged exposure.

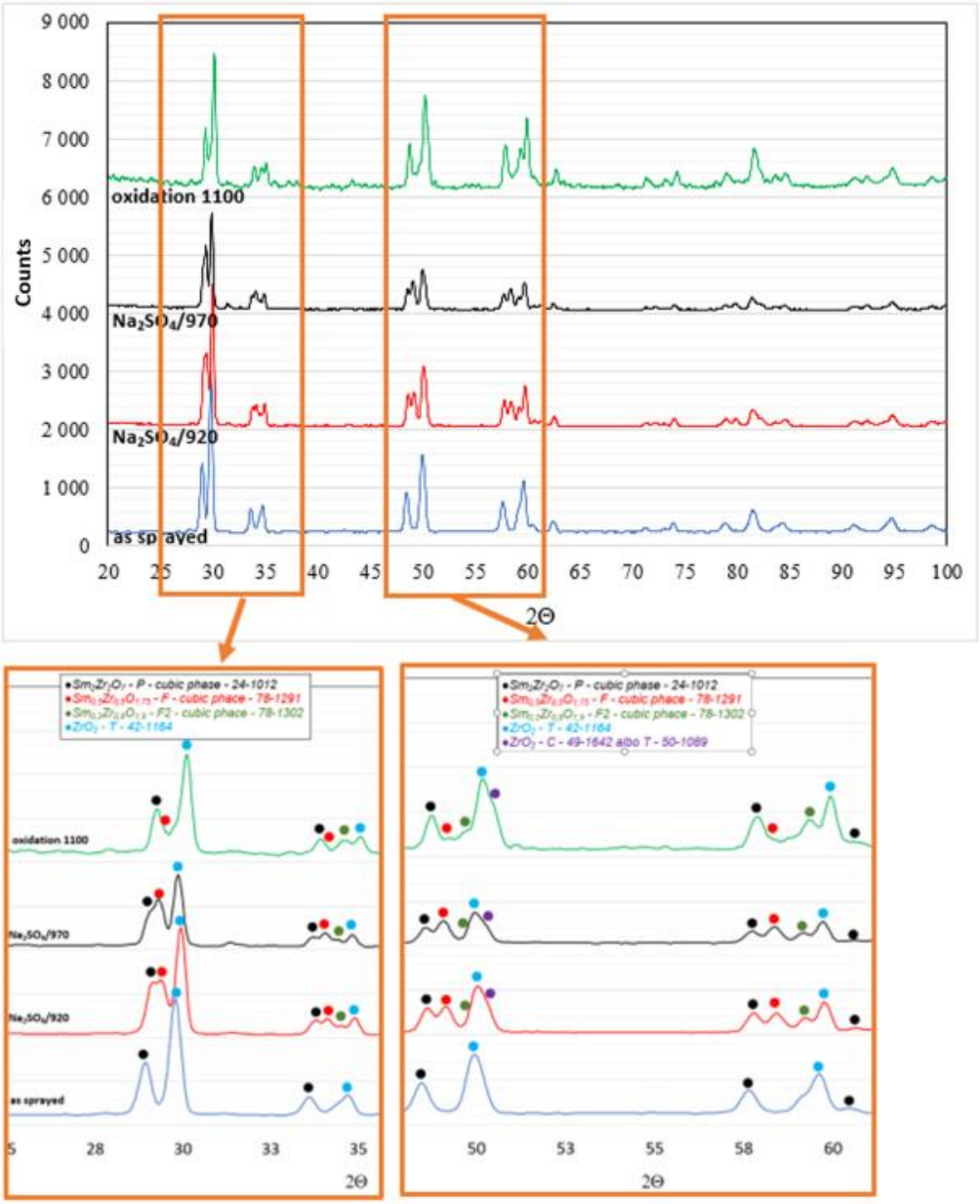

Figure 2.7: XRD patterns for 50 8YSZ + 50 $Sm_2Zr_2O_7$ TBC system after corrosion test in liquid Na_2SO_4 **[59]**.

At the same time, microstructural analyses are a first-hand indicator of the susceptibility of $Sm_2Zr_2O_7$+8YSZ to hot corrosion. The investigations using SEM have demonstrated that the surface degradation following the attack by Na_2SO_4 is acute, marked by the appearance of cracks, coalescence of pores, and serrated edges of the splats. The attributes are attributed to the fact that molten salt penetrates the porous microstructure via a lamellar structure, which enables chemical reactions on the grain boundaries and accelerates the rate of mechanical weakening. The extent of this damage has been emphasised under **Fig. 2-8** where the deformed

morphology of the surface corrosion of the coating shows unmistakable signs of penetration of molten sodium salt and correlation with microstructural destruction **[59][63]**.

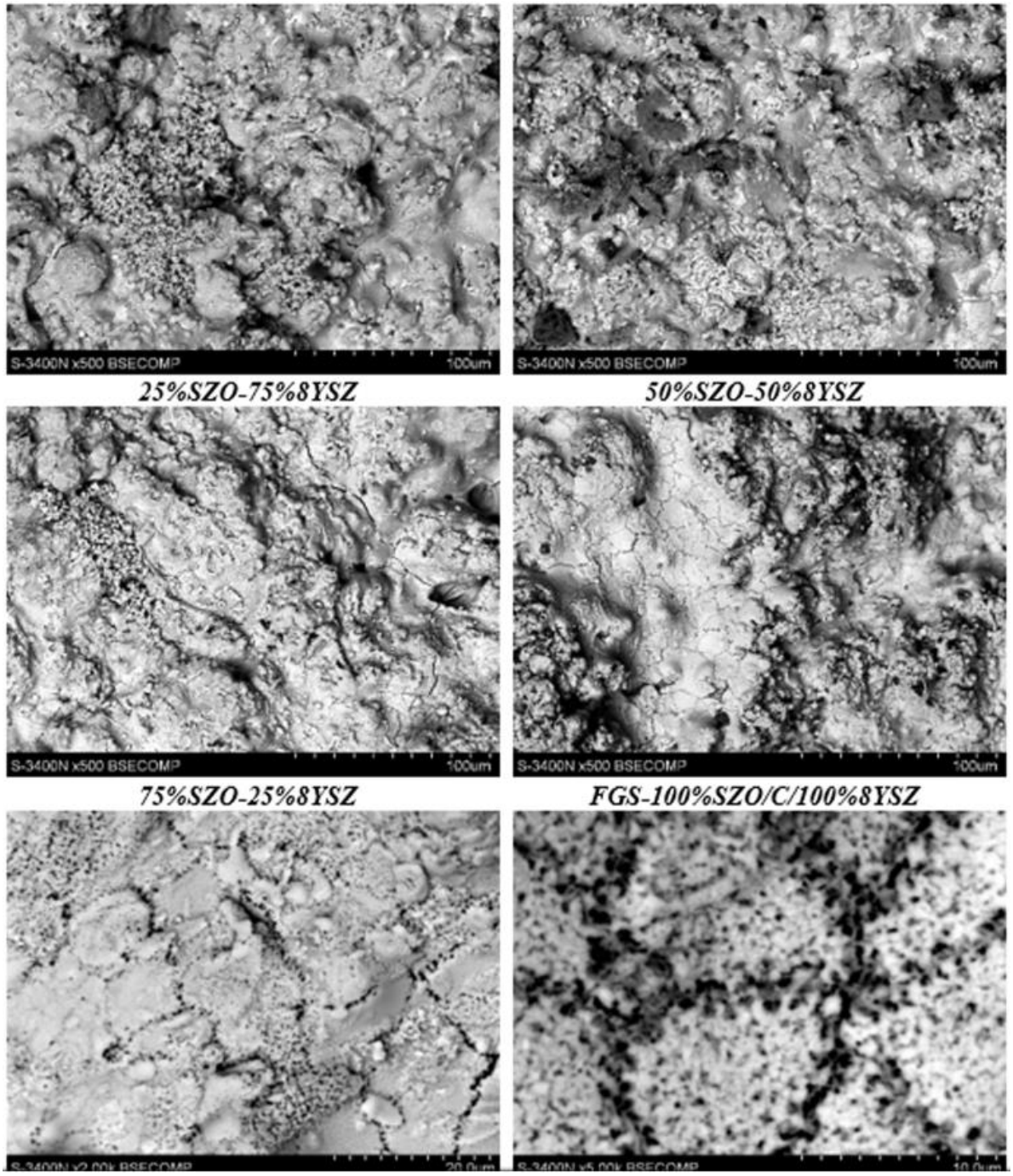

Figure 2.8: Surface morphology of TBC coatings after corrosion at 970 °C in liquid Na_2SO_4 salt **[59]**.

2.6 Summary

Chapter 2 summarises the design, material and deposition methodology of thermal barrier coatings (TBCs) and their importance in military operations of metallic components in extreme thermal and chemical conditions. Although yttria-stabilised zirconia (YSZ) has been the conventional material for the ceramic surface layer, its instability at temperatures exceeding 1200 °C (due to sintering and the tetragonal-monoclinic transition) has prompted the search for alternative materials. New materials such as rare-earth zirconates and cerates have been shown to be promising due to their reduced thermal conductivity, increased melting temperature, and better phase stability with dual phase composites, adding further to their thermomechanical compatibility. Different deposition techniques, such as APS, EB-PVD, SPS, and PS-PVD, have been developed to tailor the microstructure and improve coating performance; however, degradation mechanisms, including thermal fatigue, bond coat oxidation, hot corrosion, and CMAS infiltration, remain limiting factors for long-term durability. Among these, hot corrosion is particularly damaging, with molten salts such as Na_2SO_4 and V_2O_5 widely studied for their destabilising effects on TBCs. However, significantly less attention has been given to the influence of MgSO4-containing environments, although Na_2SO_4–$MgSO_4$ mixtures form low-melting eutectics (~660 °C) that create far more aggressive and realistic corrosive conditions for turbine applications. Furthermore, there is a marked lack of systematic studies on the hot corrosion behaviour of neodymium-based cerates ($Nd_2Ce_2O_7$), both as single-phase coatings and as dual phase composites with YSZ, even though ceria incorporation can strongly influence oxygen transport, phase evolution, and molten salt interactions. This evident deficiency in the available literature, particularly regarding MgSO4-induced corrosion and the unexplored stability of $Nd_2Ce_2O_7$-based systems, forms the central research gap addressed in the present work, motivating the investigation of $Nd_2Zr_2O_7$, $Nd_2Ce_2O_7$, and their dual phase composites with YSZ under complex sulphate vanadate environments to develop next-generation TBCs with enhanced phase stability and hot corrosion resistance.

References

[1] K. Parthiban, P. Roy, and S. Ghosh, "Hot Corrosion Behaviour of Three-Layered Functionally Graded Glass–ceramic–YSZ-based Thermal Barrier Coating System," *Trans. Indian Inst. Met.*, vol. 77, no. 5, pp. 1407–1412, 2024, doi: 10.1007/s12666-023-03073-2.

[2] M. Yoshiba, K. Abe, T. Aranami, and Y. Harada, "High-temperature oxidation and hot corrosion behavior of two kinds of thermal barrier coating systems for advanced gas turbines," *J. Therm. Spray Technol.*, vol. 5, no. 3, pp. 259–268, 1996, doi: 10.1007/BF02645876.

[3] C. Holländer *et al.*, "Hot corrosion of TBC-coated components upon combustion of low-sulfur fuels," *Mater. Corros.*, vol. 72, no. 10, pp. 1643–1655, 2021, doi: 10.1002/maco.202112371.

[4] Y. Ozgurluk, K. M. Doleker, H. Ahlatci, and A. C. Karaoglanli, "Investigation of hot corrosion behavior of thermal barrier coating (TBC) systems with rare earth contents," *Arab. J. Geosci.*, vol. 11, no. 11, pp. 2017–2019, 2018, doi: 10.1007/s12517-018-3625-0.

[5] S. K, N. Babu, S. Govindarajan, and S. B. Arya, "Hot corrosion behaviour of mullite thermal barrier coatings for marine diesel engines," *Ceram. Int.*, vol. 50, no. 2, pp. 2808–2818, 2024, doi: 10.1016/j.ceramint.2023.11.001.

[6] A. Mehta and H. Vasudev, "A Review on the Thermal Barrier Coatings in Hot Corrosion Protection: Innovations and Future Directions for High-Temperature Alloys," *J. Fail. Anal. Prev.*, vol. 25, no. 3, pp. 1003–1039, 2025, doi: 10.1007/s11668-025-02185-9.

[7] X. Zhou *et al.*, "Hot corrosion behaviour of La2(Zr0.7Ce0.3)2O7 thermal barrier coating ceramics exposed to molten calcium magnesium aluminosilicate at different temperatures," *Corros. Sci.*, vol. 100, pp. 566–578, 2015, doi: 10.1016/j.corsci.2015.08.031.

[8] Q. Liu, S. Huang, and A. He, "Composite ceramics thermal barrier coatings of yttria stabilized zirconia for aero-engines," *J. Mater. Sci. Technol.*, vol. 35, no. 12, pp. 2814–2823, 2019, doi: 10.1016/j.jmst.2019.08.003.

[9] H. Vakilifard, R. Ghasemi, and M. Rahimipour, "Hot corrosion behaviour of plasma-sprayed functionally graded thermal barrier coatings in the presence of Na2SO4 + V2O5 molten salt," *Surf. Coatings Technol.*, vol. 326, pp. 238–246, 2017, doi: 10.1016/j.surfcoat.2017.07.058.

[10] M. J. Moaveni, H. Omidvar, M. Farvizi, and S. M. H. Mirbagheri, "Hot corrosion behavior of Y2O3-doped lanthanum zirconate TBCs in Na2SO4+V2O5 environment," *Ceram. Int.*, vol. 51, no. 18, pp. 25078–25093, 2025, doi: 10.1016/j.ceramint.2025.03.190.

[11] A. R. Patil and S. T. Vagge, "Oxidation and hot corrosion behaviour of functionally graded yttria stabilized zirconia and lanthanum zirconate thermal barrier coatings," *Surf. Coatings Technol.*, vol. 474, no. September, p. 130059, 2023, doi: 10.1016/j.surfcoat.2023.130059.

[12] K. Mondal, L. Nuñez, C. M. Downey, and I. J. Van Rooyen, “Thermal barrier coatings overview: Design, manufacturing, and applications in high-temperature industries,” *Ind. Eng. Chem. Res.*, vol. 60, no. 17, pp. 6061–6077, 2021, doi: 10.1021/acs.iecr.1c00788.

[13] A. Iqbal and G. Moskal, *Recent Development in Advance Ceramic Materials and Understanding the Mechanisms of Thermal Barrier Coatings Degradation*, vol. 30, no. 8. Springer Netherlands, 2023. doi: 10.1007/s11831-023-09960-7.

[14] X. Wei *et al.*, “Effect of doping CeO2 and Sc2O3 on structure, thermal properties and sintering resistance of YSZ,” *Ceram. Int.*, vol. 47, no. 5, pp. 6875–6883, 2021, doi: 10.1016/j.ceramint.2020.11.032.

[15] S. Jucha, G. Moskal, M. Mikuśkiewicz, and M. Stopyra, “Calorimetric study of Eu2O3–ZrO2 feedstock powders and sintered materials,” *J. Therm. Anal. Calorim.*, vol. 126, no. 3, pp. 1015–1021, 2016, doi: 10.1007/s10973-016-5816-9.

[16] Z. Y. Wei *et al.*, “Progress in ceramic materials and structure design toward advanced thermal barrier coatings,” *J. Adv. Ceram.*, vol. 11, no. 7, pp. 985–1068, 2022, doi: 10.1007/s40145-022-0581-7.

[17] R. Gadow and M. Lischka, “Lanthanum hexaaluminate - Novel thermal barrier coatings for gas turbine applications - Materials and process development,” *Surf. Coatings Technol.*, vol. 151–152, pp. 392–399, 2002, doi: 10.1016/S0257-8972(01)01642-5.

[18] J. Zeng *et al.*, “Heat-treated lanthanum magnesium hexaaluminate coatings exposed to molten calcium-magnesium-alumino-silicate,” *Ceram. Int.*, vol. 45, no. 9, pp. 11723–11733, 2019, doi: 10.1016/j.ceramint.2019.03.048.

[19] M. G. Gok and G. Goller, “Microstructural characterization of GZ/CYSZ thermal barrier coatings after thermal shock and CMAS+hot corrosion test,” *J. Eur. Ceram. Soc.*, vol. 37, no. 6, pp. 2501–2508, 2017, doi: 10.1016/j.jeurceramsoc.2017.02.004.

[20] X. Ma, K. Rivellini, P. Ruggiero, and G. Wildridge, “Novel Thermal Barrier Coatings with Phase Composite Structures for Extreme Environment Applications: Concept, Process, Evaluation and Performance,” *Coatings*, vol. 13, no. 1, 2023, doi: 10.3390/coatings13010210.

[21] C. S. Ramachandran, V. Balasubramanian, and P. V. Ananthapadmanabhan, “On the cyclic hot corrosion behaviour of atmospheric plasma sprayed Lanthanum Zirconate based coatings in contact with a mixture of sodium sulphate and vanadate salts: A comparison with the traditional Ysz duplex and NiCrAlY coated samples,” *Vacuum*, vol. 97, pp. 81–95, 2013, doi: 10.1016/j.vacuum.2013.03.020.

[22] G. Bhavesh, P. Hariharan, and D. Dhinasekaran, “Assessment of the microstructural features and electrochemical corrosion behaviour of nanostructured Gd2Zr2O7 EB-PVD TBCs under three salt conditions,” *Surf. Coatings Technol.*, vol. 487, no. April, p. 130991, 2024, doi: 10.1016/j.surfcoat.2024.130991.

[23] J. Song, L. Wang, J. Yao, and H. Dong, “Multi-Scale Structural Design and Advanced Materials for Thermal Barrier Coatings with High Thermal Insulation: A Review,” *Coatings*, vol. 13, no. 2, 2023, doi: 10.3390/coatings13020343.

[24] R. Vaßen, E. Bakan, D. E. Mack, and O. Guillon, “A Perspective on Thermally Sprayed Thermal Barrier Coatings: Current Status and Trends,” *J. Therm. Spray Technol.*, vol. 31, no. 4, pp. 685–698, 2022, doi: 10.1007/s11666-022-01330-2.

[25] A. Iqbal, G. Moskal, and B. Witala, “Degradation mechanism of dual-phase thermal barrier coatings Gd 2 Zr 2 O 7 + 8YSZ under hot corrosion ambience Na 2 SO 4,” 2024, [Online]. Available: https://ssrn.com/abstract=4617181

[26] G. Mehboob *et al.*, “Tailoring periodic vertical cracks in thermal barrier coatings enabling high strain tolerance,” *Coatings*, vol. 11, no. 6, 2021, doi: 10.3390/coatings11060720.

[27] W. Fan and Y. Bai, “Review of suspension and solution precursor plasma sprayed thermal barrier coatings,” *Ceram. Int.*, vol. 42, no. 13, pp. 14299–14312, 2016, doi: 10.1016/j.ceramint.2016.06.063.

[28] X. Zhang *et al.*, “Al2O3-modified PS-PVD 7YSZ thermal barrier coatings for advanced gas-turbine engines,” *npj Mater. Degrad.*, vol. 4, no. 1, pp. 1–6, 2020, doi: 10.1038/s41529-020-00134-5.

[29] G. Mauer and R. Vaßen, “Coatings with Columnar Microstructures for Thermal Barrier Applications,” *Adv. Eng. Mater.*, vol. 22, no. 6, pp. 1–9, 2020, doi: 10.1002/adem.201900988.

[30] A. Miller, B. A. Nagaraj, and W. Bruce, “Barrier Laser Conductivity Coatings Heat Flux of EB-PVD Thermal Evaluated Technique by a Steady-State,” no. July, 2000.

[31] M. Bellippady *et al.*, “Characteristics and performance of suspension plasma sprayed thermal barrier coatings on additively manufactured superalloy substrates,” *Surf. Coatings Technol.*, vol. 472, no. June, 2023, doi: 10.1016/j.surfcoat.2023.129926.

[32] M. J. Liu *et al.*, “Plasma spray–physical vapor deposition toward advanced thermal barrier coatings: a review,” *Rare Met.*, vol. 39, no. 5, pp. 479–497, 2020, doi: 10.1007/s12598-019-01351-x.

[33] M. P. Schmitt, B. J. Harder, and D. E. Wolfe, “Process-structure-property relations for the erosion durability of plasma spray-physical vapor deposition (PS-PVD) thermal barrier coatings,” *Surf. Coatings Technol.*, vol. 297, pp. 11–18, 2016, doi: 10.1016/j.surfcoat.2016.04.029.

[34] G. Mehboob, M. J. Liu, T. Xu, S. Hussain, G. Mehboob, and A. Tahir, “A review on failure mechanism of thermal barrier coatings and strategies to extend their lifetime,” *Ceram. Int.*, vol. 46, no. 7, pp. 8497–8521, 2020, doi: 10.1016/j.ceramint.2019.12.200.

[35] D. R. Mumm and G. A. Evans, “Mechanisms controlling the performance and durability of thermal barrier coatings,” *Key Eng. Mater.*, vol. 197, pp. 199–230, 2001, doi: 10.4028/www.scientific.net/kem.197.199.

[36] L. Mahfouz *et al.*, “Thermal Barrier Coatings in burner rig experiment analyzed through LAser Shock for DAmage Monitoring (LASDAM) method,” *J. Eur. Ceram. Soc.*, vol. 44, no. 13, pp. 7867–7882, 2024, doi: 10.1016/j.jeurceramsoc.2024.05.001.

[37] D. Chen, C. Dambra, and M. Dorfman, “Deposition, Microstructure and Thermal Cycling Performance of Strain-Tolerant Thermal Barrier Coatings,” *J. Therm. Spray Technol.*, vol. 32, no. 4, pp. 1108–1114, 2023, doi: 10.1007/s11666-022-01516-8.

[38] F. A. Zhao, H. Y. Xiao, X. M. Bai, Z. J. Liu, and X. T. Zu, “Effects of doping Yb3+, La3+, Ti4+, Hf4+, Ce4+ cations on the mechanical properties, thermal conductivity, and electronic structures of Gd2Zr2O7,” *J. Alloys Compd.*, vol. 776, pp. 306–318, 2019, doi: 10.1016/j.jallcom.2018.10.240.

[39] L. Zhang *et al.*, “Effect of the non-uniformed growth of TGO on dynamic stress evolution in realistic TC/TGO interface of MCrAlY-YSZ TBCs during thermal cycling,” *Surf. Coatings Technol.*, vol. 511, no. May, 2025, doi: 10.1016/j.surfcoat.2025.132319.

[40] A. Miller, “Thermal Evolution Under Conductivity of Thermal Heat and Elastic Modulus Barrier Coatings High,” no. April, 1999.

[41] A. M. Limarga, S. Shian, M. Baram, and D. R. Clarke, “Effect of high-temperature aging on the thermal conductivity of nanocrystalline tetragonal yttria-stabilized zirconia,” *Acta Mater.*, vol. 60, no. 15, pp. 5417–5424, 2012, doi: 10.1016/j.actamat.2012.06.054.

[42] S. R. Choi, D. Zhu, and R. A. Miller, “Effect of sintering on mechanical properties of plasma-sprayed zirconia-based thermal barrier coatings,” *J. Am. Ceram. Soc.*, vol. 88, no. 10, pp. 2859–2867, 2005, doi: 10.1111/j.1551-2916.2005.00504.x.

[43] W. R. Chen, X. Wu, B. R. Marple, and P. C. Patnaik, “The growth and influence of thermally grown oxide in a thermal barrier coating,” *Surf. Coatings Technol.*, vol. 201, no. 3–4, pp. 1074–1079, 2006, doi: 10.1016/j.surfcoat.2006.01.023.

[44] W. R. Chen, X. Wu, B. R. Marple, D. R. Nagy, and P. C. Patnaik, “TGO growth behaviour in TBCs with APS and HVOF bond coats,” *Surf. Coatings Technol.*, vol. 202, no. 12, pp. 2677–2683, 2008, doi: 10.1016/j.surfcoat.2007.09.042.

[45] J. Zygmuntowicz, P. Wiecińska, A. Miazga, and K. Konopka, “Characterization of composites containing NiAl2O4 spinel phase from Al2O3/NiO and Al2O3/Ni systems,” *J. Therm. Anal. Calorim.*, vol. 125, no. 3, pp. 1079–1086, 2016, doi: 10.1007/s10973-016-5357-2.

[46] H. F. Chen *et al.*, “Recent progress in thermal/environmental barrier coatings and their corrosion resistance,” *Rare Met.*, vol. 39, no. 5, pp. 498–512, 2020, doi: 10.1007/s12598-019-01307-1.

[47] S. L. Silyakov, V. I. Yukhvid, V. A. Gorshkov, T. I. Ignat’eva, N. V. Sachkova, and N. Y. Khomenko, “Chemical and Phase Transformations in the Combustion of a CrO3/AlN Mixture,” *Combust. Explos. Shock Waves*, vol. 54, no. 2, pp. 165–169, 2018, doi: 10.1134/S0010508218020053.

[48] X. Wan *et al.*, “Review: hot corrosion mechanisms and corrosion resistance improvement strategies for thermal barrier coatings,” *J. Mater. Sci.*, vol. 60, no. 41, pp. 19484–19513, 2025, doi: 10.1007/s10853-025-11543-9.

[49] R. L. Jones, “Some aspects of the hot corrosion of thermal barrier coatings,” *J. Therm. Spray Technol.*, vol. 6, no. 1, pp. 77–84, 1997, doi: 10.1007/BF02646315.

[50] S. Hu, H. Finklea, and X. Liu, “A review on molten sulfate salts induced hot corrosion,” *J. Mater. Sci. Technol.*, vol. 90, pp. 243–254, 2021, doi: 10.1016/j.jmst.2021.03.013.

[51] B. Salehnasab, E. Poursaeidi, S. A. Mortazavi, and G. H. Farokhian, “Hot corrosion failure in the first stage nozzle of a gas turbine engine,” *Eng. Fail. Anal.*, vol. 60, pp. 316–325, 2016, doi: 10.1016/j.engfailanal.2015.11.057.

[52] Y. Ozgurluk, K. M. Doleker, and A. C. Karaoglanli, “Investigation of the effect of V2O5 and Na2SO4 melted salts on thermal barrier coatings under cyclic conditions,” *Anti-Corrosion Methods Mater.*, vol. 66, no. 5, pp. 644–650, 2019, doi: 10.1108/ACMM-12-2018-2042.

[53] D. A. Shifler, “The increasing complexity of hot corrosion,” *Proc. ASME Turbo Expo*, vol. 1, 2017, doi: 10.1115/1.4038037.

[54] A. Iqbal, G. Moskal, A. Cavaleiro, A. Amjad, and M. J. Khan, “The current advancement of zirconate based dual phase system in thermal barrier coatings (TBCs): New modes of the failures: Understanding and investigations,” *Alexandria Eng. J.*, vol. 91, no. February, pp. 161–196, 2024, doi: 10.1016/j.aej.2024.01.063.

[55] G. Moskal, “Oxidation and Hot Corrosion Behaviour of Dual Phase 8YSZ + La2Zr2O7 and 8YSZ + Gd2Zr2O7 TBC Systems,” *J. Therm. Spray Technol.*, vol. 34, no. 4, pp. 1082–1108, 2025, doi: 10.1007/s11666-025-01978-6.

[56] V. Patarini, N. S. Bornstein, and M. A. DeCrescente, “Hot corrosion of gas turbine components,” *J. Eng. Gas Turbines Power*, vol. 101, no. 1, pp. 177–185, 1979, doi: 10.1115/1.3446441.

[57] L. Guo, X. Zhang, M. Liu, S. Yang, and J. W. Dai, “CMAS + sea salt corrosion to thermal barrier coatings,” *Corros. Sci.*, vol. 218, no. December 2022, p. 111172, 2023, doi: 10.1016/j.corsci.2023.111172.

[58] S. Morelli, S. Bursich, V. Testa, G. Bolelli, A. Miccichè, and L. Lusvarghi, “CMAS corrosion and thermal cycling fatigue resistance of alternative thermal barrier coating materials and architectures: A comparative evaluation,” *Surf. Coatings Technol.*, vol. 439, no. April, 2022, doi: 10.1016/j.surfcoat.2022.128433.

[59] G. Moskal, S. Jucha, M. Mikuśkiewicz, D. Migas, and A. Jasik, “Atypical decomposition processes of Sm2Zr2O7 + 8YSZ dual-phase TBCs during hot corrosion,” *Corros. Sci.*, vol. 170, no. December 2019, p. 108681, 2020, doi: 10.1016/j.corsci.2020.108681.

[60] A. Iqbal and G. Moskal, “Investigating degradation in the La2Zr2O7 + YSZ dual-phase innovative system under hot corrosion conditions,” *J. Therm. Anal. Calorim.*, vol. 150, no. 16, pp. 12223–12243, 2025, doi: 10.1007/s10973-025-14349-8.

[61] A. Iqbal, G. Moskal, and B. Witala, “Degradation mechanism of dual-phase thermal barrier coatings Gd2Zr2O7 + 8YSZ under hot corrosion in pure Na2SO4,” *J. Therm. Anal. Calorim.*, vol. 150, no. 1, pp. 151–165, 2025, doi: 10.1007/s10973-024-13784-3.

[62] T. Malurdy, M. Mocek, A. Jasik, and G. Moskal, “Top-surface characterization of La2Zr2O7 + 8YSZ thermal barrier coatings under condition of hot corrosion in liquid Na2SO4 + V2O5 deposits,” *Ochr. Przed Koroz.*, vol. 64, no. 6, pp. 170–176, 2021, doi: 10.15199/40.2021.6.1.

[63] G. Moskal, A. Jasik, M. Mikuśkiewicz, and S. Jucha, “Thermal resistance determination of Sm2Zr2O7 + 8YSZ composite type of TBC,” *Appl. Surf. Sci.*, vol. 515, no. February, p. 145998, 2020, doi: 10.1016/j.apsusc.2020.145998.

Chapter 3: Materials and Methods

Figure 3.1 illustrates a flowchart that visually depicts the materials and methods utilised in this study. This section details the step-by-step process of preparing TBCs to assess their performance in various liquid salt environments. Finally, different experimental techniques were outlined and discussed to gather and interpret the results.

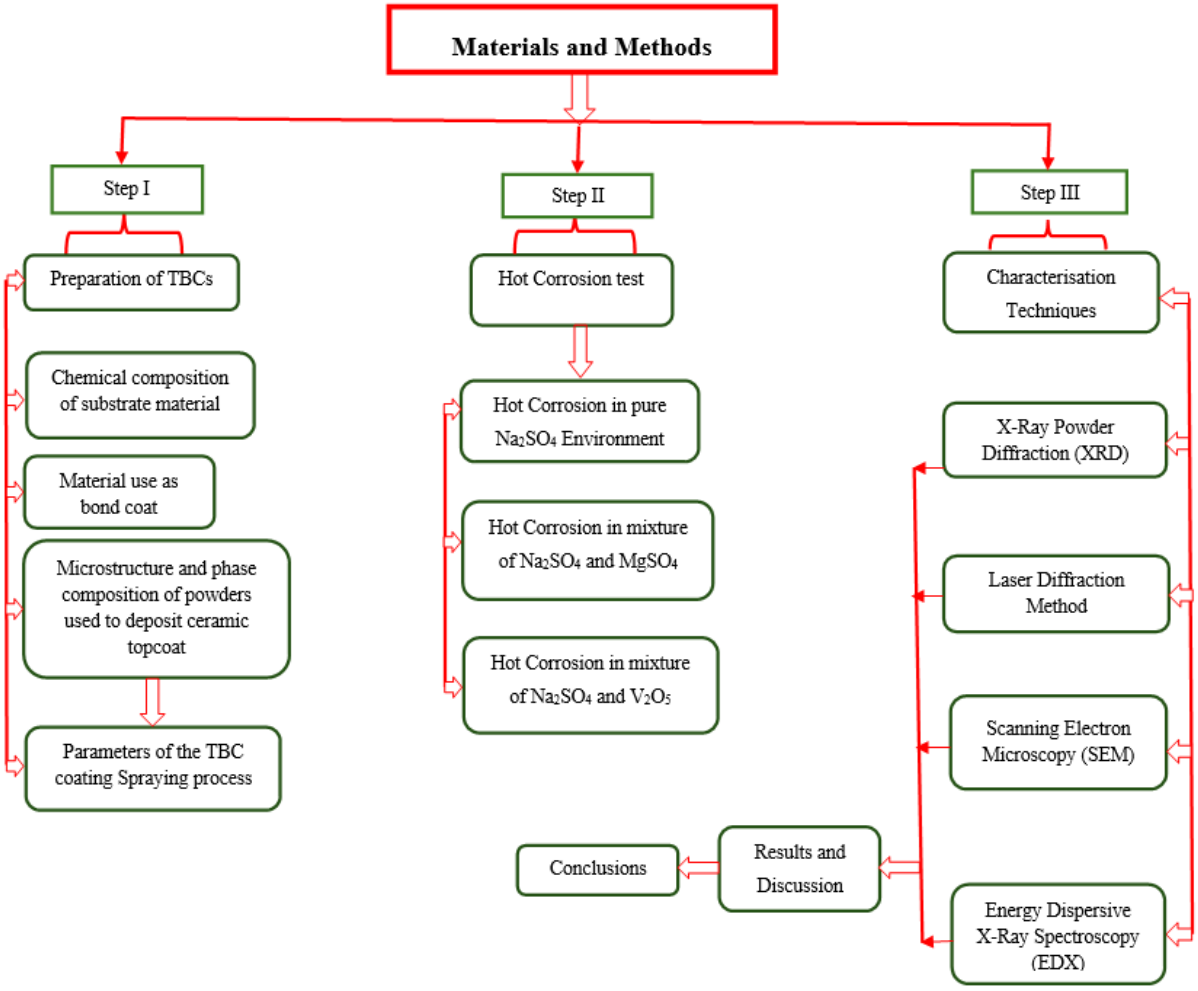

Figure 3.1: Flow chart of the experimental methodology

3.1 Preparation of Coatings (TBCs)

Inconel 625 was the substrate material used in this study, a nickel-based superalloy renowned for its high-temperature strength and corrosion resistance. The detailed chemical composition of the alloy is provided in **Table 1**. Rectangular flat specimens with dimensions of 40 mm × 20 mm × 2 mm were prepared from the alloy sheet to serve as substrates. Before coating deposition, the substrate surfaces were cleaned and roughened by grit blasting with high-purity alumina particles. This surface preparation step removed contaminants and oxides while producing the necessary roughness to improve the adhesion of the thermally sprayed ceramic topcoats. This pretreatment provided high mechanical interlocking at the coating-substrate interface, thus enhancing the performance and durability of the overall thermal barrier coating system.

Table 3.1: Chemical composition of the IN 625 substrate alloy

Wt%	Ni	Cr	Fe	Mo	Co	Nb	Al	Mn	Si	Ti	P	C	S
In 625	60.7	21.67	4.27	8.96	0.07	3.56	0.14	0.07	0.08	0.18	0.007	0.01	0.0003

The bond coat was deposited using a NiCrAlY feedstock (Amdry 962, Oerlikon Metco), which consisted of a metallic powder with a particle size range of 53–106 μm. The choice of this material was based on its excellent resistance to oxidation and hot corrosion, as well as its ability to serve as a compliant material between the substrate and ceramic topcoat. The bond coat deposited had a thickness of approximately 120 μm, providing a uniform and adhesive interlayer.

For the ceramic topcoat, three different powders were employed: neodymium zirconate ($Nd_2Zr_2O_7$), 8 wt.% yttria-stabilised zirconia (8YSZ), and neodymium cerate ($Nd_2Ce_2O_7$). Inframat® Advanced Materials™ synthesised the 8YSZ powder, while Skyworks manufactured the $Nd_2Zr_2O_7$ and $Nd_2Ce_2O_7$ powders. The overall morphology, phase composition, and particle size of the powders used for the ceramic topcoat are shown in **Fig. 3.2** and **Fig. 3.3**. The XRD analysis confirmed that $Nd_2Zr_2O_7$ crystallizes in a cubic pyrochlore phase (JCPDS 78-1618), 8YSZ exhibits a dominant tetragonal zirconia phase with a minor monoclinic contribution (JCPDS 50-1089 and 37-1484), while $Nd_2Ce_2O_7$ shows a stable cubic fluorite structure (JCPDS 75-0156) with the absence of pyrochlore superlattice peaks in the 35°–45° range (2θ). Morphological examination revealed that all powders consist mainly of spherical particles with relatively smooth surfaces. However, some irregularly shaped particles and splats were also observed, which is typical for spray-dried and plasma-treated ceramic

feedstocks. This morphology provides high flowability, making the powders very suitable for deposition using the air plasma spraying (APS) method.

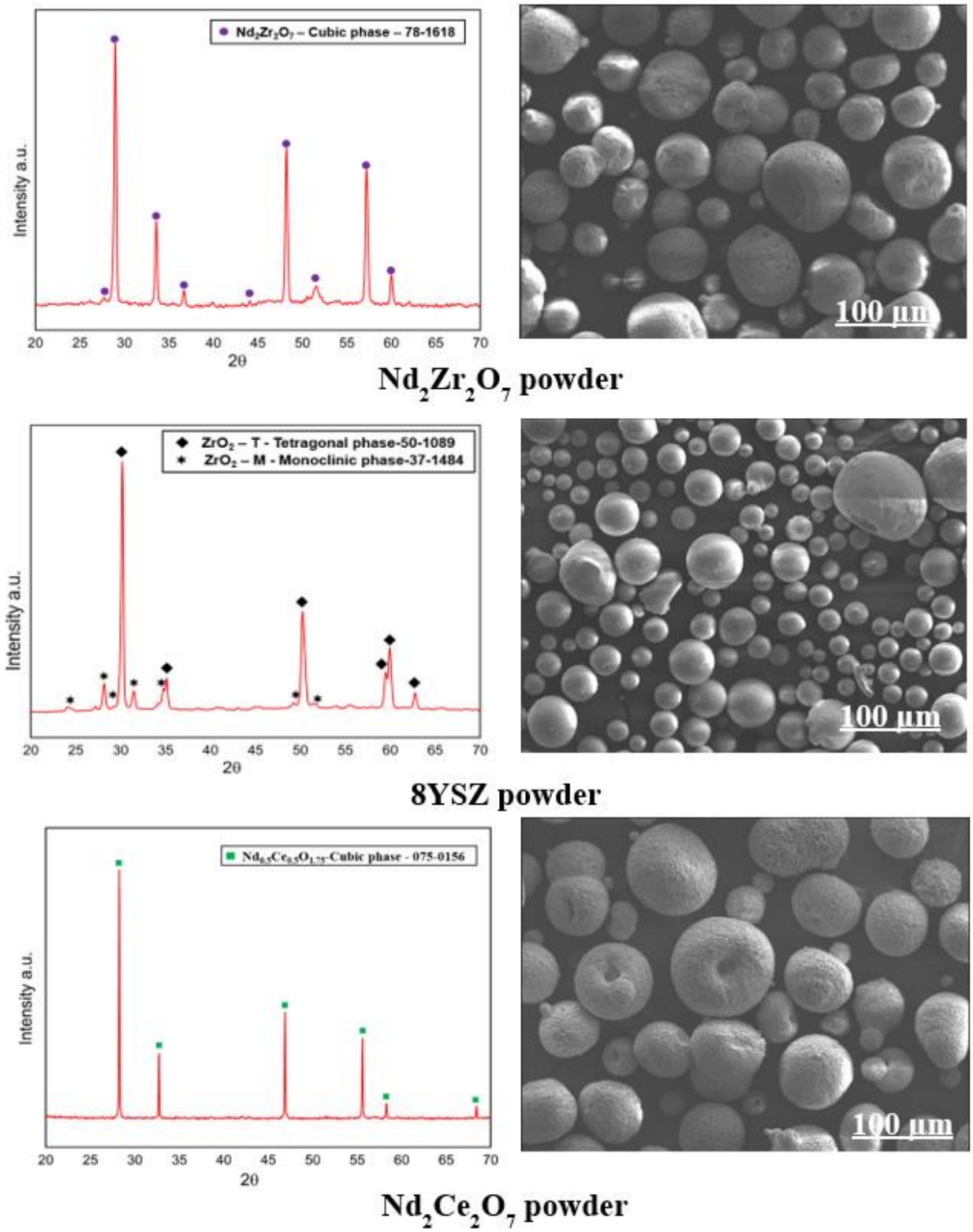

Figure 3.2: Features and XRD patterns of the sprayed powders

As shown in **Fig. 3.3**, the particle size distribution of the powders used for coatings falls within the typical range required for air plasma spraying (APS). For 8YSZ, the particle size was reported to be between ~20–120 µm, with the majority centred around 60–80 µm, while Nd2Zr2O7 powders exhibited a slightly narrower range of ~40–120 µm, with a peak near 90 µm. $Nd_2Ce_2O_7$ exhibited the sharpest distribution, concentrated in the ~40–110 µm range, with a maximum at around 80–90 µm. Mesmerizer analysis in referenced works further confirmed that these powders possess relatively narrow distributions with D_{50} values well suited for APS. Overall, the particle size ranges across all powders are appropriate for plasma spraying, providing good flowability and consistent deposition quality.

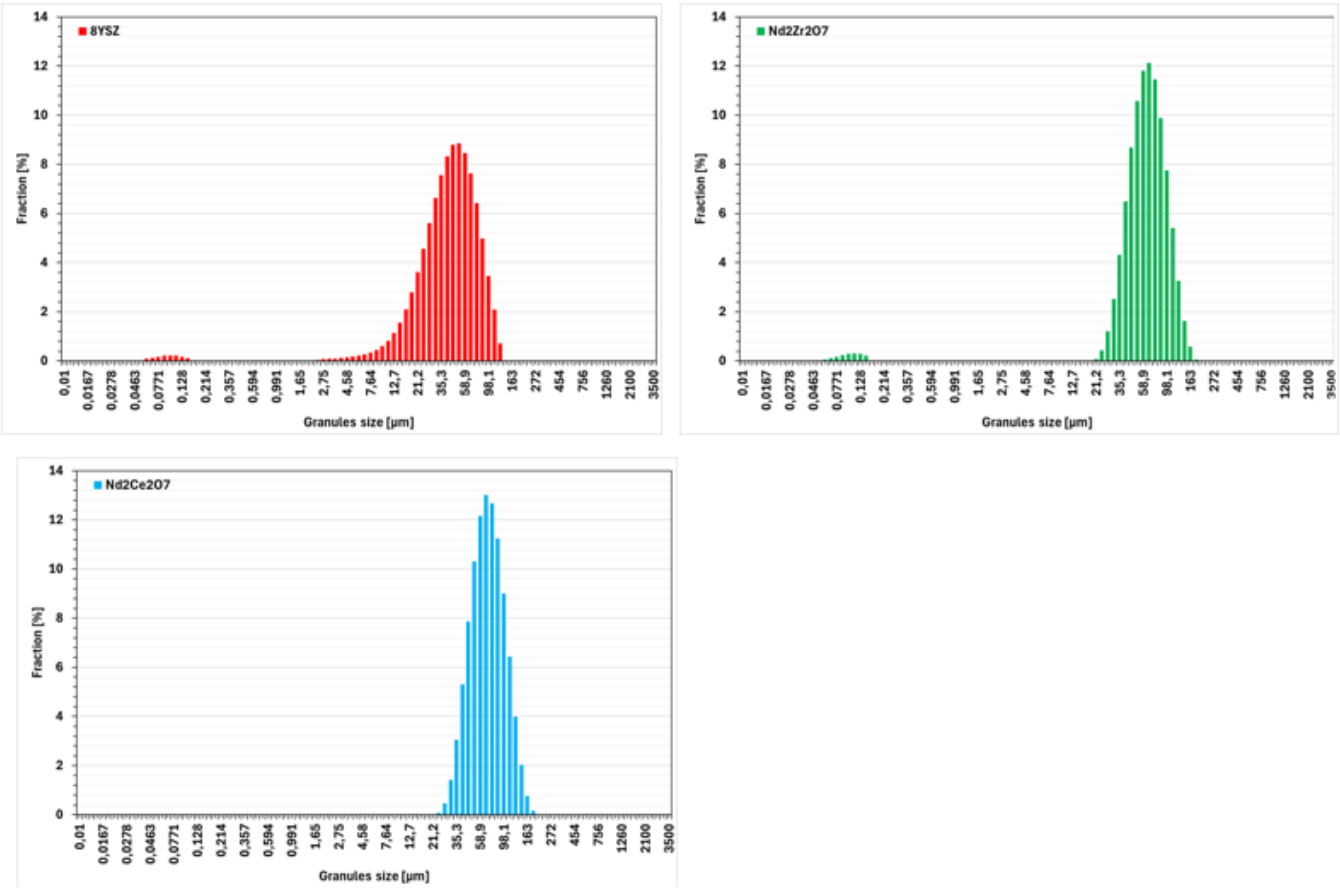

Figure 3.3: Characterization of 8YSZ, $Nd_2Zr_2O_7$ and $Nd_2Ce_2O_7$ powder size distributions

3.2 Deposition Techniques

The Air Plasma Spraying (APS) method is commonly used to deposit thermal barrier coatings in various applications because it provides fine control over the coating thickness and microstructure. In this process, the ceramic powders are injected into a high-temperature plasma jet, where they are melted, and the jet is then directed onto the substrate to create a uniform

layer. Before the spraying process, all feedstock powders were homogenously mixed and dried in a furnace at 100 °C to ensure smooth flow during spraying. Spraying parameters are very important and optimise the quality of coating, and are fine-tuned in the deposition process. The standard parameters are a type F4MB burner, 40 L/min of argon flow, 10 L/min of hydrogen flow, 2.6 L/min of powder carrier gas flow and a powder feeding rate of 15 g/min. The electrical operating conditions generally have a current of 600 A, arc voltage of approximately 61.6 - 62.3 V and burner power of 37.2 - 38.1 kW. Other process controls involve a mixing rate of 60 RPM and 120 RPM rotation, an instrument diameter of 150 mm, and a feed rate of 10 mm/s. The distance between the sprays is usually maintained at 100 mm. For the MCrAlY bond coat, it was decided to apply four program cycles, with a layer thickness of approximately 120 µm. For all ceramic topcoats, the number of program cycles was 8, leading to a coating thickness of approximately 200–275 µm, depending on the system. The following parameters, summarised in Table 2, ensure the stability of the plasma, effective melting of the powder, and high adhesion to the coating.

Table 3.2: TBCs coating spraying process parameters.

Parameters	**Powder type**		
	8YSZ	$Nd_2Zr_2O_7$	$Nd_2Ce_2O_7$
Burner type	F4MB	F4MB	F4MB
argon [l/min]	40	40	40
hydrogen [l/min]	10	10	10
Powder carrier	2,6	2,6	2,6
Powder feeding	15	15	15
Current [A]	600	600	600
Arc voltage [V]	61,6-62,3	61,6-62,3	61,6-62,3
Burner power [kW]	37,2-38,1	37,2-38,1	37,2-38,1
Mixing	60	60	60
Rotation [RPM]	120	120	120
Instrument diameter	150	150	150
Feed [mm/s]	10	10	10
Distance[mm]	100	100	100
Number of program cycles	8	8	8

A schematic of the APS setup is shown in **Figure 3.4**, which illustrates the arrangement of the plasma torch, powder feeder, and substrate movement system, highlighting the interaction zone where molten particles are deposited to form uniform coatings. This setup allows APS to consistently produce high-quality, dense coatings with minimal defects, making it a preferred method for fabricating advanced protective layers.

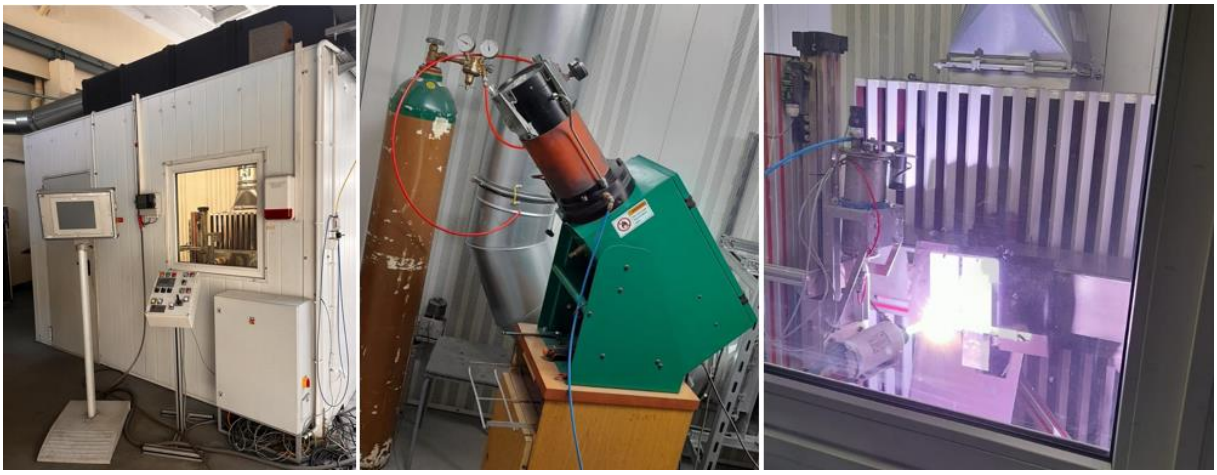

Figure 3.4: Complete APS setup employed for depositing thermal barrier coatings.

3.3 Hot Corrosion Test

The hot corrosion test was conducted to assess the performance of the coatings in aggressive molten salt environments. For this purpose, three types of salts were used: pure Na_2SO_4 (99.0% purity), a 50/50 mol% mixture of Na_2SO_4 and $MgSO_4$ (99.8% purity), and a 50/50 mol% mixture of Na_2SO_4 and V_2O_5 (99.95% purity). The salts were homogeneously blended with ethanol to ensure uniform distribution, and then pressed into small tablets weighing approximately 0.3 mg. Each tablet was carefully positioned at the centre of the coating surface to minimise edge effects and to guarantee controlled contact between the molten salt and the coating.

The corrosion experiments were performed in a LAC LE09/11 muffle furnace (Czech Republic). The specimens were heated at a controlled rate of 10 °C/min until reaching the target temperature of 920 °C, at which point the salts entered their liquid phase. The thermal barrier coating systems were exposed to different corrosion environments for varying durations, all at a temperature of 920°C. The exposure schedule incorporated initial interruptions at 1, 4, and 10 hours, with subsequent repeated test examinations every 24 hours until the maximum test time was reached. The specimens were allowed to cool in the furnace after each heating process to avoid the effects of thermal shock, which were not associated with the corrosion process. As represented in **Table 3.3**, the exposure times for the different environments were as follows: $Nd_2Zr_2O_7$ in Na_2SO_4 for 120 hours, in Na_2SO_4 + $MgSO_4$ (50/50) for 120 hours, and in Na_2SO_4 + V_2O_5 (50/50) for 36 hours; $Nd_2Zr_2O_7$ + 8YSZ (50/50) in Na_2SO_4 for 224 hours, in Na_2SO_4 + $MgSO_4$ (50/50) for 224 hours, and in Na_2SO_4 + V_2O_5 (50/50) for 64 hours; and $Nd_2Ce_2O_7$ +

8YSZ (50/50) in Na_2SO_4 for 168 hours, in Na_2SO_4 + $MgSO_4$ (50/50) for 168 hours, and in Na_2SO_4 + V_2O_5 (50/50) for 48 hours.

Table 3.3: Hot corrosion test parameters and conditions

Thermal Barrier Coating Systems	Corrosion Environment	Time of Exposer	Temperature
$Nd_2Zr_2O_7$	Na_2SO_4	120 h	920 °C
	Na_2SO_4 + $MgSO_4$ (50/50)	120 h	920 °C
	Na_2SO_4 + V_2O_5 (50/50)	36 h	920 °C
$Nd_2Zr_2O_7$ + 8YSZ (50/50)	Na_2SO_4	224 hours	920 °C
	Na_2SO_4 + $MgSO_4$ (50/50)	224 hours	920 °C
	Na_2SO_4 + V_2O_5 (50/50)	64 hours	920 °C
$Nd_2Ce_2O_7$ + 8YSZ (50/50)	Na_2SO_4	168 h	920 °C
	Na_2SO_4 + $MgSO_4$ (50/50)	168 h	920 °C
	Na_2SO_4 + V_2O_5 (50/50)	48 h	920 °C

3.4 Characterisation Techniques

To fully understand the performance of thermal barrier coatings under hot corrosion conditions, it is essential to apply a combination of advanced characterisation techniques. Such techniques give complementary data on the physical, chemical, and geometrical characteristics of the feedstock powders, as well as the deposited coatings. The powders themselves, and in particular their particle size distribution, have a direct effect on the behaviour of coating deposition during air plasma spraying. In the same manner, the phase arrangement of the coatings, both before and after exposure, needs to be determined to monitor their structural stability and potential changes under high-temperature conditions. Essential features of microstructural analysis include porosity, splat morphology and defect formation, whereas chemical analysis is used to explain compositional variation during degradation. These methods, when combined, determine a good correlation between the processing environment, microstructure, and the corrosion resistance of the coatings.

3.4.1 Particle Size Distribution (PSD) – Laser Diffraction

The particle size distribution (PSD) of the feedstock powders was determined to assess their suitability for the air plasma spraying process. The NanoTec Analysette 22 laser diffraction analyser was used to measure them (Fritsch, Germany). The wet dispersion technique was employed, ensuring a homogeneous suspension of powder particles in the measurement, thereby minimising agglomeration. The theory of the Fraunhofer diffraction was used in the analysis, a proven method of characterising an extensive array of particles. A wide range of

measurements for PSD was 0.1-504.48 μm, allowing for the observation of both fine and coarse fractions. Each sample was measured 100 times to enhance accuracy and reproducibility, and the procedure was repeated three times in each powder batch. The reason behind this technique is that the PSD of the powders directly determines the flowability of the feedstock and subsequently affects the melting behaviour of the powders within the plasma jet, leading to the final quality and uniformity of the deposited coating.

3.4.2 X-ray Diffraction (XRD)

X-ray diffraction (XRD) was used to analyse the phase composition and structural properties of the as-sprayed coating and the post-hot corrosion testing specimens. A Philips X'Pert3 Powder diffractometer, fitted with a copper anode tube ($\lambda CuK\alpha$ = 1.54178 Å), was used to measure the samples. The diffractometer was set at 40 kV and 30 mA, which was considered sufficient to produce high-quality diffraction patterns due to the intensity of the X-ray beam. The data were collected over a 2θ range of 10°–90° with a step size of 0.02°, and detailed information on the crystalline phases present in the coatings was obtained. A small step size permitted the precise determination of small peaks and insignificant phase changes. The patterns of diffraction obtained were analysed using crystallographic databases and software to determine the phases and assess probable alterations following hot corrosion. The key objectives of XRD analysis were to determine the stability of the crystalline phases, the decomposition of any new phase, and the integrity of the structure under high-temperature, corrosive conditions.

3.4.3 Scanning Electron Microscopy and Energy-Dispersive Spectroscopy (SEM/EDS)

Scanning electron microscopy (SEM) and energy-dispersive X-ray spectroscopy (EDS) were used to study the microstructure, morphology, and elemental composition of the coating. The imaging was performed using a Hitachi 3400N SEM, which provided both secondary electron (SE) and backscattered electron (BSE) imaging features and was capable of determining both the surface and cross-sectional features of the coatings. A Thermo Noran System Six EDS detector was installed in the SEM, allowing for compositional analysis of the chosen microstructural areas. To obtain the specimens used in SEM analysis, the coated specimens were sectioned with a precision saw, placed in cold-setting resin, and then subjected to stepwise grinding and polishing with diamond suspensions of 9, 3, and 1 μm to obtain a smooth surface with no defects. Surface morphology, splat boundaries, porosity distribution, coating thickness uniformity, and crack or defect formation were studied under SEM, both prior to and after exposure to hot corrosion. Qualitative and semi-quantitative chemical analysis was done using

the EDS system, which was used to identify the distribution of key elements in the coating system and corrosion products in the form of elemental maps and spot analysis. The combination of SEM and EDS provided supplementary information: whereas SEM could reveal structural aspects and failure modes, EDS confirmed the chemical nature of the observed phases. This combined method was critical in order to match microstructural degradation to changes in composition that occur in corrosive high-temperature conditions.

3.5 Summary

- Thermal barrier coatings (TBCs) were prepared on Inconel 625 substrates, which were grit-blasted before applying a NiCrAlY bond coat followed by ceramic topcoats of $Nd_2Zr_2O_7$, 8YSZ, or $Nd_2Ce_2O_7$.
- The ceramic powders were characterised by XRD and morphology analysis, confirming their respective cubic pyrochlore, tetragonal/monoclinic, and cubic fluorite phases, with spherical particle shapes suitable for APS deposition.
- Air Plasma Spraying (APS) was used to deposit both bond and topcoats, employing F4MB torch conditions (40 L/min Ar, 10 L/min H_2, 600 A, ~62 V, 15 g/min feed), producing ~120 µm bond coats and ~200–275 µm ceramic layers.
- Hot corrosion testing was conducted at 920 °C using three salt environments: pure Na_2SO_4, Na_2SO_4–$MgSO_4$ (50/50), and Na_2SO_4–V_2O_5 (50/50), with exposure durations up to 224 h (or 64 h for V_2O_5).
- Particle size distribution of feedstock powders was measured by laser diffraction, using wet dispersion over a 0.1–504 µm range with repeated cycles to ensure accuracy.
- Post-deposition and post-corrosion characterisation employed XRD, SEM, and EDS, enabling phase identification, microstructural observation, and elemental mapping to evaluate degradation and coating performance.

Chapter 4: Thesis and Objectives of the Work

Based on literature research that highlights gaps in knowledge regarding thermal barrier coatings, particularly two-phase composite coatings of the $Ln_2Zr_2O_7$ + 8YSZ or $Ln_2Ce_2O_7$ + 8YSZ type, especially their corrosion resistance in liquid sulfate salt deposits with and without vanadium oxide, the following thesis was proposed for this doctoral dissertation.

Thermal barrier coatings with a composite two-phase ceramic insulating layer of $Nd_2Zr_2O_7$ + 8YSZ and $Nd_2Ce_2O_7$ + 8YSZ are expected to exhibit higher durability under hot corrosion test conditions compared to traditional single-phase TBC systems. This is due to the increased stress compensation capacity and, consequently, better deformation tolerance (fracture toughness) of two-phase systems. This phenomenon is related to previously unidentified degradation mechanisms in two-phase systems, involving interactions between the pyrochlore/fluorite phase and 8YSZ, which lead to the formation of non-stoichiometric phases and numerous ultrafine voids. These voids help to compensate for the nucleation and growth of microcracks. As a result, it will be possible to develop TBC systems resistant to macroscopic cracking and spallation of the ceramic layer. The intensity of decomposition of the initial phases, $Nd_2Zr_2O_7$ and $Nd_2Ce_2O_7$, will depend on the compositions of the sulphate salts used in the study, especially their tendency to form low-melting eutectics that speed up the decomposition process.

To demonstrate this, the following studies will be undertaken:

- Evaluation of the high-temperature corrosion resistance of $Nd_2Zr_2O_7$-type TBC systems and the composite systems: $Nd_2Zr_2O_7$ + 8YSZ and $Nd_2Ce_2O_7$ + 8YSZ in an environment of liquid Na_2SO_4 salt deposits, a Na_2SO_4 + $MgSO_4$ salt mixture, and Na_2SO_4 salt with added V_2O_5;

- Studies of the phase composition of the TBC systems at individual stages of corrosion resistance testing.

- Studies of the surface layer condition of the analysed systems and their cross-sectional sections.

These studies are aimed at achieving specific objectives:

- Determining the factors determining the durability of the TBC systems under the test conditions.

- Determining the microstructural and phase composition changes in the tested TBC systems induced by temperature and environmental factors.

- Determining the microstructural mechanisms influencing the degradation process of the tested TBC systems.

- Identification of mechanisms determining the course of corrosion processes and their reference to generally available knowledge in the field of high-temperature corrosion processes of TBC systems based on rare-earth zirconates and cerates.

Chapter 5: Effect of Molten Sulfate and Vanadate Salts on the Hot Corrosion Behaviour of Single-Layered $Nd_2Zr_2O_7$ Thermal Barrier Coatings

5.1 Abstract

The performance and lifetime of thermal barrier coatings (TBCs) in gas turbine engines are strongly influenced by their resistance to hot corrosion from molten salts generated during fuel combustion. The study of hot corrosion behaviour of Air plasma-sprayed $Nd_2Zr_2O_7$ (NZO) coatings was conducted under three corrosive conditions, which included the following: Na_2SO_4, Na_2SO_4 + $MgSO_4$, and Na_2SO_4 + V_2O_5. The analysis of the evolution of phases and microstructural gradual degradation relied on XRD, SEM, and EDS. Findings indicate that NZO is partially stable in Na_2SO_4, and the early development of monoclinic ZrO_2 and sodium-based oxides is obtained. In Na_2SO_4+$MgSO_4$ deposits, eutectic reactions at ~660 °C promoted extensive grain boundary attack and microcracking, accompanied by the emergence of $Nd_2(SO_4)_3$ and MgO. In the Na2SO4 + V2O5 environment, the worst degradation occurred, and the pyrochlore phase rapidly decomposed, resulting in the crystallisation of $NdVO_4$, the formation of monoclinic zirconia, and coating failure within short time periods. These findings establish the corrosion mechanisms governing NZO under different salt chemistries and emphasise the critical vulnerability of the coating to vanadate-induced attack, providing insights for the design of more durable rare-earth zirconate-based TBCs.

5.2 Introduction

Thermal barrier coatings (TBCs) are commonly employed in the high-temperature regions of gas turbine engines, including the combustion chamber and blades, with the primary objective of prolonging the operational life of metallic components and safeguarding them against degradation caused by elevated temperatures **[1–5]**. TBCs are composed of a fundamental building block that consists of a metallic substrate, typically made of a nickel-based superalloy. A metallic bond coating known as MCrAlY (with M being nickel, cobalt, or both) is then overlaid on this substrate. The bond coat is intended to serve as a buffer layer, effectively reducing the thermal expansion gradient between the substrate and the ceramic topcoat. One of the consequential outcomes of subjecting the coating to high temperatures at the bond coat/topcoat interface is the development of a thermally grown oxide (TGO), which occurs as a reaction product **[6–10]**.

The degradation mechanisms that occur depend on the duration of operation of the TBC coating under the actual operational environment, which involves different degradation mechanisms. These mechanisms encompass (1) the formation and growth of a thermally grown oxide layer

at the interface of the bond coat and topcoat; (2) the sintering of porous ceramic microstructures due to high temperatures; (3) thermal stresses resulting from inadequate thermal expansion coefficients (CTEs) between the ceramic insulation layer and metallic substrate; (4) phase transformations within the ceramic topcoat; and (5) the impact of aggressive environmental factors such as molten salts (hot corrosion), sands, or volcanic ashes (CMAS—CaO-MgO-Al_2O_3-SiO_2). These aspects all lead to the overall deterioration and eventually affect the durability of the TBC coating **[11–14]**. These interdependent mechanisms modify the TBC structure, affecting its mechanical, thermal, and functional properties, and consequently, the overall durability of the system. Most often, the final result of the degradation processes is the loss of TBC covering qualities due to the ceramic layer breaking and spalling (delamination) **[15–17]**.

The phenomenon of hot corrosion is one of the most thoroughly investigated among a vast list of issues examined in this field. Hot corrosion primarily occurs due to the combination of molten alkali sulphates and the topcoat material, resulting in the formation of new phases that cause instability in the topcoat. This instability manifests as cracks and spalling formation, compromising the integrity of the coating. One of the most essential features of hot corrosion in thermal barrier coatings is the presence of fuel impurities, which include sodium, calcium, sulphur, vanadium, and, in some cases, phosphorus. Such fuel impurities may be in the fuel or added by environmental contaminants during the combustion process. The fuel impurities undergo chemical reactions, which ultimately result in the production of corrosive oxides. These oxides may be highly acidic or alkaline, and this makes the environment even more caustic.

$$2V + 5/2\ O_2 \rightarrow V_2O_5 \text{ (strongly acidic)} \quad (1)$$

$$S + O_2 \rightarrow SO_2;\ SO_2 + ½\ O_2 \rightarrow SO_3 \text{ (strongly acidic)} \quad (2)$$

$$2Na + ½\ O_2 \rightarrow Na_2O \text{ (strongly basic)} \quad (3)$$

$$Na_2O \text{ (base)} + SO_3 \text{ (acid)} \rightarrow Na_2SO_4 \text{ (salt)} \quad (4)$$

$$Na_2O \text{ (base)} + V_2O_5 \text{ (acid)} \rightarrow 2NaVO_3 \text{ (salt)} \quad (5)$$

Vanadium pentoxide (V_2O_5), a potent acidic oxide with a melting point of 690 °C, and sodium metavanadate ($NaVO_3$), a corrosive salt with a melting point of 610 °C, have been viewed as severe hazards to TBCs because they can form when both Na and V are present in fuel **[18–23]**.

Identifying two hot corrosion regimes is based on a comprehensive analysis of various factors, including the temperature range, sulphur's role, and the unique morphology of the corrosion attack. These regimes are known as Type II and Type I, and they provide significant information on the individual degradation modes under varying temperature conditions. Type II regime typically occurs at lower temperatures, between 600 °C and 800 °C, which is the normal temperature range. The mechanism and characteristics of corrosion at this temperature regime are not comparable to those observed in the high-temperature regime. Conversely, the type II type I regime prevails at higher temperatures, typically ranging from approximately 800 °C to 950 °C. The corrosion behaviour in this regime is notably distinct from the type II regime and showcases its unique features and mechanisms **[24,25]**. The initial stage of the attack involves dissolving the metal's protective oxide using the available molten sulfate deposit. Type I hot corrosion is initiated by liquid sodium sulphate (Na_2SO_4, which melts at 884 °C **[10,26,27]**.

Sodium (Na) and magnesium (Mg) sulphate mixtures are more susceptible to hot corrosion. This is because they are the only elements that are partially molten at temperatures of approximately 695–698°C, acquiring a partially molten state. In contrast, sodium sulfate alone does not reach a molten state at 700 °C. The fact that there is a mixture of magnesium sulfate ($MgSO_4$) and sodium sulfate (Na_2SO_4) further enhances the incidence of hot corrosion in that the particular mixture of sulfate is a eutectic mixture of sulfate that melts at 666 °C, as opposed to the given temperature of 700 °C. The root cause of hot corrosion sensitivity is the ability of these sulfate salts to foster the development of a highly reactive environment. These sulfate salts react chemically when placed under a high-temperature environment to produce aggressive sulfate species. These aggressive species are especially harmful because they actively attack and corrode the substrate material, causing an increased rate of corrosion **[28–30]**. Hot corrosion in gas turbine engines is also influenced by vanadium impurities that oxidise to V_2O_5 during combustion and react with sodium salts to form $NaVO_3$, further intensifying corrosive damage to coatings **[18–23]**.

The primary objective of this research is to investigate and gain a comprehensive understanding of the complex hot corrosion mechanisms affecting NZO coatings in the presence of sodium sulfate (Na_2SO_4), equimolar sodium–magnesium sulfate mixtures (Na_2SO_4 + $MgSO_4$), and sodium sulfate–vanadium oxide mixtures (Na_2SO_4+V_2O_5). Although the scientific literature extensively covers hot corrosion in TBCs, particularly focusing on sodium sulfate and vanadium-based degradation, there is limited information regarding the specific mechanisms associated with NZO coatings. This knowledge gap suggests the necessity to conduct additional studies of how NZO degrades in these salt environments. The current paper presents the earlier

steps of the degradation process of NZO coatings under the deposits of pure Na_2SO_4, eutectic $Na_2SO_4 + MgSO_4$, and $Na_2SO_4 + V_2O_5$, shedding light on their behaviour in terms of corrosion in various sulfate and vanadate conditions.

5.3. Results and discussion

5.3.1 Hot corrosion test

Single-layered $Nd_2Zr_2O_7$ thermal barrier coating (TBC) samples were subjected to hot corrosion tests to assess their resistance to various aggressive molten salt environments. The salted conditions were studied using pure Na_2SO_4, a mixture of Na_2SO_4 and $MgSO_4$ with an equimolar ratio, and a mixture of Na_2SO_4 and V_2O_5 with an equimolar ratio. A precisely weighed 0.3 mg salt tablet was pre-weighed and placed at the centre of the coating surface to minimise edge effects, and then exposed to a laboratory furnace at 920 °C. The heating rate of the furnace was kept at 10 °C until the salts melted. After 1, 4, and 10 h, the experiments were interrupted and then repeated in 24-h cycles. The pure Na_2SO_4 and $Na_2SO_4 + MgSO_4$ mixtures were exposed for 120 hours, while the highly aggressive environment ($Na_2SO_4 + V_2O_5$) was limited to 36 hours. The samples were allowed to cool in the furnace after each stage to prevent thermal shock. The characterization of the post-exposure was performed using scanning electron microscopy (SEM, Hitachi 3400N) and energy-dispersive spectroscopy (EDS) to study the surface morphology and elemental composition. Phase analysis of the as-sprayed and corroded coatings was performed using X-ray diffraction (XRD, Phillips X'Pert3 with Cu Kα, $\lambda = 1.54178$ Å) in the 2θ range of 10°–90°, enabling the identification of phase transformations and corrosion products formed during the tests.

5.3.2 Microstructural Characteristics of As-Sprayed TBCs

Fig. 5.1 shows the XRD pattern and SEM micrographs of the as-sprayed single-layered NZO thermal barrier coatings. The XRD analysis confirms the presence of a pure pyrochlore NZO phase (PDF No. 78-1618), with sharp and well-defined diffraction peaks, indicating phase stability during plasma spraying without the formation of secondary zirconia or neodymium oxide phases. Similar phase retention has been reported in earlier works on rare-earth zirconate coatings, demonstrating their structural stability under high-energy spraying conditions. The SEM surface morphology, **Fig. 5.1a**, reveals a typical lamellar microstructure with partially melted splats and some unmelted particles, a feature inherent to the atmospheric plasma spraying process. **Fig. 5.1b** provides a clearer view of the inter-splat pores, microcracks, and irregular edges, which contribute to increasing the strain tolerance of the coating, while also

presenting potential routes for molten salt penetration in the event of hot corrosion exposure. These microstructural characteristics, in association with the established pyrochlore phase, are consistent with those reported previously and provide a basis for evaluating the hot corrosion resistance of NZO TBCs.

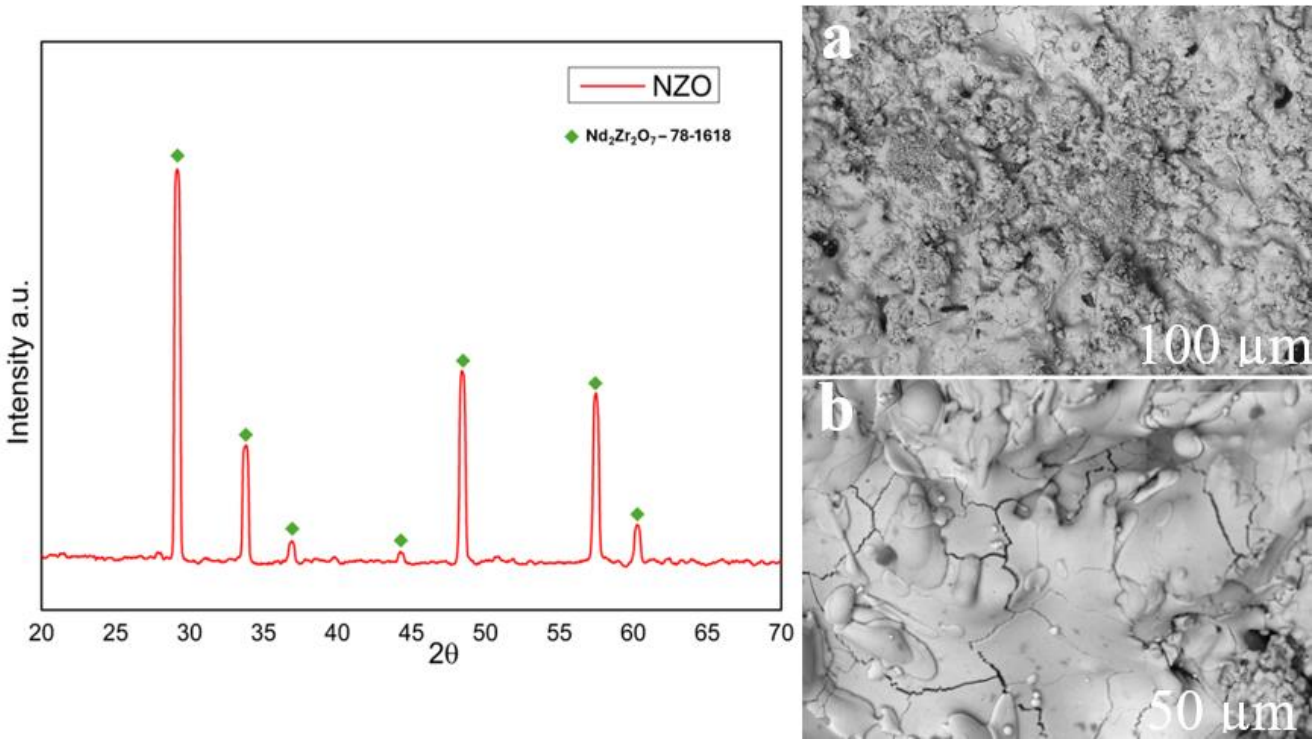

Figure 5.1: Phase Analysis and Surface Morphology of As-Sprayed $Nd_2Zr_2O_7$ TBCs

5.3.3 Hot Corrosion Behavior of $Nd_2Zr_2O_7$ TBCs in Pure Na_2SO_4 Environment

Figure 5.2 presents the XRD pattern of single-layered NZO thermal barrier coatings after hot corrosion exposure in pure Na_2SO_4 for 120 h at 920 °C. The dominant peaks of pyrochlore NZO (PDF No. 78-1618) remain visible, confirming partial structural stability; however, additional reflections corresponding to monoclinic zirconia (m-ZrO_2, PDF No. 37-1484) and sodium peroxide (Na_2O_2, PDF No. 16-0270) indicate ongoing degradation. The decomposition of Na_2SO_4 at high temperature can be represented as:

$$Na_2SO_4 \rightarrow Na_2O\ (\text{Basic}) + SO_3\ (\text{Acidic}) \qquad (6)$$

The liberated Na_2O reacts with oxygen to form sodium peroxide:

$$Na_2O + \frac{1}{2} O_2 \rightarrow Na_2O_2 \quad (7)$$

Meanwhile, the acidic SO_3 interacts with Nd2Zr2O7 destabilizing the pyrochlore lattice and promoting zirconia formation:

$$Nd_2Zr_2O_7 + SO_3 \rightarrow Nd_2(SO_4)_3 + m - ZrO_2 \quad (8)$$

This explains the emergence of m-ZrO_2 peaks in the XRD pattern **[24,25]**. Regardless of such reactions, the fact that even the NZO reflections remain strong after 120 hours of coating testing proves that the coating still retains some resistance. These results highlight that NZO exhibits better resistance than YSZ under sulfate attack, but Na_2SO_4 still initiates early degradation pathways through the combined action of basic (Na_2O/Na_2O_2) and acidic (SO_3) corrosion products.

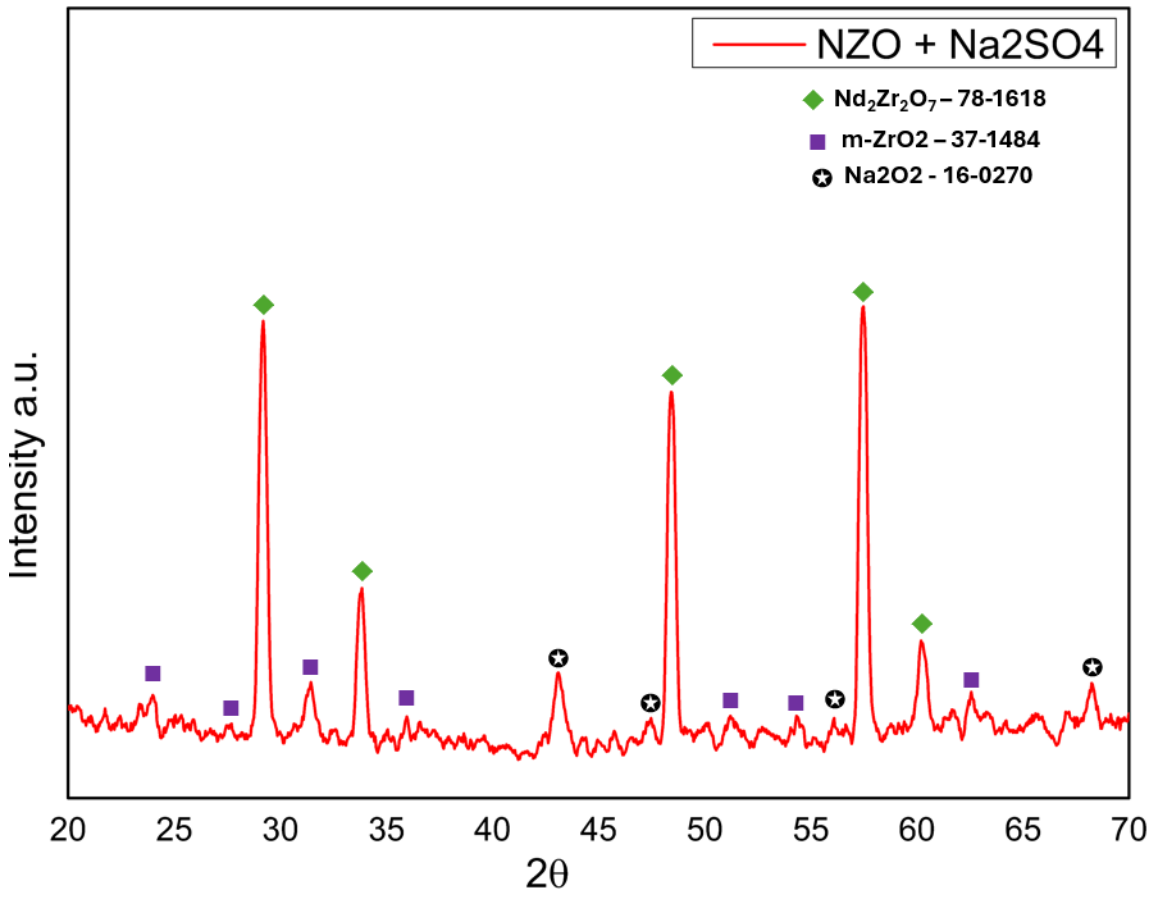

Figure 5.2: XRD Pattern of $Nd_2Zr_2O_7$ TBCs after 120 h Exposure in Pure Na_2SO_4 Environment

Figure 5.3(a-c) presents the micrographs and analysis of EDS and single-layered NZO coating in the presence of molten Na_2SO_4 at different temperatures of 920 °C after 120 h of exposure. Low magnification **5.3 (a, b)** surface morphology shows that there is severe degradation with

a porous and cracking structure with granular and globular corrosion deposits that occupy significant parts of the coating. Increasing magnification to **5.3 (c)**, we can clearly see interconnected cracks as well as localised clusters of reaction products, which support the fact that molten Na_2SO_4 moved along splat boundaries and porosity, providing easy channels through which the salt could move.

The EDS point analysis offers additional information about the corrosion processes. Although points 1-4 generally indicate the presence of Nd-Zr-O-rich areas, such as those found in the pyrochlore matrix, point 5 has a high concentration of sodium (9.1%) and sulphur (6.8%), and a significantly reduced concentration of Zr (3.2%) and Nd (14.4%). This shows the addition of Na and S into the coating, and secondary sodium sulphur phases were formed, partially destabilising the pyrochlore lattice. The elemental mapping results confirm these observations. Oxygen is evenly spread over the microstructure, and Zr and Nd are accumulated in the undamaged parts of the coating. Conversely, Na and S signals are common and more likely to be found in cracks on surfaces and in porous areas, which confirms that salt penetration occurred throughout the microstructure. This distribution indicates that corrosion through the infiltration of Na_2SO_4 into the porous lamellar network promotes localised phase decomposition and the formation of secondary products. Overall, these findings suggest that long-term exposure to molten Na_2SO_4 causes severe microstructural damage and chemical alteration of the NZO coating, which compromises its integrity. However, a small portion of the pyrochlore phase remains intact.

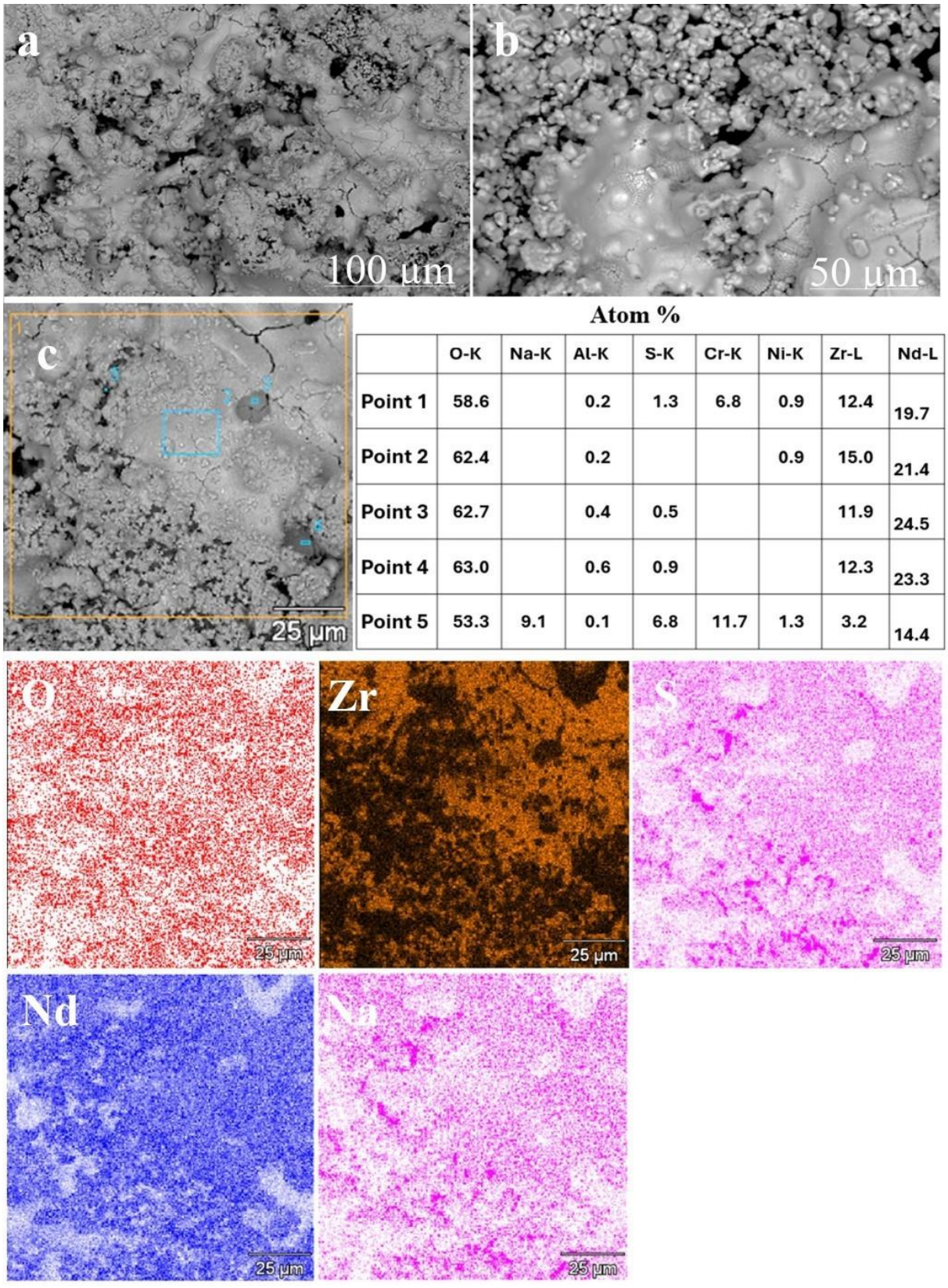

Atom %

	O-K	Na-K	Al-K	S-K	Cr-K	Ni-K	Zr-L	Nd-L
Point 1	58.6		0.2	1.3	6.8	0.9	12.4	19.7
Point 2	62.4		0.2			0.9	15.0	21.4
Point 3	62.7		0.4	0.5			11.9	24.5
Point 4	63.0		0.6	0.9			12.3	23.3
Point 5	53.3	9.1	0.1	6.8	11.7	1.3	3.2	14.4

Figure 5.3: SEM and EDS Analysis of NZO Coatings after 120 h Hot Corrosion in Na_2SO_4

4.3.4 Hot Corrosion Behavior of $Nd_2Zr_2O_7$ in Equimolar Na_2SO_4–$MgSO_4$ Environment

A subsequent hot corrosion test was conducted using a 50/50 molar mixture of sulfate (Na_2SO_4 + $MgSO_4$) at 920 °C. The total exposure time was 120 h, after which X-ray diffraction analysis was performed to examine the phase changes in the TBC sample's topcoat. **Fig 5.4** presents the XRD results of the phase transformation of the NZO (neodymium zirconate) sample. The results indicate that the NZO-based sample, which initially exhibited complete stability in its cubic pyrochlore form before hot corrosion exposure, underwent significant phase transformations. The secondary phases detected include m-ZrO_2 (ICDD card no. 37-1484), $Nd_2(SO_4)_3$ (ICDD card no. 36-0721), NaO_2 (ICDD card no. 77-0209), and MgO (ICDD card no. 87-0653). These findings highlight the susceptibility of NZO-based TBCs to phase transformations when exposed to prolonged hot corrosion in mixed Na_2SO_4 and $MgSO_4$ deposits.

At the specified temperature, the Na_2SO_4 + $MgSO_4$ sulfate mixture exhibits pronounced reactivity toward the coatings. XRD analysis of the NZO topcoat confirmed that the observed phases originate from specific chemical reactions triggered by this aggressive sulfate environment. The transformations leading to phase formation in the NZO topcoat can be described as follows:

$$2Nd_2Zr_2O_2 + 6Na_2SO_4 \rightarrow Nd_2(SO_4)_3 + NaO_2 + 4m - ZrO_2 + SO_3 + Na_2O \quad (9)$$

$$Nd_2Zr_2O_2 + MgSO_4 \rightarrow Nd_2(SO_4)_3 + MgO + m - ZrO_2 \quad (10)$$

These reactions demonstrate the chemical processes occurring in the TBC system upon exposure to the Na_2SO_4+ $MgSO_4$ mixture, leading to the observed phase evolution in the NZO topcoat **[26]**.

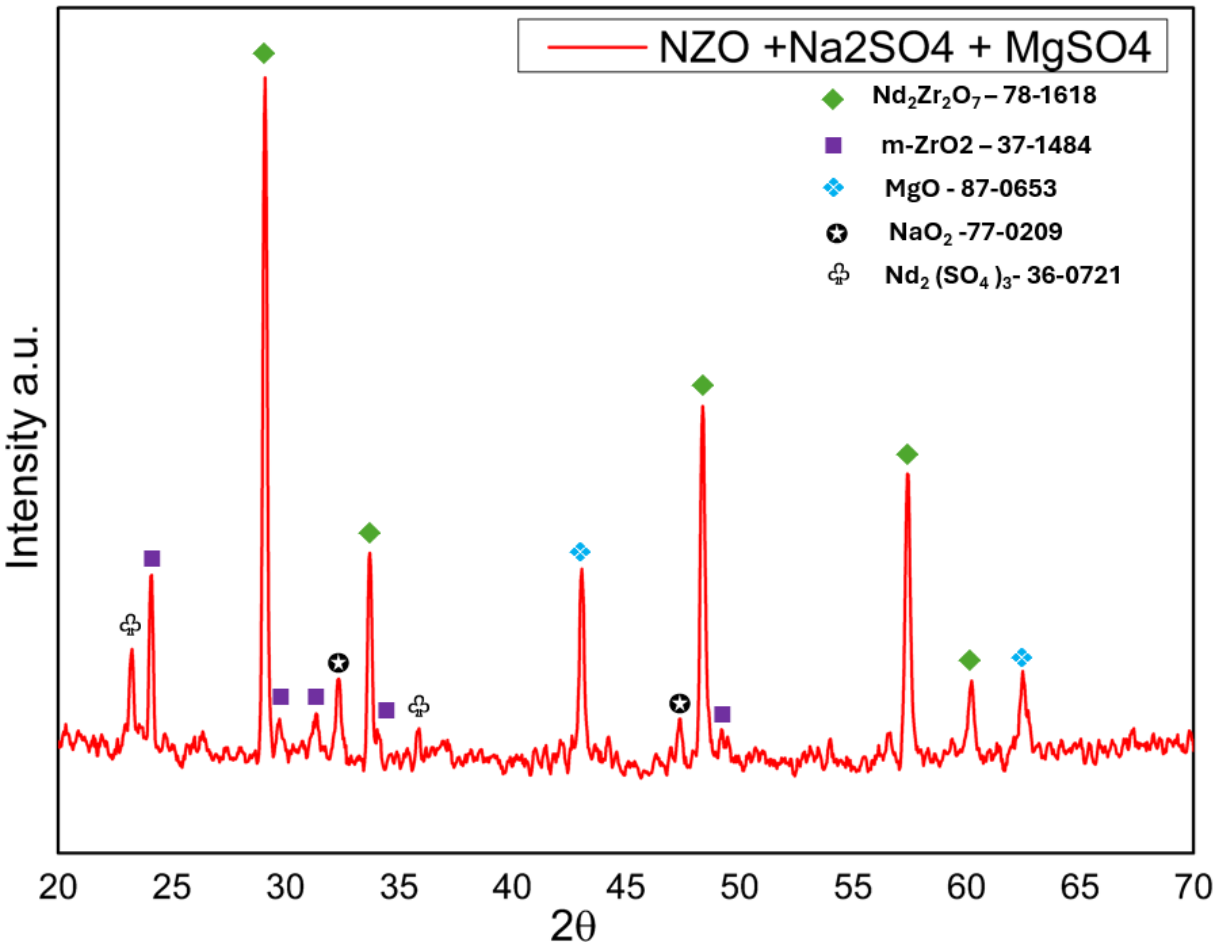

Figure 5.4: XRD Pattern of $Nd_2Zr_2O_7$ TBCs after 120 h Exposure in Na_2SO_4-$MgSO_4$ Environment.

Fig 5.5 shows the SEM micrographs, EDS spectra, and elemental mapping of the NZO topcoat after hot corrosion in an equimolar Na_2SO_4 + $MgSO_4$ mixture at 920 °C for 120 h. The SEM images reveal severe microstructural degradation, including intergranular cracks, pore formation, and grain boundary attack. The surface morphology is also well-preserved, and the bright secondary deposits present serve as evidence of the precipitation of corrosion products. These characteristics indicate that molten salts entered through the already existing cracks and pores, accelerating the localised attack and destabilisation of the NZO phase.

The EDS analysis reveals that Na, Mg, and S are present, in addition to the significant elements of the coating (Nd, Zr, O). Na and S-rich regions are associated with sodium sulphate remains, whereas the Mg-rich areas are related to the creation of MgO. The reduced Nd and Zr content at certain spots highlight selective leaching and decomposition of the pyrochlore structure.

Elemental mapping further supports these observations. Oxygen is relatively homogeneous, whereas Na, Mg, and S are distributed over the corroded regions, confirming salt infiltration

and reaction. Nd and Zr maps show non-uniform distribution, reflecting phase decomposition and the formation of secondary compounds.

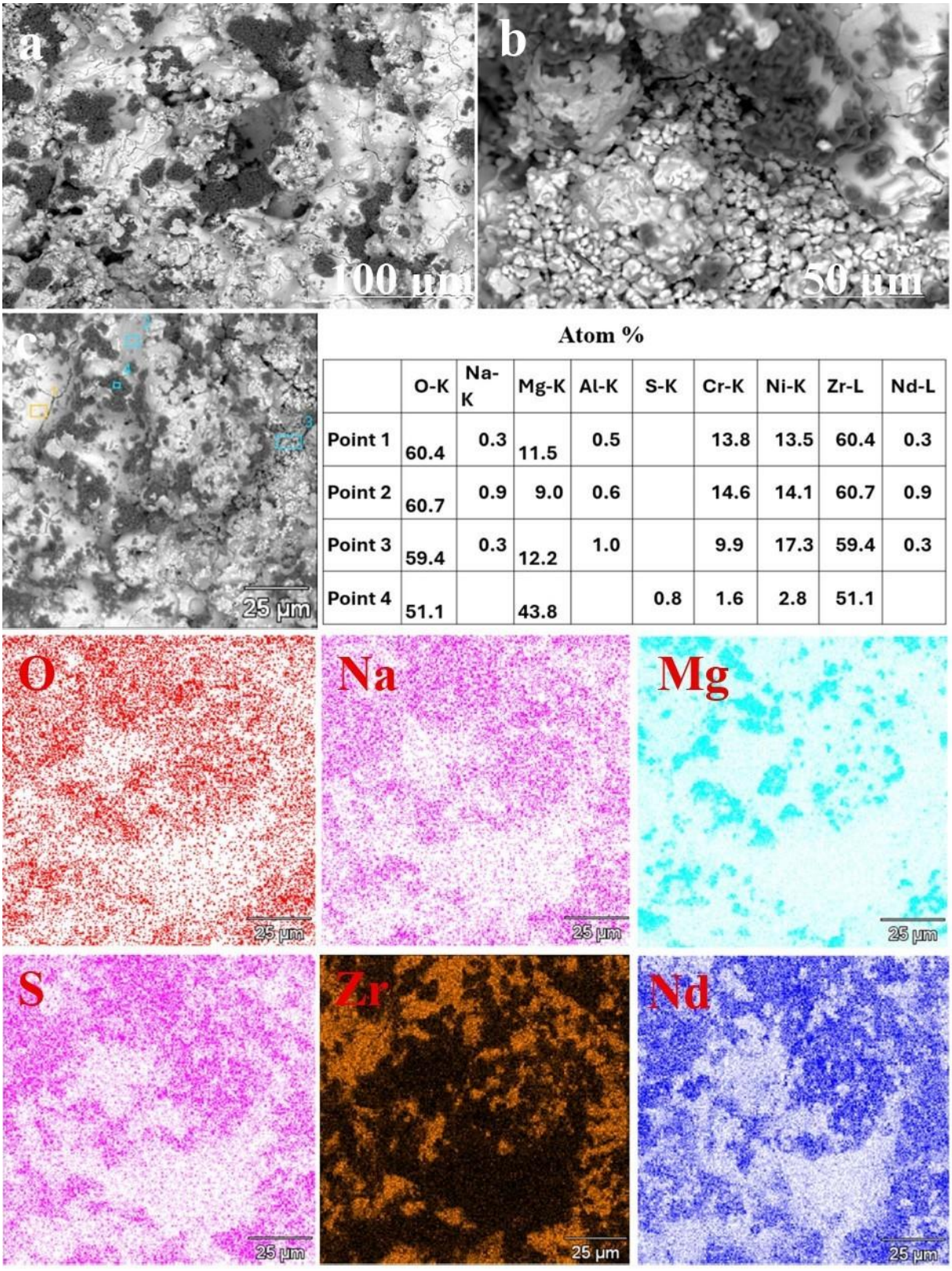

	O-K	Na-K	Mg-K	Al-K	S-K	Cr-K	Ni-K	Zr-L	Nd-L
Point 1	60.4	0.3	11.5	0.5		13.8	13.5	60.4	0.3
Point 2	60.7	0.9	9.0	0.6		14.6	14.1	60.7	0.9
Point 3	59.4	0.3	12.2	1.0		9.9	17.3	59.4	0.3
Point 4	51.1		43.8		0.8	1.6	2.8	51.1	

Figure 5.5: SEM and EDS Analysis of NZO Coatings after 120 h Hot Corrosion in Na_2SO_4-$MgSO_4$ Environment.

These measurements are relatively consistent in terms of the eutectic temperature of L ↔ $Mg_3Na_2(SO_4)_4$ + Na_2SO_4, which is approximately 660 °C. In **[27]**, this temperature was calculated as 666 °C. The ability to form such a low-melting eutectic compound is the primary cause of the greater corrosion effect observed in rare-earth zirconates. Reactions (9) and (10), which explain the formation of sulphates and oxysulphates of the rare-earth elements, in combination with monoclinic zirconia and magnesium and sodium oxides, explain the accelerated degradation. In addition, the occurrence of the rare-earth oxides may be explained by the thermal breaking up of the zirconates, which is considerably enhanced by the appearance of the eutectic sulphate mixture **[27,28]**.

4.3.5 Hot Corrosion Behavior of $Nd_2Zr_2O_7$ in Equimolar Na_2SO_4–V_2O_5 Environment

Fig 5.6 illustrates the XRD pattern of the NZO single-layer thermal barrier coating (TBC) after hot corrosion in an equimolar Na_2SO_4+V_2O_5 environment at 920 °C for 36 h. The spectrum reveals the partial disappearance of the characteristic pyrochlore peaks and the concurrent emergence of strong reflections from $NdVO_4$ and monoclinic ZrO_2, confirming the extensive chemical decomposition of the coating. The corrosion mechanism is initiated by the eutectic reaction between Na_2SO_4 and V_2O_5, which produces low-melting sodium vanadates that readily infiltrate pores and splat boundaries of the coating:

$$Na_2SO_2 + V_2O_5 \rightarrow Na_2VO_3 + SO_3 \qquad (11)$$

Once infiltrated, vanadates preferentially react with the A-site rare-earth cations of the pyrochlore, destabilising the lattice and leading to the formation of rare-earth vanadates with simultaneous release of zirconia:

$$Nd_2Zr_2O_7 + 2V_2O_5 \rightarrow 2NdVO_4 + 2ZrO_2 \qquad (12)$$

On cooling, the zirconia produced stabilises predominantly in the monoclinic polymorph, which is associated with a volume change and the generation of local stresses:

$$t - ZrO_2 \rightarrow m - ZrO_2 + \Delta V \qquad (13)$$

The sharp NdVO4 peaks observed in the diffractogram indicate not only the high chemical affinity of Nd^{3+} for vanadates but also suggest crystallisation of needle- or plate-like vanadate phases that can embrittle the coating microstructure. In the meantime, monoclinic zirconia is an indication of the stresses caused by the transformation, which also damages coating integrity and increases crack propagation. The overall decomposition pathway of NZO under these conditions is analogous to that reported for other rare-earth zirconates such as $Gd_2Zr_2O_7$ and

$La_2Zr_2O_7$, which also undergo $REVO_4 + ZrO_2$ formation in $Na_2SO_4 + V_2O_5$ environments. These results indicate that, despite having better thermal stability during pure thermal cycling, NZO is susceptible to vanadate corrosion; hence, its usage in impure, contaminated combustion atmospheres is limited. Employing multilayer architectures or infiltration-resistant topcoats can reduce the corrosive effects of such environments **[29-31]**.

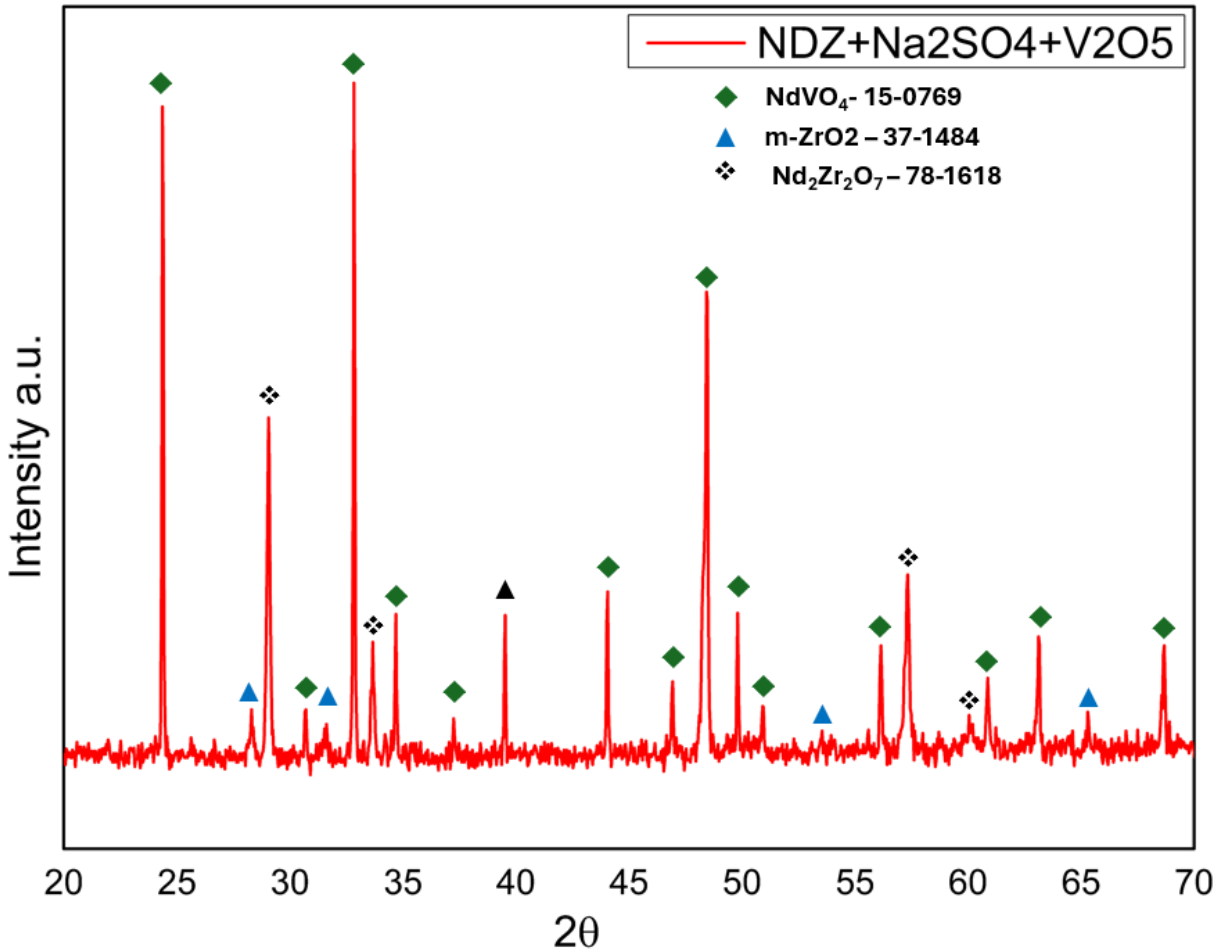

Figure 5.6: XRD Pattern of $Nd_2Zr_2O_7$ TBCs after 36 h Exposure in Na_2SO_4-V_2O_5 Environment.

Fig 5.7 provides direct microstructural evidence for the phase decomposition of NZO after hot corrosion in an equimolar Na_2SO_4+V_2O_5 mixture at 920 °C for 36 h. The surface morphology in Fig. 4.7a reveals faceted crystallites that are enriched in neodymium and vanadium. These are typical of $NdVO_4$, which is one of the major corrosion products when molten vanadates penetrate the coating and react selectively with the rare-earth cation. Similar faceted or needle-like vanadate precipitates have been extensively reported in $Gd_2Zr_2O_7$, $La_2Zr_2O_7$, and YSZ systems exposed to Na_2SO_4 + V_2O_5, and their growth has been linked to the strong thermodynamic affinity of rare-earth ions for vanadate species. These brittle crystallites tend to

nucleate at the surface and within splat boundaries, where the vanadate melt accumulates, thereby serving as crack initiation sites that weaken the mechanical integrity of the coating. In contrast, **Fig. 5.7b** shows agglomerated and irregular grains dominated by zirconium, which correspond to monoclinic ZrO_2. The appearance of zirconia is a direct consequence of neodymium extraction from the parent pyrochlore lattice, leaving a Zr-rich matrix that separates and crystallises independently. During cooling, this zirconia stabilises mainly in the monoclinic polymorph, whose tetragonal-to-monoclinic transformation is associated with a volume expansion of about 4–5%. This transformation strain generates local stresses and microcracks, compounding the embrittlement introduced by $NdVO_4$ crystallites. The coexistence of $NdVO_4$ and m-ZrO_2, both observed here, has also been reported in previous studies of $Gd_2Zr_2O_7$ and $La_2Zr_2O_7$ coatings under identical salt environments, confirming that this dual-phase decomposition is a universal corrosion pathway for rare-earth zirconates **[32-33]**.

The compositional evidence in **Fig. 5.7c** further validates this interpretation. Faceted crystallites report energy dispersive spectroscopy with about 15 atomic percent of vanadium and 16-17 atomic percent of neodymium, which is in line with stoichiometric $NdVO_4$. In comparison, the neighbouring grains of the oxide are concentrated on zirconium and oxygen, similar to the composition of zirconia. These results show that $NdVO_4$ and ZrO_2 phases are spatially isolated. On the elemental mapping not represented in this section of the figure, it can be seen that the trace levels of sodium and sulphur are diffusely apportioned throughout the corroded scale. This behaviour agrees with the literature, where Na_2SO_4 is described as a fluxing agent that reacts with V_2O_5 to form sodium metavanadate ($NaVO_3$), which facilitates penetration of the molten phase, while sulphur volatilizes as SO_3. Consequently, Na and S rarely appear as stable crystalline residues in XRD or EDS analyses, which explains their weak signals in the present study.

Overall, the features in **Fig. 5.7(a–c)** confirm the proposed corrosion mechanism: molten $NaVO_3$ formed in situ penetrates the coating microstructure, extracts $Nd3^+$ from the pyrochlore lattice to form $NdVO_4$, and leaves behind a destabilised Zr-rich framework that crystallises as monoclinic zirconia. The brittle morphology of $NdVO_4$ crystallites, combined with the stress-inducing polymorphic transformation of zirconia, provides a synergistic pathway for coating degradation, ultimately reducing adhesion and accelerating failure during service.

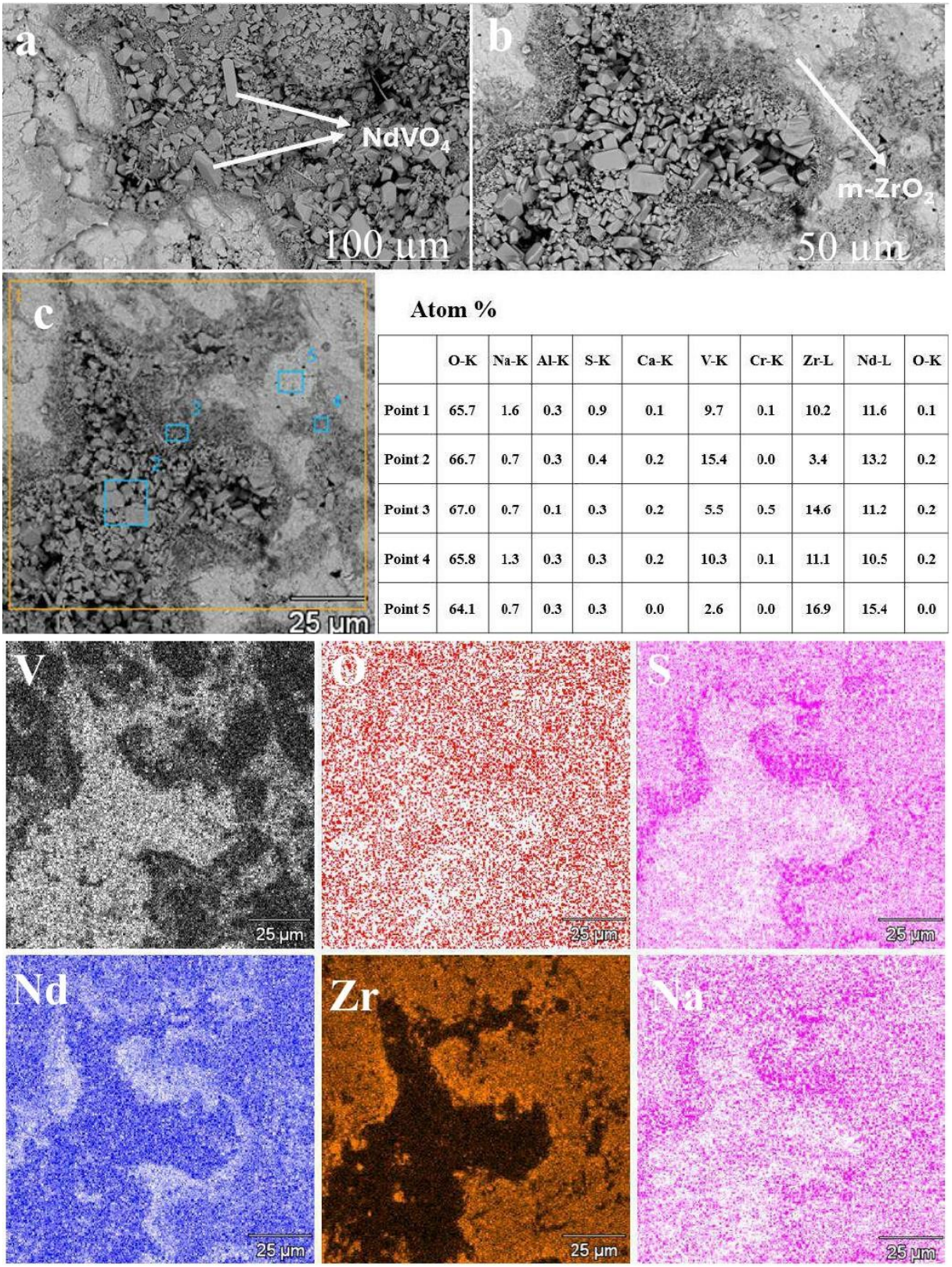

Atom %

	O-K	Na-K	Al-K	S-K	Ca-K	V-K	Cr-K	Zr-L	Nd-L	O-K
Point 1	65.7	1.6	0.3	0.9	0.1	9.7	0.1	10.2	11.6	0.1
Point 2	66.7	0.7	0.3	0.4	0.2	15.4	0.0	3.4	13.2	0.2
Point 3	67.0	0.7	0.1	0.3	0.2	5.5	0.5	14.6	11.2	0.2
Point 4	65.8	1.3	0.3	0.3	0.2	10.3	0.1	11.1	10.5	0.2
Point 5	64.1	0.7	0.3	0.3	0.0	2.6	0.0	16.9	15.4	0.0

Figure 5.7: SEM and EDS Analysis of NZO Coatings after 36 h Hot Corrosion in Na_2SO_4-V_2O_5 Environment.

5.4 Conclusion

- Plasma-sprayed NZO coatings exhibited distinct hot corrosion behaviours depending on the molten salt environment.
- In Na_2SO_4, NZO maintained partial phase stability, though monoclinic ZrO_2 and sodium oxides indicated the onset of degradation.
- In Na_2SO_4–$MgSO_4$, eutectic formation at ~660 °C accelerated microstructural damage, causing grain boundary attack, microcracking, and the formation of $Nd_2(SO_4)_3$ and MgO.
- In Na_2SO_4–V_2O_5, rapid pyrochlore decomposition produced $NdVO_4$ and monoclinic zirconia, leading to severe cracking and early coating failure.
- The results confirm that NZO offers moderate resistance against sulfate-based salts but is highly vulnerable to vanadate-induced attack.
- To enhance durability, future strategies should focus on multilayered architectures or compositionally engineered designs that mitigate vanadate reactivity while retaining the high-temperature stability of NZO.

References

[1] K. M. Doleker, Y. Ozgurluk, Y. Kahraman, and A. C. Karaoglanli, "Oxidation and hot corrosion resistance of HVOF/EB-PVD thermal barrier coating system," *Surf. Coatings Technol.*, vol. 409, no. December 2020, p. 126862, 2021, doi: 10.1016/j.surfcoat.2021.126862.

[2] A. Iqbal, G. Moskal, H.M. Głowacka, T. Pawlik, and A. Cavalerio, Phase decompositions of Gd2Zr2O7+ 8YSZ TBC systems under the condition of long-term high-temperature oxidation. Surface and Coatings Technology, 462, p.129471, 2023, doi: 10.1016/j.surfcoat.2023.129471

[3] K. W. Schlichting, N. P. Padture, E. H. Jordan, and M. Gell, "Failure modes in plasma-sprayed thermal barrier coatings," *Mater. Sci. Eng. A*, vol. 342, no. 1–2, pp. 120–130, 2003, doi: 10.1016/S0921-5093(02)00251-4.

[4] J. W. Hutchinson *et al.*, "Thermal barrier coating materials for SI engine," *Ceram. Int.*, vol. 50, no. 1, pp. 179–184, 2002, doi: 10.1016/S1359-6454(01)00422-0.

[5] A. Mehta *et al.*, "Processing and Advancements in the Development of Thermal Barrier Coatings: A Review," *Coatings*, vol. 12, no. 9, 2022, doi: 10.3390/coatings12091318.

[6] J. G. Thakare, C. Pandey, M. M. Mahapatra, and R. S. Mulik, "Thermal Barrier Coatings—A State of the Art Review," *Met. Mater. Int.*, vol. 27, no. 7, pp. 1947–1968, 2021, doi: 10.1007/s12540-020-00705-w.

[7] G. Moskal, "Thermal barrier coatings: Part 1 – characteristics of microstructure and properties, generation and directions of development of bond," *Arch. Mater. Sci.*, vol. 28, no. 2, pp. 100–112, 2007.

[8] A. M. Karlsson, T. Xu, and A. G. Evans, "The effect of the thermal barrier coating on the displacement instability in thermal barrier systems," *Acta Mater.*, vol. 50, no. 5, pp. 1211–1218, 2002, doi: 10.1016/S1359-6454(01)00422-0.

[9] S. Dhomne and A. M. Mahalle, "Thermal barrier coating materials for SI engine," *J. Mater. Res. Technol.*, vol. 8, no. 1, pp. 1532–1537, 2019, doi: 10.1016/j.jmrt.2018.08.002.

[10] L. Guo, B. Li, Y. Cheng, and L. Wang, "Composition optimization , high-temperature stability , and thermal cycling performance of Sc-doped Gd 2 Zr 2 O 7 thermal barrier coatings : Theoretical and experimental studies," vol. 11, no. 3, pp. 454–469, 2022.

[11] G. Moskal, S. Jucha, M. Mikuśkiewicz, D. Migas, and A. Jasik, "Atypical decomposition processes of Sm 2 Zr 2 O 7 + 8YSZ dual-phase TBCs during hot corrosion," *Corros. Sci.*, vol. 170, no. April, p. 108681, 2020, doi: 10.1016/j.corsci.2020.108681.

[12] P. Mohan, T. Patterson, B. Yao, and Y. Sohn, "Degradation of thermal barrier coatings by fuel impurities and CMAS: Thermochemical interactions and mitigation approaches," *J. Therm. Spray Technol.*, vol. 19, no. 1–2, pp. 156–167, 2010, doi: 10.1007/s11666-009-9424-0.

[13] S. Morelli, S. Bursich, V. Testa, G. Bolelli, and A. Miccich, "Surface & Coatings Technology CMAS corrosion and thermal cycling fatigue resistance of alternative thermal barrier coating materials and architectures : A comparative evaluation," vol. 439, no. April, 2022, doi: 10.1016/j.surfcoat.2022.128433.

[14] Z. Y. Wei *et al.*, “Progress in ceramic materials and structure design toward advanced thermal barrier coatings,” *J. Adv. Ceram.*, vol. 11, no. 7, pp. 985–1068, 2022, doi: 10.1007/s40145-022-0581-7.

[15] A. G. Evans, D. R. Mumm, and J. W. Hutchinson, “Mechanisms controlling the durability of thermal barrier coatings,” vol. 46, pp. 505–553, 2001.

[16] Z. Chen *et al.*, “Surface & Coatings Technology A comparative study on the hot corrosion behavior of plasma sprayed Sm / Gd doped La 2 Zr 2 O 7 / YSZ and Sm and Gd co-doped La 2 Zr 2 O 7 / YSZ coatings,” *Surf. Coat. Technol.*, vol. 452, no. May 2022, p. 129077, 2023, doi: 10.1016/j.surfcoat.2022.129077.

[17] M. K. Hossain *et al.*, “A review on recent applications and future prospects of rare earth oxides in corrosion and thermal barrier coatings, catalysts, tribological, and environmental sectors,” *Ceram. Int.*, vol. 48, no. 22, pp. 32588–32612, 2022, doi: 10.1016/j.ceramint.2022.07.220.

[18] R. L. Jones, “Some Aspects of the Hot Corrosion of Thermal Barrier Coatings,” vol. 6, no. March, pp. 77–84, 1997.

[19] R. L. Jones *et al.*, “Oxidation and hot corrosion resistance of HVOF/EB-PVD thermal barrier coating system,” *Surf. Coatings Technol.*, vol. 23, no. December 2020, pp. 1–10, 2016, doi: 10.1016/j.engfailanal.2015.11.057.

[20] Y. Ozgurluk, K. M. Doleker, D. Ozkan, H. Ahlatci, and A. C. Karaoglanli, “Cyclic hot corrosion failure behaviors of EB-PVD TBC systems in the presence of sulfate and vanadate molten salts,” *Coatings*, vol. 9, no. 3, 2019, doi: 10.3390/coatings9030166.

[21] H. fei Liu, X. Xiong, X. bin Li, and Y. lei Wang, “Hot corrosion behavior of Sc2O3-Y2O3-ZrO2 thermal barrier coatings in presence of Na2SO4+V2O5 molten salt,” *Corros. Sci.*, vol. 85, pp. 87–93, 2014, doi: 10.1016/j.corsci.2014.04.001.

[22] H. Jamali, R. Mozafarinia, R. Shoja-Razavi, and R. Ahmadi-Pidani, “Comparison of hot corrosion behaviors of plasma-sprayed nanostructured and conventional YSZ thermal barrier coatings exposure to molten vanadium pentoxide and sodium sulfate,” *J. Eur. Ceram. Soc.*, vol. 34, no. 2, pp. 485–492, 2014, doi: 10.1016/j.jeurceramsoc.2013.08.006.

[23] P. G. Lashmi, S. Majithia, V. Shwetha, N. Balaji, and S. T. Aruna, “Improved hot corrosion resistance of plasma sprayed YSZ/Gd2Zr2O7 thermal barrier coating over single layer YSZ,” *Mater. Charact.*, vol. 147, no. November 2018, pp. 199–206, 2019, doi: 10.1016/j.matchar.2018.11.007.

[24] A. Iqbal, G. Moskal, and B. Witala, “Degradation mechanism of dual-phase thermal barrier coatings Gd2Zr2O7 + 8YSZ under hot corrosion in pure Na2SO4,” *J. Therm. Anal. Calorim.*, vol. 150, no. 1, pp. 151–165, 2025, doi: 10.1007/s10973-024-13784-3.

[25] D. Migas, G. Moskal, and S. Jucha, “Hot corrosion behavior of double-phase Nd2Zr2O7-YSZ thermal barrier coatings,” *Surf. Coatings Technol.*, vol. 449, no. September, p. 128955, 2022, doi: 10.1016/j.surfcoat.2022.128955.

[26] B. R. Marple, J. Voyer, M. Thibodeau, D. R. Nagy, and R. Vassen, “Hot corrosion of lanthanum zirconate and partially stabilized zirconia thermal barrier coatings,” *J. Eng. Gas Turbines Power*, vol. 128, no. 1, pp. 144–152, 2006, doi: 10.1115/1.1924534.

[27] H. Du, “Thermodynamic assessment of the K_2SO_4–Na_2SO_4–$MgSO_4$–$CaSO_4$ system,”

Journal of Phase Equilibria, vol. 21, Feb. 2000, doi: 10.1361/105497100770340363.

[28] S. Hu, H. Finklea, and X. Liu, "A review on molten sulfate salts induced hot corrosion," *J. Mater. Sci. Technol.*, vol. 90, pp. 243–254, 2021, doi: 10.1016/j.jmst.2021.03.013.

[29] J. De la Roche, J. M. Alvarado-Orozco, and A. Toro, "Hot corrosion mechanism of yttria-stabilized zirconia powder in the presence of molten Na2SO4 + V2O5 salts," *Rare Met.*, vol. 40, no. 5, pp. 1307–1316, 2021, doi: 10.1007/s12598-020-01388-3.

[30] H. Vakilifard, R. Ghasemi, and M. Rahimipour, "Hot corrosion behaviour of plasma-sprayed functionally graded thermal barrier coatings in the presence of Na2SO4 + V2O5 molten salt," *Surf. Coatings Technol.*, vol. 326, pp. 238–246, 2017, doi: 10.1016/j.surfcoat.2017.07.058.

[31] M. Tabeshfar, M. Salehi, G. Dini, P. I. Dahl, M. A. Einarsrud, and K. Wiik, "Hot corrosion of Gd2Zr2O7, Gd2Zr2O7/YbSZ, YSZ + Gd2Zr2O7/YbSZ, and YSZ thermal barrier coatings exposed to Na2SO4 + V2O5," *Surf. Coatings Technol.*, vol. 409, no. July 2020, p. 126718, 2021, doi: 10.1016/j.surfcoat.2020.126718.

[32] S. Yugeswaran, A. Kobayashi, and P. V. Ananthapadmanabhan, "Hot corrosion behaviors of gas tunnel type plasma sprayed La 2Zr 2O 7 thermal barrier coatings," *J. Eur. Ceram. Soc.*, vol. 32, no. 4, pp. 823–834, 2012, doi: 10.1016/j.jeurceramsoc.2011.10.049.

[33] T. Malurdy, M. Mocek, A. Jasik, and G. Moskal, "Top-surface characterization of La2Zr2O7 + 8YSZ thermal barrier coatings under condition of hot corrosion in liquid Na2SO4 + V2O5 deposits," *Ochr. Przed Koroz.*, vol. 64, no. 6, pp. 170–176, 2021, doi: 10.15199/40.2021.6.1.

Chapter 6: Complex sulphate vanadate salt induced hot corrosion of $Nd_2Zr_2O_7$ + 8YSZ composite thermal barrier coating system

6.1 Abstract

The resistance to hot corrosion of composite two-phase thermal barrier coating (TBC) systems of the $Nd_2Zr_2O_7$ + 8YSZ type, plasma-sprayed onto the IN625 alloy with a NiCrAlY interlayer, is investigated. The studies of the TBC system in its as-sprayed state revealed the presence of the $Nd_2Zr_2O_7$ pyrochlore phase and the tetragonal ZrO_2 oxide. Minor effects of pyrochlore decomposition into non-stoichiometric fluorite forms were also observed. The analysed system demonstrated high resistance to hot corrosion processes in environments of liquid Na_2SO_4 salt, as well as the Na_2SO_4 + $MgSO_4$ salt mixture. The primary destruction mechanism in this case involved the intensification of the pyrochlore phase decomposition process, which was considerably more pronounced in the mix of sulphate salts. The second observed phenomenon was the formation of a network of pores and cracks, which significantly facilitated the penetration of the corrosive agent into the coating. The introduction of vanadium oxide considerably accelerated the destruction process, which was attributed to the formation of neodymium vanadates.

6.2 Introduction

Thermal barrier coating systems (TBCs) have received significant attention because they are widely used in combustors, hot gas turbines, jet engines, and nuclear power plants, where they are employed to block high operating temperatures and aggressive, corrosive conditions. These coatings serve a protective purpose, providing thermal insulation, thermal shock resistance, high-temperature corrosion resistance, oxidation reduction, and durability during repeated service cycles in the presence of mechanical loads **[1–3].** TBCs are also needed to enhance operating temperatures, minimise substrate temperatures, and protect components against hot gases **[4–6].**

Thermal barrier coating has been developed as a result of alterations in the composition and microstructure of the topcoat (TC) of ceramic, thermally grown oxide (TGO), metallic bond coating (BC), and interfaces, which attempt to increase high-temperature thermal insulation, protective functionality, and longevity. The typical arrangement of a TBC consists of a metallic bond layer (MCrAlY, where M is Ni, Co, or NiCo) and a topcoat of ceramic. The TBCs (thicknesses between 100 and 500 μm) have a strong influence on decreasing the surface temperature of superalloys (by about 100 to 300 °C) **[7-9]**. Zirconia (ZrO2) is the usual choice of the topcoat, and this is mixed with 7-8 wt% yttrium oxide (Y2O3) to maintain the tetragonal

phase. YSZ is commonly used because it has a high melting temperature of 2700 °C, relatively low thermal conductivity and thermal expansion coefficient (CTE) of 11×10^{-6} K^{-1}, which is similar to the thermal material underneath, superalloy **[10-13]**. It has a high fracture toughness to minimise the stresses and avoid the formation of cracks within the topcoat during thermal cycling. Such special properties of YSZ render it appropriate for TBC applications. Nonetheless, YSZ has considerable performance resistance in high temperatures. YSZ decomposes rapidly at temperatures exceeding 1200 °C, undergoing a phase transition and sintering that causes its deterioration. TBC failure is a phenomenon resulting in the three effects of material degradation, which include volume expansion, increased thermal conductivity and strain tolerance weakness of YSZ **[14-16]**. The main disadvantage of YSZ materials is that they have low resistance to molten salt materials, such as Na_2SO_4, V_2O_5, $MgSO_4$, $CaSO_4$, and K_2SO_4. These pollutants are generated during jet engine operation due to fuel impurities, dusty particles, and runway dust. The reaction between YSZ and these salts leads to adverse chemical reactions, resulting in the loss of Y_2O_3 content in the topcoat and destabilisation of the tetragonal zirconia phase. Destabilisation and increased porosity together increase the rate of the degradation process of the coating. The TBCs made with YSZ exhibit performance degradation caused by sintering problems and phase instability, which is exacerbated by molten salt pollution **[17-19]**.

New materials have been discussed in depth, including the operating temperature constraints of conventional 8YSZ materials, and their established drawbacks have also been addressed. Perovskites, hexaaluminates, and rare-earth zirconium oxides ($A_2B_2O_7$, where A is La, Nd, Gd, Sm, or Eu) are attracting the attention of the scientific community due to their high thermal stability and outstanding chemical stability. Rare earth zirconates are unique in having a thermal conductivity reduction, as well as embracing fluorite and pyrochlore crystal systems among their types. For example, $La_2Zr_2O_7$ has a thermal conductivity of 1.5 $Wm^{-1}K^{-1}$, while $Nd_2Zr_2O_7$, $Sm_2Zr_2O_7$, $Gd_2Zr_2O_7$, and $Eu_2Zr_2O_7$ exhibit thermal conductivity values of 1.6, 1.5, 1.6, and 1.6 $Wm^{-1}K^{-1}$, respectively **[20-22]**. The materials also offer excellent thermal expansion, good resistance to hot corrosion, stability at high temperatures, and high chemical resistance. These characteristics make them appropriate for high-temperature applications. In addition, rare earth zirconates are highly resistant to corrosion due to the effects of molten glass deposits, specifically the CMAS that forms **[23,24]**. A vast amount of literature has focused on the thermal and chemical properties of rare-earth zirconates, such as $Nd_2Zr_2O_7$, $Gd_2Zr_2O_7$, $La_2Zr_2O_7$, $Sm_2Zr_2O_7$, and $Eu_2Zr_2O_7$. These alloys have demonstrated exemplary performance in thermal degradation and molten salt resistance **[25,26]**. Although this has been improved, the

scientific literature primarily focuses on the occurrence of high-temperature corrosion in TBCs due to molten salt formation, especially those containing sodium sulphate or vanadium oxides. The extent of the knowledge about the corrosion of TBCs fabricated using rare earth zirconates or cerates in the presence of other sulphate salts, such as potassium sulphate, magnesium sulphate and calcium sulphate, is somewhat limited.

This research aims to bridge this gap by developing and analysing $Nd_2Zr_2O_7$ + 8YSZ composite coatings. These composite coatings combine the beneficial properties of Yttria-Stabilised Zirconia with the enhanced thermal and corrosion resistance demonstrated by rare-earth zirconates. The selection of these materials was based on a series of analyses of two-phase TBC coatings featuring an equimolar mixture of rare-earth zirconates (such as La, Nd, Sm, and Gd). These studies indicated that the stability of these systems relies on the mass and radii of the rare-earth cations. The highest stability was observed in TBC systems based on lanthanum zirconates, whereas the lowest stability was found in systems incorporating samarium and gadolinium zirconates. Therefore, this study evaluates a system containing neodymium zirconate, assuming that its phase stability would be similar to that of lanthanum zirconate **[15,27]**.

The coatings were produced using air plasma spraying, a commonly employed technique for TBC fabrication. Their resistance to hot corrosion was tested in various liquid sulphate environments, including pure Na_2SO_4, a mixture of Na_2SO_4 and V_2O_5, and a mixture of Na_2SO_4 and $MgSO_4$. The magnesium sulphate salt was added to basic sodium sulphate salt to decrease the melting temperature of this type of mixture and increase the corrosion aggressivity of deposits in this way [**28**]. Furthermore, their thermal shock resistance was evaluated to assess durability under cyclic heating and cooling conditions.

6.3 Results and discussion

6.3.1. Characterisation of As-deposited TBC coatings

The phase composition and microstructure of the $Nd_2Zr_2O_7$ + 8YSZ thermal barrier coatings are shown in **Fig. 6.1** and **Fig. 6.2**. XRD analysis of the surfaces of the samples confirmed the retention of the original powder phases, namely, 8YSZ with a dominant tetragonal phase, along with the $Nd_2Zr_2O_7$ cubic phase. There was no evidence of new phases arising from interactions between the initial phases. Nevertheless, a slight broadening of the peaks on the right side of the Nd-zirconate compound may suggest the formation of a small volume of non-stoichiometric compounds (see areas in the circles).

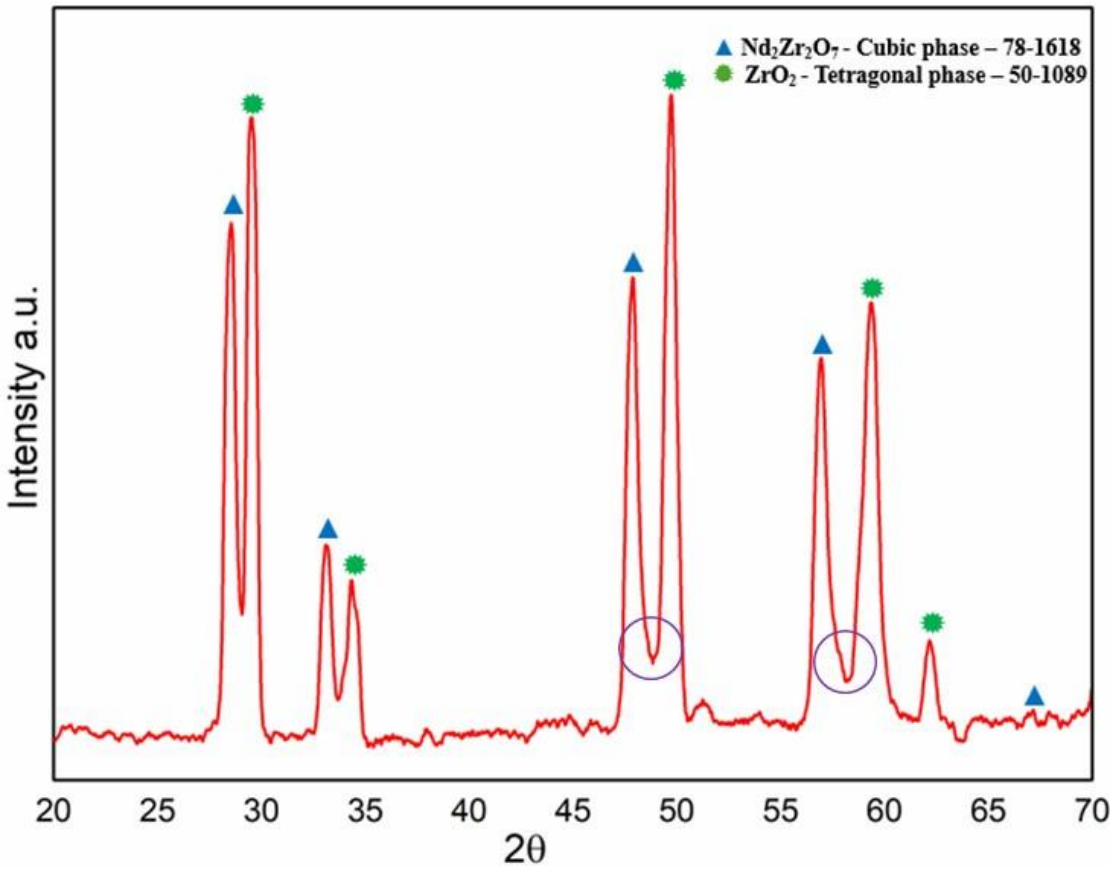

Figure 6.1: XRD pattern of 50 $Nd_2Zr_2O_7$ + 50 8YSZ as a sprayed coating

Visual surface examination of the TBC systems after thermal spraying, **Fig. 6.2(a, b)**, revealed features typical of the process, with no indications of factors that might accelerate degradation under hot corrosion conditions. There were no signs of delamination or atypical microcracks; only microcracks characteristic of the atmospheric plasma spraying methodology were observed. Cross-sectional scanning electron microscopy images of the coatings (**Fig. 6.2c**) further confirmed the strong adhesion between the coating and the Inconel substrate. There was no delamination at the interfaces between the bond coat and the substrate or between the bond coat and the ceramic layer, and no significant cracks were found. Distinct boundaries between the NiCrAlY bond coat and the 8YSZ + $Nd_2Zr_2O_7$ ceramic layer were visible, with bright regions indicating $Nd_2Zr_2O_7$ and darker zones representing 8YSZ.

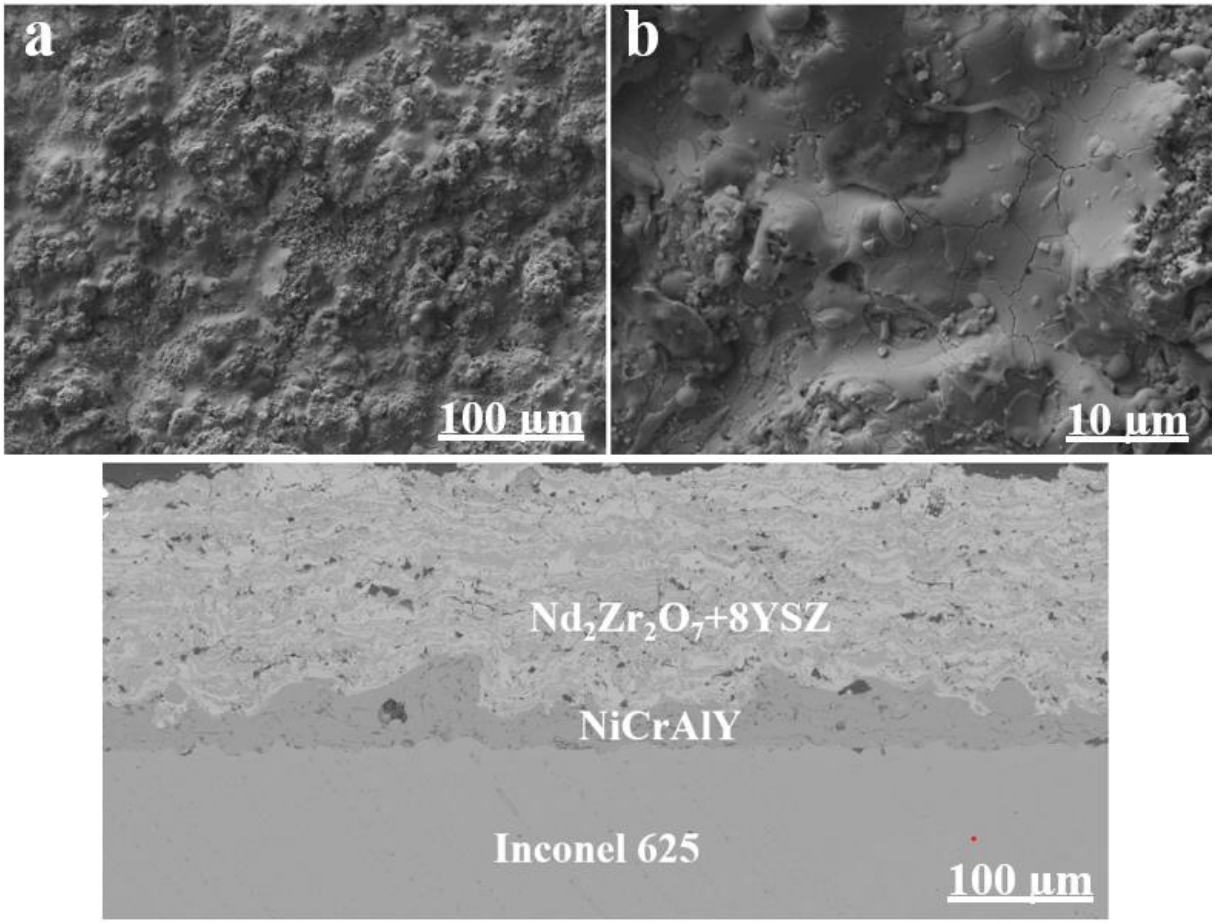

Figure 6.2: Top surface and cross-sectional SEM images of the as-sprayed TBC system.

6.3.2 Hot Corrosion in a Pure Na_2SO_4 Environment

After an extensive duration of 224 hours of exposure to elevated temperatures of 920 °C, a comprehensive analysis of the surfaces was conducted to identify the composition of their phases. Following hot corrosion treatment, the X-ray diffraction pattern of the $Nd_2Zr_2O_7$ + 8YSZ topcoat, as shown in **Fig. 6.3**, resembled the patterns observed in the as-sprayed coatings. However, the peak broadening effect of the zirconate phase was significantly more pronounced. The key phases identified in the upper part of the topcoat were tetragonal zirconia (t-ZrO2) and neodymium zirconate, which had a pyrochlore structure (p-$Nd_2Zr_2O_7$). Also, several peaks that were indicated by red circles on **Fig. 6.3** were observed. These peaks needed to be improved and were shown separately from the entire XRD patterns. They were reported to be non-stoichiometric zirconate phases, specifically $Nd_{0.5}Zr_{0.5}O_{1.75}$ (JCPDS no. 781289) and $Nd_{0.25}Zr_{0.75}O_{1.875}$ (JCPDS no. 280678), characterised by a fluorite structure. The compounds are likely formed as a result of the decomposition of p-$Nd_2Zr_2O_7$ after this product reacts with zirconia. Na_2SO_4 (JCPDS no. 01-10309) was also found. When $Nd_2Zr_2O_7$ was used together with 8YSZ, it produced fluorite-type zirconates such as $Nd_{0.25}Zr_{0.75}O_{1.875}$ and $Nd_{0.5}Zr_{0.5}O_{1.75}$.

The molten sulphate salt affects the destruction of phases in the TBC system. The phase of fluorite was the result of the fluxing process, as previously explained by Rapp **[30]**. In this work, corrosion was observed due to the combination of liquid Na_2SO_4 deposits with a ceramic blend of $Nd_2Zr_2O_7$ and 8YSZ, causing the dissolution of both acidic and basic oxides. Corrosion was only possible in the presence of skinny layers of dissolved salt that enable the passage of oxidising gases and ions, as seen in this study. The products resulting from the degradation of Na_2SO_4 helped in the dissolution of oxides as indicated in Equations **(1)-(3).**

$$Na_2SO_4 \rightarrow Na_2O_{(liquid)} + SO_{3\,(gas)} \quad (1)$$

$$Na_2O_{(liquid)} + Nd_2O_3 \rightarrow 2NaNdO_2\ (basic\ reaction) \quad (2)$$

$$\Delta H_{calc} = -0.718\ eV\ (-69\ KJmol^{-1})$$

$$ZrO_2 + 2SO_{3(gas)} \rightarrow Zr(SO_4)_2\ (acidic\ reaction) \quad (3)$$

$$\Delta H_{calc} = -1.834\ eV\ (-177\ KJmol^{-1})$$

Salts may re-precipitate when they interact with each other, as illustrated in **Equation (4)**.

$$8NaNdO_2 + 2Zr(SO_4)_2 \rightarrow Nd_2Z_2O_7 + 4Na_2SO_4 + 3Nd_2O_3 \quad (4)$$

$$\Delta H_{calc} = -13.348\ eV\ (-1288\ KJmol^{-1})$$

Thermodynamic investigations support the feasibility of this process. The reaction described in **Eq. (4)** promotes the development of fluorite phases such as $Nd_{0.25}Zr_{0.75}O_{1.875}$. This phase can also arise from the reduction of the $Nd_2Zr_2O_7$ pyrochlore phase within the Nd_2O_3 oxide. Furthermore, the regeneration of Na_2SO_4 and Nd_2O_3 is crucial in sustaining the self-sustaining process known as "synergistic hot corrosion." This process leads to the disintegration of the external layer of the ceramic zone within the thermal barrier coating system, resulting in minimal formation of corrosion by-products. This specific phenomenon was noted in the current investigation at a temperature of 920 °C.

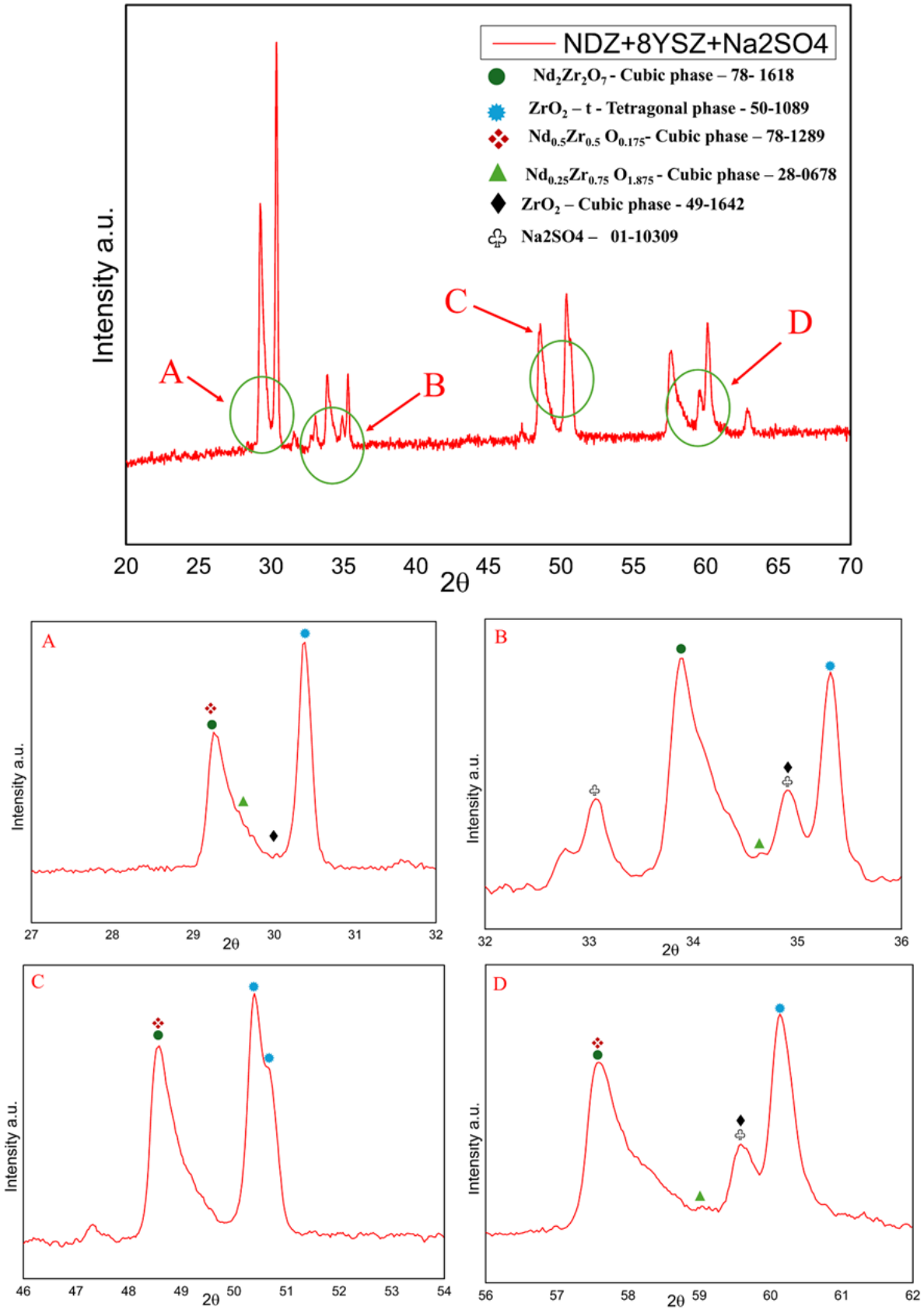

Figure 6.2: XRD pattern of 50 $Nd_2Zr_2O_7$ + 50 8YSZ after hot corrosion at 920 °C in liquid Na_2SO_4 salt.

A similar degradation pattern was observed in our prior studies, which examined different thermal barrier coating compositions under exposure to pure sodium sulfate [**31-33**]. **Figure 6.4** shows the surface morphology of the thermal barrier coating systems at a high temperature of 920 °C, exposed to liquid sodium sulphate. The influence of long-term high-temperature interaction is observed in the formation of fine-grained structural elements, and there is also a significant influence of chemically induced thermal etching. Large numbers of microscopic pits were observed near the existing micropores and microcracks, indicating a gradual degradation of the surface.

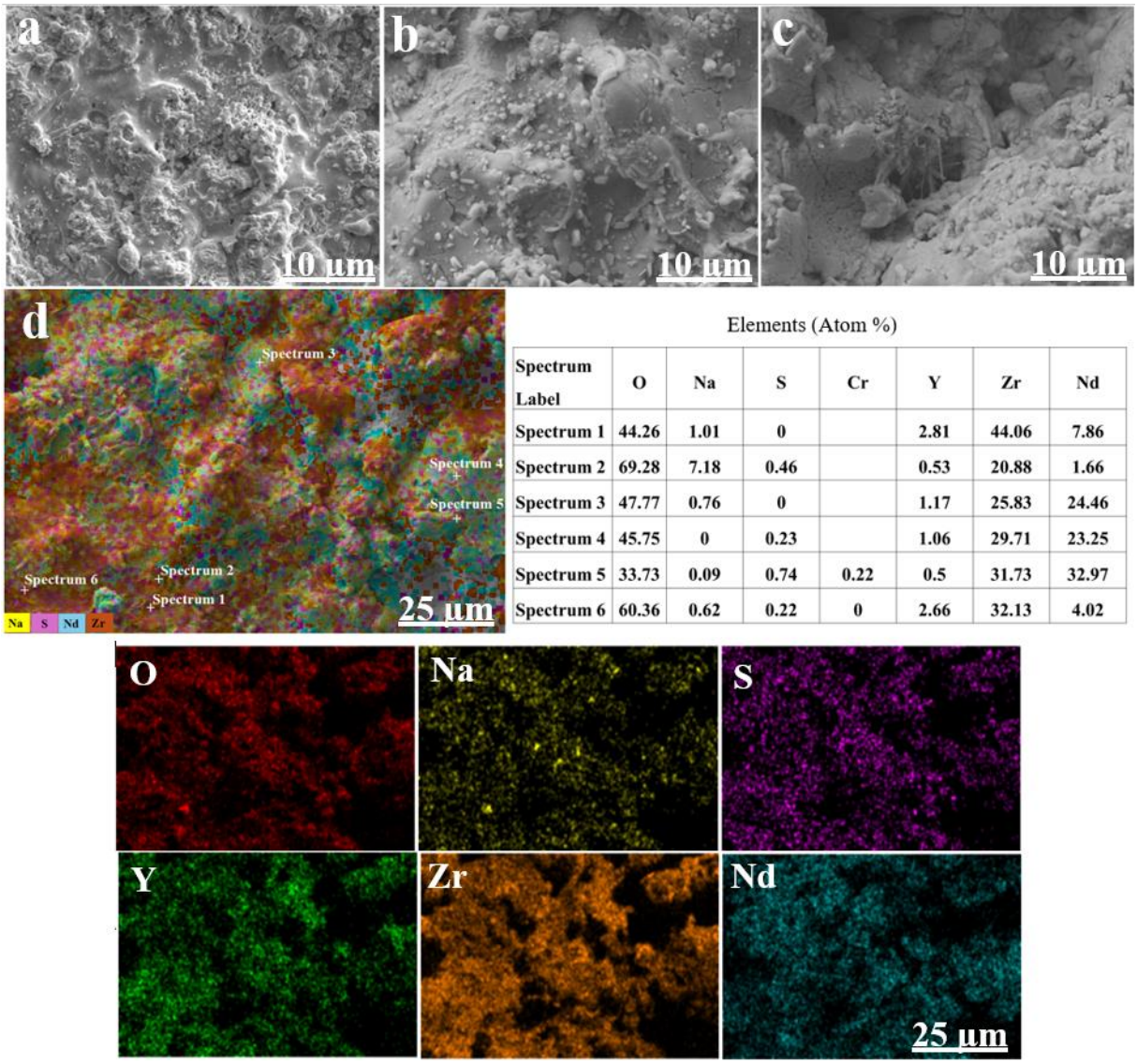

Elements (Atom %)

Spectrum Label	O	Na	S	Cr	Y	Zr	Nd
Spectrum 1	44.26	1.01	0		2.81	44.06	7.86
Spectrum 2	69.28	7.18	0.46		0.53	20.88	1.66
Spectrum 3	47.77	0.76	0		1.17	25.83	24.46
Spectrum 4	45.75	0	0.23		1.06	29.71	23.25
Spectrum 5	33.73	0.09	0.74	0.22	0.5	31.73	32.97
Spectrum 6	60.36	0.62	0.22	0	2.66	32.13	4.02

Figure 6.3: Surface morphology and chemical composition of 50 $Nd_2Zr_2O_7$ + 50 8YSZ TBC systems following hot corrosion at 920 °C for 224 hours in molten Na_2SO_4 salt.

Moreover, significant etching was also noted due to surface cracks, which, unlike those created immediately after thermal spraying, had a non-uniform geometry, i.e., serrated and irregular edges. There was also a significant enhancement of surface roughness, which further accentuated the degradation caused by thermal and chemical interactions. Analysis of energy-dispersive spectroscopy revealed separate regions with chemical compositions of either 8 mol% yttria-stabilised zirconia (8YSZ) or neodymium zirconates (NZO), indicating that these phases remained intact under intense environmental conditions. Furthermore, regions exhibiting a strong concentration of sulphur and sodium, along with a low concentration of chromium, were identified. The accumulation of these elements suggests potential chemical reactions at the surface, contributing to the observed morphological transformations.

The results of the research on the degradation of the microstructure of the $Nd_2Zr_2O_7$ + 8YSZ TBC system, subjected to corrosion resistance tests in a liquid Na_2SO_4 salt environment, demonstrated its high efficiency as a protective coating **Fig. 6.5(a-c)**.

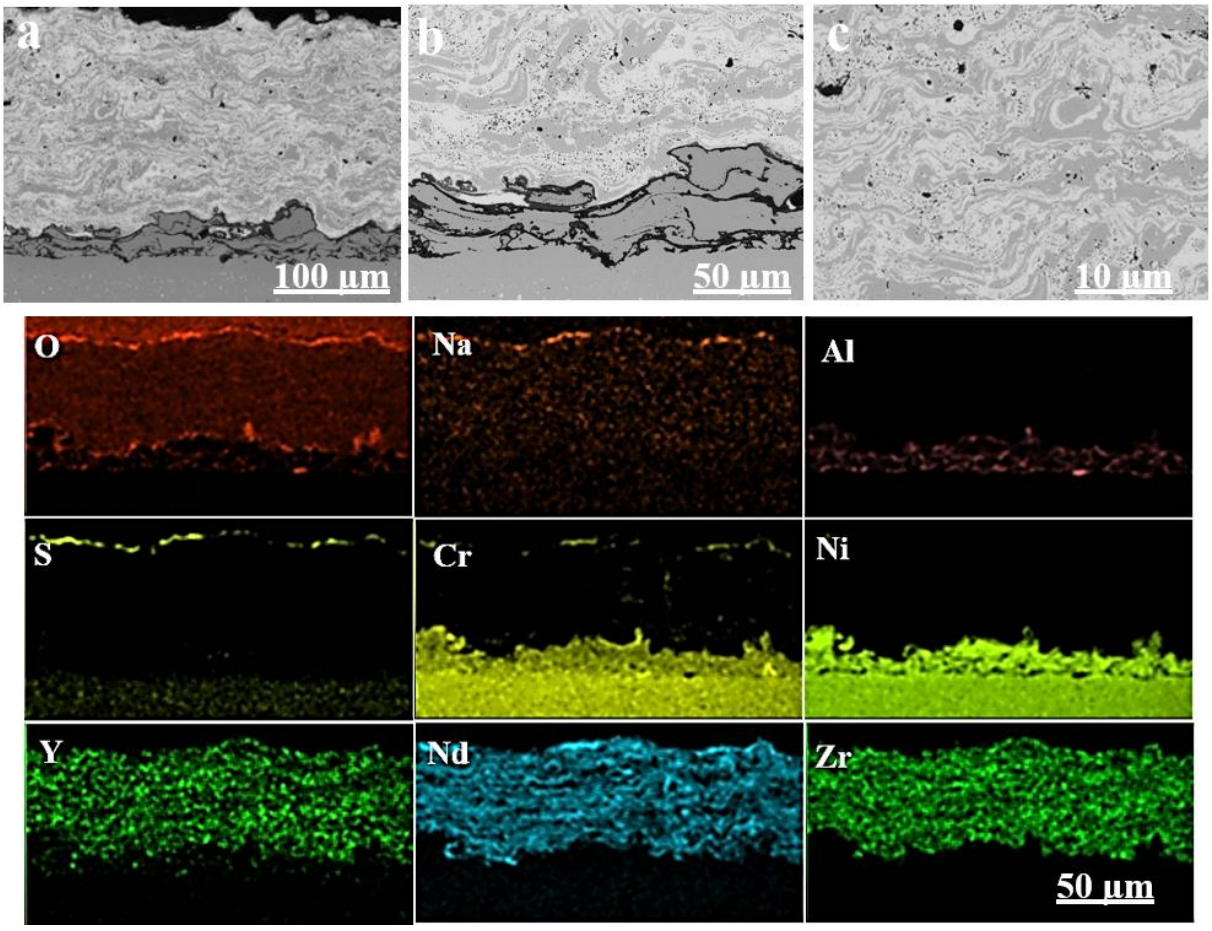

Figure 6.4: Cross-sectional SEM/EDX images composition of 50 $Nd_2Zr_2O_7$ + 50 8YSZ TBC systems following hot corrosion at 920 °C for 224 hours in molten Na_2SO_4 salt.

No significant effects related to the corrosion destruction processes were found. There were no horizontal cracks, usually located near the TGO zone. Moreover, no signs of decomposition or disintegration of individual phase components, i.e. $Nd_2Zr_2O_7$ and 8YSZ, were observed. However, the presence of numerous minimal spherical voids, located solely in the zirconate phase, is noticeable. Similar effects were observed in the Migas work **[15]**. Analysis of the surface distributions of the elements included in the TBC system (Nd, Zr, Y, Ni, Cr, Al, Y, O) and salt components (Na, S) showed Na and S dominate on the external surface of the TBC. In the case of sodium, it is also visible in the form of small point clusters in the volume of the ceramic layer, which may suggest sodium diffusion through the network of cracks and pores. In the case of sulphur, this effect was not observed.

6.3.3 Hot Corrosion in a Mixture of Na_2SO_4 and $MgSO_4$

In **Figure 6.6**, the X-ray diffraction patterns show the phase composition of the NZO/8YSZ coatings after exposure to hot corrosion in a 50/50 mol% Na_2SO_4-$MgSO_4$ environment. The main components found in the upper section of the topcoats are t-ZrO_2, p-$Nd_2Zr_2O_7$, $Nd_{0.5}Zr_{0.5}O_{1.75}$, and $Nd_{0.25}Zr_{0.75}O_{1.875}$, characterised by fluorite structures (non-stoichiometric compounds), along with MgO. Initially, Na_2SO_4 and $MgSO_4$ react to form a low-temperature eutectic compound, L ↔ $Mg_3Na_2(SO_4)_4$ + hexagonal at 660 °C, which causes severe corrosion **[34,35**]. At 920 °C, their eutectic behaviour produces a stable liquid phase that enhances the mobility of Na^+ and Mg^{2+} ions. This liquid phase accelerates the dissolution and transport of these ions, creating a highly corrosive environment that significantly increases the degradation rate **[36]**. The presence of strong and distinct peaks of the $Nd_{0.5}Zr_{0.5}O_{1.75}$ phase suggests that the decomposition process in mixed magnesium and sodium sulphate salts exhibits significantly stronger activity than hot corrosion in sodium sulphate liquid deposits.

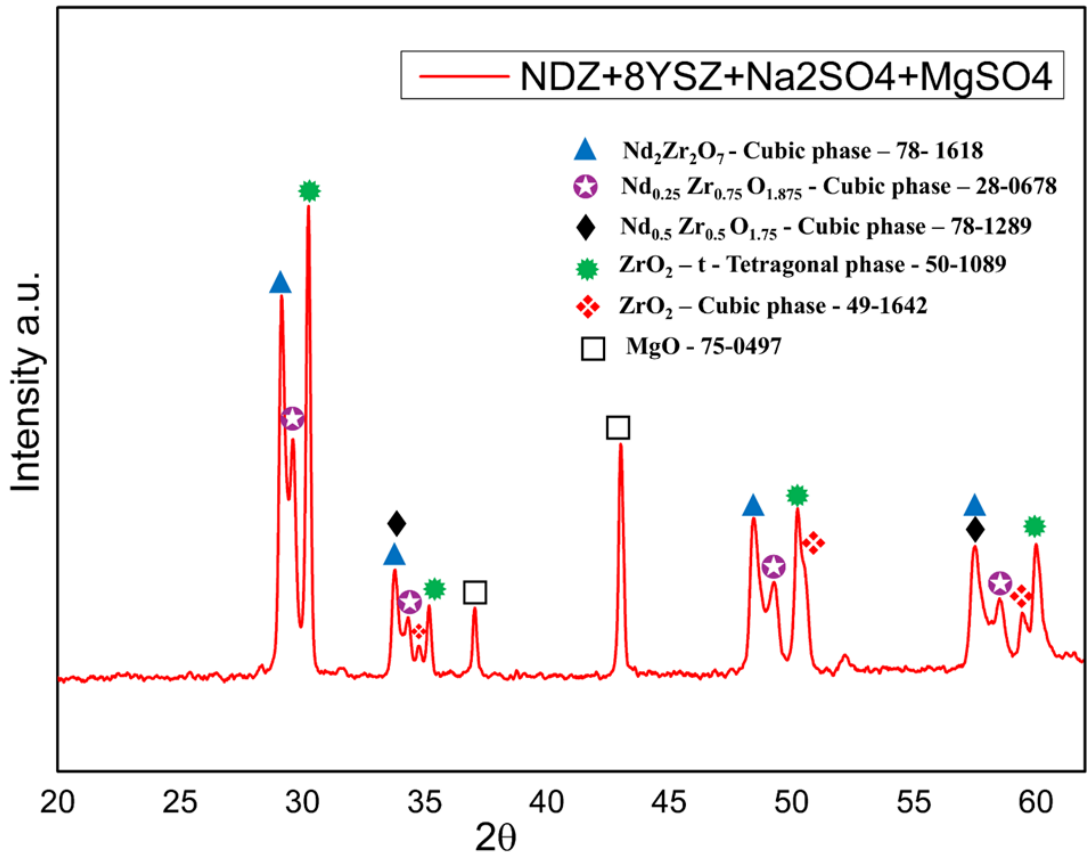

Figure 6.5: XRD pattern of 50 $Nd_2Zr_2O_7$ + 50 8YSZ after corrosion at 920 °C in the mixture of Na_2SO_4 + $MgSO_4$ salt.

Figure 6.7 illustrates the SEM analysis of the corroded $Nd_2Zr_2O_7$ + 8YSZ sample following exposure to Na_2SO_4 + $MgSO_4$ molten salts, revealing distinct signs of microstructural damage due to hot corrosion. Severe grain boundary deterioration, crack formation, and greater porosity are observed in the surface structure, indicating significant material degradation. Intergranular cracks suggest that the primary corrosion process occurs along grain boundaries, likely due to the removal of Nd and Y from the NZO and 8YSZ phases. Such cracks open pathways through which molten salts can enter, exacerbating the corrosion process even further. Additionally, the SEM images reveal bright secondary phase deposits, indicating that corrosion products have formed.

The deposits are likely due to chemical reactions between the molten salts and the ceramic material, resulting in the formation of MgO and cubic ZrO_2. Even though these compounds are corrosion-resistant, they change the original material structure. The surface appears porous and rough, indicating the dissolution of the phases and loss of material. The EDS sample of the corroded surface also identified sulphur (S), sodium (Na) and magnesium (Mg), indicating the presence of sulphate-based reaction products. Little chromium (Cr) was also present, which could have been an external contaminant or a result of diffusion from the surrounding materials

[15]. Further surface examination revealed areas with varying contrast, indicating localised phase separations. This could result from the transformation of pyrochlore NZO into a fluorite phase, thereby affecting material stability and increasing defect formation. The SEM and EDS findings collectively indicate that molten salt infiltration, selective element leaching, and reaction product formation play crucial roles in the material's structural changes under high-temperature corrosion conditions.

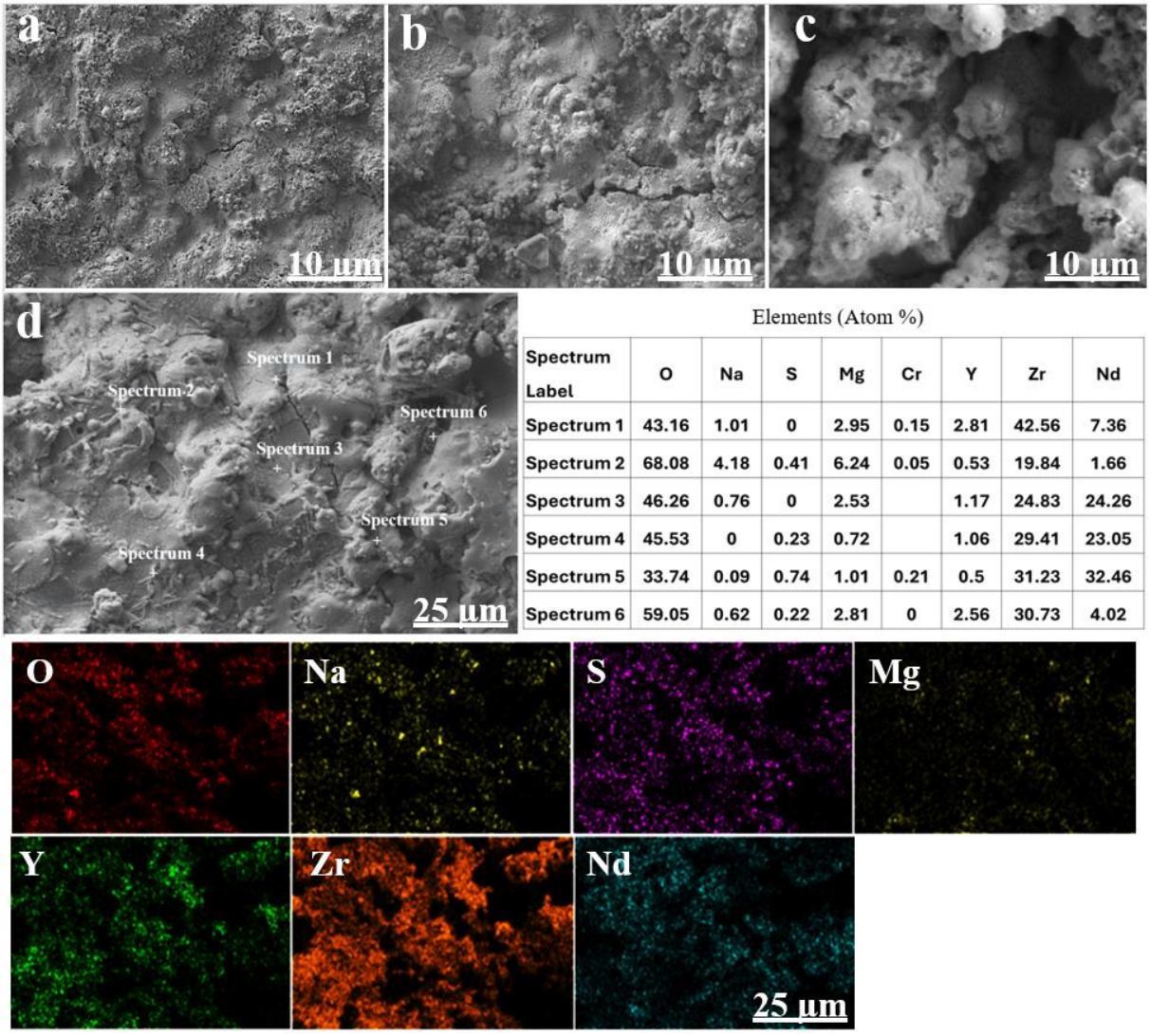

Elements (Atom %)

Spectrum Label	O	Na	S	Mg	Cr	Y	Zr	Nd
Spectrum 1	43.16	1.01	0	2.95	0.15	2.81	42.56	7.36
Spectrum 2	68.08	4.18	0.41	6.24	0.05	0.53	19.84	1.66
Spectrum 3	46.26	0.76	0	2.53		1.17	24.83	24.26
Spectrum 4	45.53	0	0.23	0.72		1.06	29.41	23.05
Spectrum 5	33.74	0.09	0.74	1.01	0.21	0.5	31.23	32.46
Spectrum 6	59.05	0.62	0.22	2.81	0	2.56	30.73	4.02

Figure 6.6: Surface morphology and chemical composition of 50 $Nd_2Zr_2O_7$ + 50 8YSZ TBC systems after hot corrosion at 920 °C for 224 hours in a Na_2SO_4 + $MgSO_4$ salt mixture.

The degradation of the microstructure of the $Nd_2Zr_2O_7$-8YSZ TBC system, subjected to corrosion resistance tests in a mixture of liquid Na_2SO_4 and $MgSO_4$ salt environment, is shown in **Fig. 6.8(a-c)**. In this case, the degradation of the ceramic layer is significantly more advanced than that of pure Na_2SO_4. Especially, the presence of large horizontal microcracks is revealed,

which are localised near the bond coat peaks with a thick oxide layer on roughness profile peaks. Much shorter vertical cracks are also visible. Contrary to hot corrosion degradation in pure Na_2SO_4, the presence of small pores in the zirconate compound was not detected on a comparable scale. This suggests that other mechanisms of destruction may have occurred in this variant of the test (crack formation). Analysis of the surface distributions of the elements included in the TBC system (Nd, Zr, Y, Ni, Cr, Al, O) and salt components (Na, Mg, S) showed that only Mg dominates the external surface of the TBC. In the case of sodium and sulphur, they are visible in the form of higher concentrations than in the earlier case, point clusters in the volume of the ceramic layer, which suggest sodium and sulphur diffusion through the network of vertical cracks.

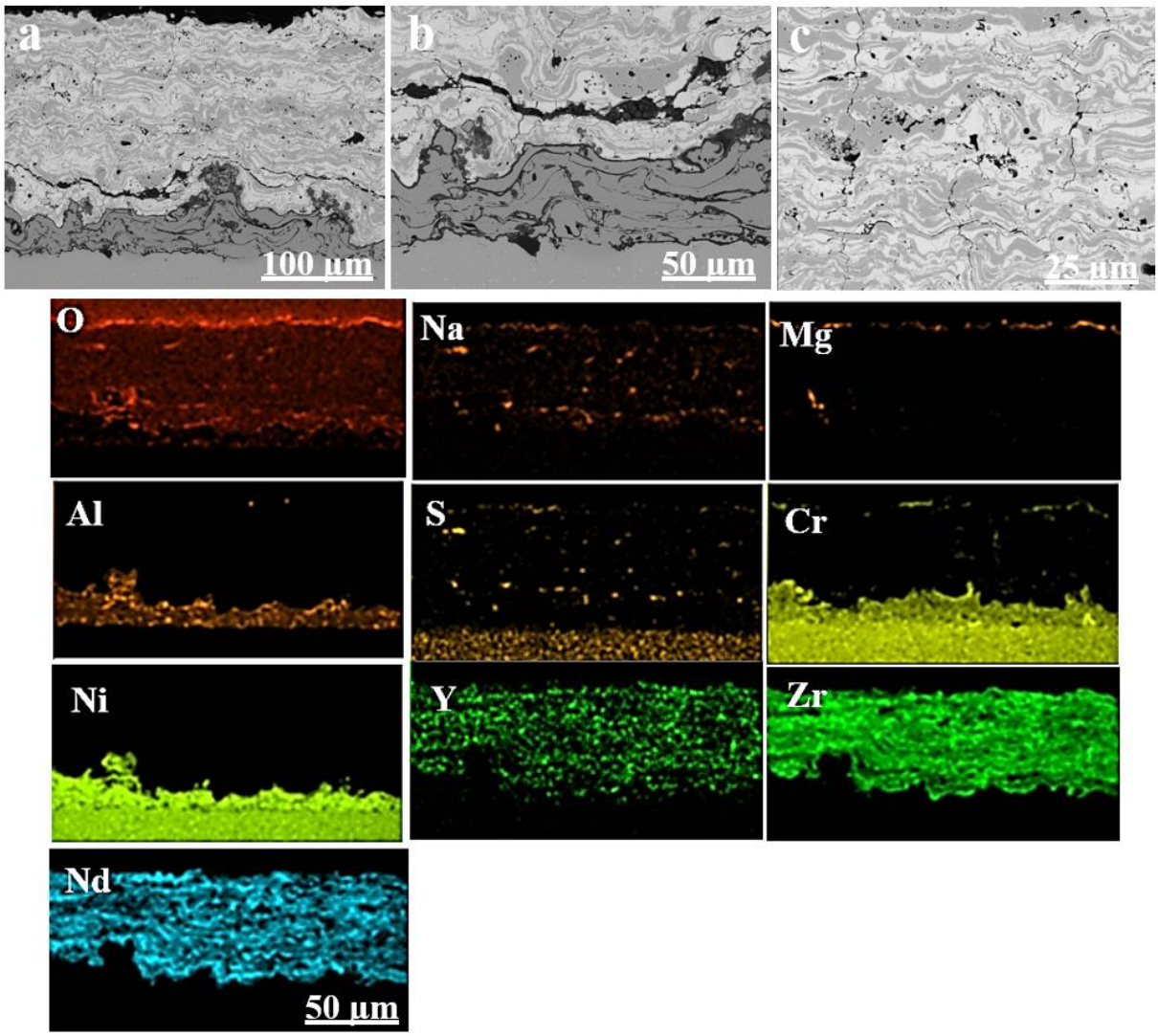

Figure 6.7: Cross-sectional SEM/EDX images composition of 50 $Nd_2Zr_2O_7$ + 50 8YSZ TBC systems following hot corrosion at 920 °C for 224 hours in Na_2SO_4 + $MgSO_4$ salt mixture.

6.3.4 Hot Corrosion in a mixture of Na_2SO_4 and V_2O_5

Figure 6.9 presents the XRD analysis of 50 NZO + 50 8YSZ composite coatings that underwent a hot corrosion test at 920 °C for 64 hours in a mixture of 50 % Na_2SO_4 and 50% V2O5. The XRD results indicate that the primary corrosion products are $NdVO_4$, YVO_4 monoclinic zirconia (m-ZrO_2), and tetragonal zirconium oxide (t-ZrO_2). The formation of these products signifies the interaction between the corrosive salts and the ceramic topcoat, as well as the production of $NdVO_4$ crystalline structures. Based on the current study and corroborating research [**37,38**], the formation mechanism of corrosion products in NZO + 8YSZ coatings can be attributed to the interaction of Na_2SO_4 and V_2O_5. Initially, Na_2SO_4 does not react directly with NZO + 8YSZ but interacts with V_2O_5, forming the eutectic compound $NaVO_3$. This $NaVO_3$ reacts with NZO and 8YSZ to produce $NdVO_4$, YVO_4, and m-ZrO_2. According to the current investigation and supporting scholarly literature, the possible reactions are as follows (**Equations 5-7**) [**39,40**].

$$Na_2SO_4(l) + V_2O_5(l) \rightarrow 2NaVO_3(l) + SO_3(g) \quad (5)$$

$$Zr_2Y_2O_3(s) + 2NaVO_3 \rightarrow 2YVO_4(s) + m - ZrO_2(l) + Na_2O(l) \quad (6)$$

$$Nd_2Zr_2O_7 + 2NaVO_3 \rightarrow 2NdVO_4(s) + m - ZrO_2(l) + Na_2O(l) \quad (7)$$

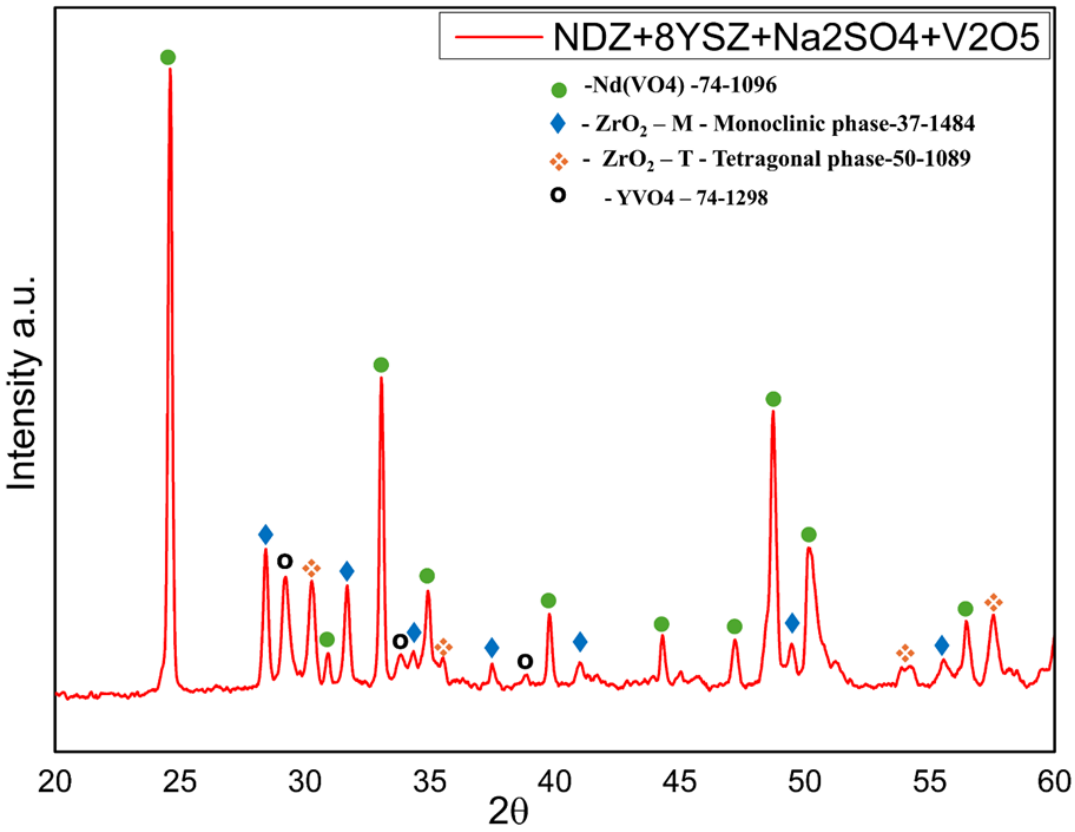

Figure 6.8: XRD pattern of 50 $Nd_2Zr_2O_7$ + 50 8YSZ after hot corrosion test at 920 °C in the mixture of Na_2SO_4 + V_2O_5 salt.

Figure 6.10 (a, b) presents a detailed examination of the surface morphology and EDS analysis of the NZO + 8YSZ thermal barrier coating exposed to hot corrosion in a 50/50 mol. % mixture of sodium sulphate and vanadium pentoxide. This study identified the presence of $NdVO_4$, YVO_4, and monoclinic zirconia (m-ZrO_2). The rod-like crystalline structures observed on the coating surface correspond primarily to $NdVO_4$, indicating that it is the predominant corrosion product. The formation of the YVO_4 phase is relatively low, suggesting a higher concentration of $Nd_2Zr_2O_7$ in the outer topcoat compared to 8YSZ in the composite coatings. Furthermore, the surface morphology demonstrates significant interaction between the corrosive mixture and the ceramic topcoat. Evidence of spallation in certain regions further confirms the aggressive nature of the corrosion process.

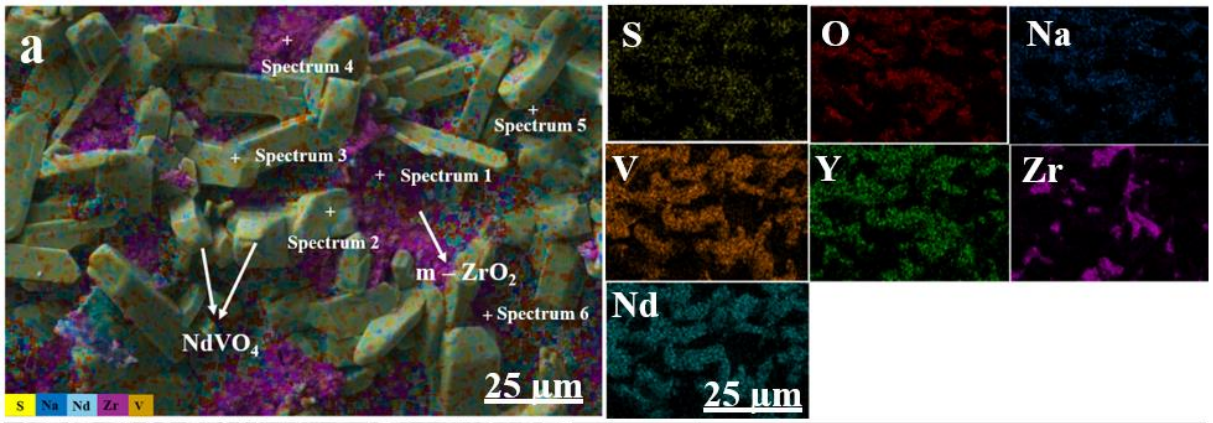

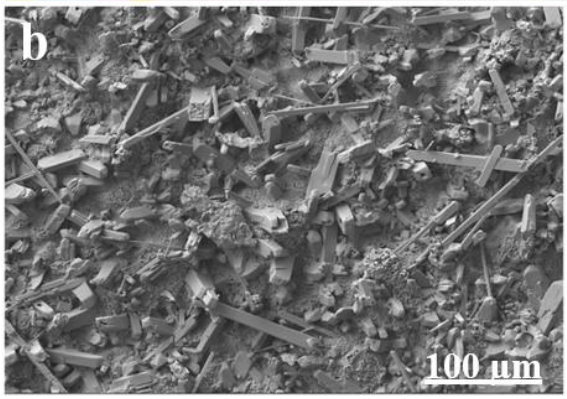

Spectrum Label	Elements (atom%)							
	O	Na	S	V	Y	Zr	Nd	Total
Spectrum 1	66.8	0	0	3.11	0.04	27.79	2.25	100
Spectrum 2	66.62	0.07	0	16.63	1.97	0	14.71	100
Spectrum 3	66.95	0.31	0	17.68	1.13	0	13.93	100
Spectrum 4	66.41	0.67	0	1.25	0	30.88	0.79	100
Spectrum 5	66.98	0.33	0	17.77	0	0	14.92	100
Spectrum 6	65.02	3.45	0	13.72	1.66	4.56	11.59	100

Figure 6.9: Surface morphology and chemical composition of 50 $Nd_2Zr_2O_7$ + 50 8YSZ TBC systems after hot corrosion at 920°C for 64 hours in a Na_2SO_4 + V_2O_5 salt mixture.

6.4 Conclusion

The microstructural studies conducted, along with those characterising the behaviour of the TBC coating system type 50 $Nd_2Zr_2O_7$ + 50 8YSZ, under the conditions of sulphate salts in the presence of vanadium oxide, revealed the following:

- In an as-sprayed condition, the pyrochlore phase of $Nd_2Zr_2O_7$ was partially decomposed into non-stoichiometric compounds with a fluorite-type network. This phenomenon is a result of doping pyrochlore with Y_2O_3 oxide, derived from 8YSZ, which led to a state in which the more stable phase is a zirconate compound with a fluorite-type lattice.
- Under the hot-corrosion test conditions, the decomposition process of the pyrochlore phase was intensified. However, the intensity of the degradation phenomena was moderate. Another significant effect of degradation was the formation of numerous ultrafine voids in the zirconate phase, a phenomenon also confirmed in other binary systems, such as $Gd_2Zr_2O_7$ + 8YSZ or $Sm_2Zr_2O_7$ + 8YSZ.
- The degradation processes of the $Nd_2Zr_2O_7$ + 8YSZ system were significantly more intense when degradation occurred in an environment containing a mixture of sodium and magnesium sulphate salts. As a result of the lowered melting temperature of such a mixture compared to pure sodium sulphate salt, a much greater penetration of the corrosive atmospheric components into the ceramic layer was observed.
- Analysis of the tested system in an environment containing Na_2SO_4 salt and vanadium oxide demonstrated complete decomposition of neodymium zirconate, resulting in the formation of neodymium vanadate, as well as partial decomposition of the 8YSZ phase, which produced yttrium vanadate and monoclinic zirconium oxide.

References

[1] H. Dai, X. Zhong, J. Li, J. Meng, and X. Cao, “Neodymium-cerium oxide as new thermal barrier coating material,” *Surf. Coatings Technol.*, vol. 201, no. 6, pp. 2527–2533, 2006, doi: 10.1016/j.surfcoat.2006.04.016.

[2] B. Cheng *et al.*, “Sintering governing the cracking behaviors of different La2Zr2O7/YSZ ceramic layer combination TBCs at 1150 °C,” *Surf. Coatings Technol.*, vol. 428, no. November, p. 127910, 2021, doi: 10.1016/j.surfcoat.2021.127910.

[3] A. Iqbal, G. Moskal, A. Cavaleiro, A. Amjad, and M. J. khan, “The current advancement of zirconate based dual phase system in thermal barrier coatings (TBCs): New modes of the failures: Understanding and investigations,” *Alexandria Eng. J.*, vol. 91, no. February, pp. 161–196, 2024, doi: 10.1016/j.aej.2024.01.063.

[4] A. Avcı, M. Karabaş, A. Akdoğan, and E. Erhan, “Optimization of laser process parameters and improved corrosion behaviour of LZ / YSZ thermal barrier coating,” vol. c, 2025.

[5] X. Guo *et al.*, “Thermal properties of La 2 Zr 2 O 7 double-layer thermal barrier coatings,” *Adv. Appl. Ceram.*, vol. 118, no. 3, pp. 91–97, 2019, doi: 10.1080/17436753.2018.1510820.

[6] A. Iqbal and G. Moskal, *Recent Development in Advance Ceramic Materials and Understanding the Mechanisms of Thermal Barrier Coatings Degradation*, vol. 30, no. 8. Springer Netherlands, 2023. doi: 10.1007/s11831-023-09960-7.

[7] J. Rahimi, N. Choupani, E. Poursaeidi, F. Montakhabi, M. J. Sigaroodi, and Y. Y. Jamalabad, “Investigation of the hot corrosion effects on the lifetime of TBCs with and without TC,” *J. Alloys Compd.*, vol. 1004, no. August, p. 175840, 2024, doi: 10.1016/j.jallcom.2024.175840.

[8] G. Bhavesh, P. Hariharan, and D. Dhinasekaran, “Assessment of the microstructural features and electrochemical corrosion behaviour of nanostructured Gd2Zr2O7 EB-PVD TBCs under three salt conditions,” *Surf. Coatings Technol.*, vol. 487, no. April, p. 130991, 2024, doi: 10.1016/j.surfcoat.2024.130991.

[9] A. Keyvani, M. Saremi, and M. Heydarzadeh Sohi, “Microstructural stability of zirconia-alumina composite coatings during hot corrosion test at 1050 °c,” J. Alloys Compd., vol. 506, no. 1, pp. 103–108, 2010, doi: 10.1016/j.jallcom.2010.06.110.

[10] A. Keyvani, M. Saremi, and M. H. Sohi, “An investigation on oxidation, hot corrosion and mechanical properties of plasma-sprayed conventional and nanostructured YSZ coatings,” Surf. Coatings Technol., vol. 206, no. 2–3, pp. 208–216, 2011, doi: 10.1016/j.surfcoat.2011.06.036.

[11] P. Soltani, A. Keyvani, and M. Bahamirian, “Evolution of hot corrosion resistance of conventional CSZ and MoSi2 self-healing thermal barrier coatings in Na2SO4+V2O5 at 950 °C,” Ceram. Int., vol. 48, no. 7, pp. 9038–9050, 2022, doi: 10.1016/j.ceramint.2021.12.087.

[12] I. Parchovianská, M. Parchovianský, A. Nowicka, A. Prnová, P. Švančárek, and A. Pakseresht, “Effect of sintering temperature on phase evolution, microstructure, and mechanical properties of La2Ce2O7/40 wt.% YSZ composite ceramics,” *J. Mater. Res. Technol.*, vol. 24, pp. 4573–4586, 2023, doi: 10.1016/j.jmrt.2023.04.054.

[13] A. ÖZÇELİK, A. AKDOĞAN EKER, M. KARABAŞ, A. AVCI, and B. O. KÜÇÜKYILDIRIM, “Enhanced CMAS and hot corrosion degradation of YSZ thermal barrier coating with nano powders,” *Surf. Coatings Technol.*, vol. 481, no. March, 2024, doi: 10.1016/j.surfcoat.2024.130624.

[14] A. Pakseresht, S Ariharan, A. Sekar, M. Parchoviansky´1, and P. Parchoviansky´1, “Investigating Hot corrosion, CMAS, and Thermal Shock Behaviour of Double-layer YSZ/La 2 Ce 2 O 7 + YSZ Thermal Barrier Coatings,” *J. Therm. Spray Technol.*, p. 01845, 2024, doi: 10.1007/s11666-024-01845-w.

[15] D. Migas, G. Moskal, and S. Jucha, “Hot corrosion behavior of double-phase Nd2Zr2O7-YSZ thermal barrier coatings,” *Surf. Coatings Technol.*, vol. 449, no. September, p. 128955, 2022, doi: 10.1016/j.surfcoat.2022.128955.

[16] K. Yan *et al.*, “Hot corrosion mechanism and thermal cycling performance of air-plasma-sprayed LaYbZr2O7 thermal barrier coatings in the vanadate-containing molten salts,” *Surf. Coatings Technol.*, vol. 472, no. June, p. 129925, 2023, doi: 10.1016/j.surfcoat.2023.129925.

[17] A. C. Karaoglanli, Y. Ozgurluk, A. Gulec, D. Ozkan, and G. Binal, “Effect of coating degradation on the hot corrosion behavior of yttria-stabilized zirconia (YSZ) and blast furnace slag (BFS) coatings,” *Surf. Coatings Technol.*, vol. 473, no. September, p. 130000, 2023, doi: 10.1016/j.surfcoat.2023.130000.

[18] A. R. Patil and S. T. Vagge, “Oxidation and hot corrosion behaviour of functionally graded yttria stabilized zirconia and lanthanum zirconate thermal barrier coatings,” *Surf. Coatings Technol.*, vol. 474, no. September, p. 130059, 2023, doi: 10.1016/j.surfcoat.2023.130059.

[19] R. Pourshahsavari, A. Yaghtin, and N. Hosseinabadi, “Hot corrosion and thermal shock performance of nanoparticulate YSZ coatings deposited via suspension plasma spraying (SPS),” *Mater. Chem. Phys.*, vol. 297, no. October 2022, p. 127406, 2023, doi: 10.1016/j.matchemphys.2023.127406.

[20] J. Che, X. Wang, X. Liu, G. Liang, and S. Zhang, “Thermal transport property in pyrochlore-type and fluorite-type A2B2O7 oxides by molecular dynamics simulation,” *Int. J. Heat Mass Transf.*, vol. 182, p. 122038, 2022, doi: 10.1016/j.ijheatmasstransfer.2021.122038.

[21] J. Feng *et al.*, “Electronic structure, mechanical properties and thermal conductivity of Ln2Zr2O7 (Ln = La, Pr, Nd, Sm, Eu and Gd) pyrochlore,” *Acta Mater.*, vol. 59, no. 4, pp. 1742–1760, 2011, doi: 10.1016/j.actamat.2010.11.041.

[22] B. Liu, J. Y. Wang, Y. C. Zhou, T. Liao, and F. Z. Li, “Theoretical elastic stiffness, structure stability and thermal conductivity of La2Zr2O7 pyrochlore,” *Acta Mater.*, vol. 55, no. 9, pp. 2949–2957, 2007, doi: 10.1016/j.actamat.2006.12.035.

[23] Y. Wang *et al.*, “CMAS corrosion behavior of interface for EB-PVD Gd2Zr2O7/YSZ thermal barrier coatings,” *Mater. Today Commun.*, vol. 41, no. September, p. 110756, 2024, doi: 10.1016/j.mtcomm.2024.110756.

[24] D. Li, P. Jiang, R. Gao, F. Sun, X. Jin, and X. Fan, “Experimental and numerical investigation on the thermal and mechanical behaviours of thermal barrier coatings exposed to CMAS corrosion,” *J. Adv. Ceram.*, vol. 10, no. 3, pp. 551–564, 2021, doi: 10.1007/s40145-021-0457-2.

[25] W. Ma *et al.*, “Unsatisfactory CMAS resistance of Gd2Zr2O7 thermal barrier coatings and the solution strategy based on laser surface modification,” *Ceram. Int.*, vol. 50, no. 18, pp. 31859–31868, 2024, doi: 10.1016/j.ceramint.2024.05.483.

[26] L. Guo, X. Zhang, M. Liu, S. Yang, and J. W. Dai, “CMAS + sea salt corrosion to thermal barrier coatings,” *Corros. Sci.*, vol. 218, no. December 2022, p. 111172, 2023, doi: 10.1016/j.corsci.2023.111172.

[27] G. Moskal, A. Jasik, M. Mikuśkiewicz, and S. Jucha, “Thermal resistance determination of Sm2Zr2O7 + 8YSZ composite type of TBC,” *Appl. Surf. Sci.*, vol. 515, no. March, p. 145998, 2020, doi: 10.1016/j.apsusc.2020.145998.

[28] Du, H. "Thermodynamic assessment of the K2SO4-Na2SO4-MgSO4-CaSO4 system," JPE vol. 21, p. 6–18 (2000). https://doi.org/10.1361/105497100770340363.

[29] G. Moskal, “Microstructural characterization of plasma sprayed Ln2Zr2O7 thermal barrier coatings by electron microscopy methods,” *Microsc. Res. Tech.*, vol. 83, no. 5, pp. 523–530, 2020, doi: 10.1002/jemt.23441.

[30] R. A. Rapp, “Hot corrosion of materials: A fluxing mechanism?,” *Corros. Sci.*, vol. 44, no. 2, pp. 209–221, 2002, doi: 10.1016/S0010-938X(01)00057-9.

[31] G. Moskal, S. Jucha, M. Mikuśkiewicz, D. Migas, and A. Jasik, “Atypical decomposition processes of Sm2Zr2O7 + 8YSZ dual-phase TBCs during hot corrosion,” *Corros. Sci.*, vol. 170, no. December 2019, p. 108681, 2020, doi: 10.1016/j.corsci.2020.108681.

[32] A. Iqbal, G. Moskal, and B. Witala, “Degradation mechanism of dual-phase thermal barrier coatings Gd2Zr2O7 + 8YSZ under hot corrosion ambience Na 2 SO 4,” *J. Therm. Anal. Calorim.*, 2024, doi: 10.1007/s10973-024-13784-3.

[33] D. Migas, G. Moskal, and S. Jucha, “Hot corrosion behavior of double-phase Nd2Zr2O7-YSZ thermal barrier coatings,” *Surf. Coatings Technol.*, vol. 449, no. April, p. 128955, 2022, doi: 10.1016/j.surfcoat.2022.128955.

[34] M. Wang and B. O. Sundman, “Thermodynamic Assessment of the,” *J. Am. Ceram. Soc.*, vol. 21, no. December, pp. 6–18, 2000, doi: http://dx.doi.org/10.1111/j.1551-2916.2004.00683.x.

[35] Khan, M.J., Moskal, G., Iqbal, A., Mikuśkiewicz, M., Pawlik, T. and Olesik, P., 2023. Hot Corrosion Behavior of Single-Layered Gd2Zr2O7, Sm2Zr2O7, and Nd2Zr2O7 Thermal Barrier Coatings Exposed to Na2SO4+ MgSO4 Environment. Coatings, 13(8), “Hot Corrosion Behavior of Single-Layered Gd2Zr2O7, Sm2Zr2O7, and Nd2Zr2O7 Thermal Barrier Coatings Exposed to Na2SO4 + MgSO4 Environment,” vol. 13, no. 8, p. 14, 2023, doi: https://doi.org/10.3390/coatings13081311.

[36] S. Hu, H. Finklea, and X. Liu, “A review on molten sulfate salts induced hot corrosion,” *J. Mater. Sci. Technol.*, vol. 90, pp. 243–254, 2021, doi: 10.1016/j.jmst.2021.03.013.

[37] P. G. Lashmi, S. Majithia, V. Shwetha, N. Balaji, and S. T. Aruna, “Improved hot corrosion resistance of plasma sprayed YSZ/Gd2Zr2O7 thermal barrier coating over single layer YSZ,” *Mater. Charact.*, vol. 147, no. June 2018, pp. 199–206, 2019, doi: 10.1016/j.matchar.2018.11.007.

[38] Y. Ozgurluk, K. M. Doleker, and A. C. Karaoglanli, “Investigation of the effect of V2O5 and Na2SO4 melted salts on thermal barrier coatings under cyclic conditions,” *Anti-Corrosion Methods Mater.*, vol. 66, no. 5, pp. 644–650, 2019, doi: 10.1108/ACMM-12-

2018-2042.

[39] M. Bahamirian, S. M. M. Hadavi, M. Farvizi, M. R. Rahimipour, and A. Keyvani, “Enhancement of hot corrosion resistance of thermal barrier coatings by using nanostructured Gd 2 Zr 2 O 7 coating,” *Surf. Coatings Technol.*, vol. 360, no. June 2018, pp. 1–12, 2019, doi: 10.1016/j.surfcoat.2018.12.113.

[40] M. Tabeshfar, M. Salehi, G. Dini, P. I. Dahl, M. A. Einarsrud, and K. Wiik, “Hot corrosion of Gd2Zr2O7, Gd2Zr2O7/YbSZ, YSZ + Gd2Zr2O7/YbSZ, and YSZ thermal barrier coatings exposed to Na2SO4 + V2O5,” *Surf. Coatings Technol.*, vol. 409, no. July 2020, p. 126718, 2021, doi: 10.1016/j.surfcoat.2020.126718.

[41] Q. Xing *et al.*, “Microstructure and thermal shock resistance of Nd2O3-doped YSZ-based thermal barrier coatings,” *Ceram. Int.*, vol. 46, no. 17, pp. 26841–26853, 2020, doi: 10.1016/j.ceramint.2020.07.160.

[42] T. Yang *et al.*, “Thermal Shock Resistance and Bonding Strength of Novel-Structured Thermal Barrier Coatings with Different Microstructure,” *J. Therm. Spray Technol.*, vol. 31, no. 5, pp. 1540–1555, 2022, doi: 10.1007/s11666-022-01353-9.

Chapter 7: Hot Corrosion Behavior of $Nd_2Ce_2O_7$ + 8YSZ Thermal Barrier Coatings in Sulfate and Vanadate Environments.

7.1 Abstract

The hot corrosion behaviour of air plasma sprayed $Nd_2Ce_2O_7$ + 8YSZ composite thermal barrier coatings was investigated at 920 °C in molten salt environments consisting of pure Na_2SO_4, equimolar Na_2SO_4–$MgSO_4$, and equimolar Na_2SO_4–V_2O_5. Phase stability and microstructural degradation were evaluated using X-ray diffraction (XRD), scanning electron microscopy (SEM), and energy-dispersive spectroscopy (EDS). The as-sprayed coating exhibited a stable dual-phase structure composed of cubic fluorite $Nd_2Ce_2O_7$ and cubic YSZ. Exposure to pure Na_2SO_4 resulted in limited surface reactions, with minor $Nd_2O_2SO_4$ formation and localized monoclinic ZrO_2. In contrast, the Na_2SO_4–$MgSO_4$ environment produced more extensive surface degradation, characterized by compact reaction layers, widespread sulphur distribution, and intensified chemical interactions, indicating enhanced molten salt attack compared with pure Na_2SO_4. The Na_2SO_4–V_2O_5 mixture caused severe degradation, with the formation of $NdVO_4$ and monoclinic ZrO_2, accompanied by extensive surface damage and increased porosity.

Overall, the $Nd_2Ce_2O_7$ + 8YSZ composite coating demonstrated good resistance in pure sulfate environments, increased degradation in mixed sulfate systems, and rapid failure in vanadate-containing salts, highlighting the dominant influence of salt chemistry on hot corrosion behaviour.

7.2 Introduction

Thermal barrier coatings have been extensively employed for many decades in the hot sections of gas turbines and aeroengines to increase the combustion temperature and improve overall engine efficiency, while simultaneously shielding metallic components from oxidation and hot corrosion in severe operating environments. A typical TBC system is composed of multiple layers. The first layer, deposited directly on the metallic substrate, acts as an oxidation- and corrosion-resistant metallic barrier, typically an aluminide or MCrAlY-type coating (where M = Ni, Co, or both). Directly over it is the ceramic layer, which gives thermal insulation and erosion resistance. These layers are typically referred to as the bond coat and the topcoat, respectively. Multi-layered ceramic topcoats with varying physical and thermal characteristics have been explored to improve the thermal performance and service life of TBCs **[1-4]**. Among these, 7–8 wt.% yttria-stabilised zirconia has been the most widely used top-coat material due to its excellent thermal expansion compatibility, low thermal conductivity, and stability within

the operational temperature range of turbine components. However, the tetragonal-to-monoclinic phase transformation of YSZ that occurs near 1170 °C leads to lattice expansion and delamination, limiting its service temperature to below this threshold **[5-7]**. Moreover, commercial fuels contain impurities such as sulfur, vanadium, and sodium that promote hot corrosion of the YSZ coating, resulting in premature failure and a shortened service life. This has led to the creation of new, high-thermal-stability, and corrosion-resistant top-coat materials, which are of significant research interest **[8,9]**.

Materials with pyrochlore and defect-fluorite structures, such as lanthanide zirconates and cerates, have attracted considerable attention as advanced TBC candidates due to their high-temperature phase stability, low thermal conductivity, and chemical durability **[10]**. Pyrochlore-type lanthanide zirconates ($L_2Zr_2O_7$, where L = La, Nd, Sm, Eu, Er, Gd, Dy, Yb, etc.) exhibit significantly lower thermal conductivities (1.1–1.6 $Wm^{-1}K^{-1}$) compared with YSZ **[11]**. Nevertheless, they have a relatively low thermal expansion coefficient (TEC) and fracture toughness, which can lead to poor thermal cycling behaviour. The apparent discrepancy in TEC between the ceramic topcoat and the metallic substrate also remains one of the primary reasons for coating failure **[12-13]**. Replacement of Ce^{4+} by Zr^{4+} of such oxides has been reported to increase the thermal compatibility by enhancing the TEC of such oxides. A number of the lanthanide cerates, such as $La_2Ce_2O_7$, $Er_2Ce_2O_7$, $Yb_2Ce_2O_7$, $Gd_2Ce_2O_7$, $Y_2Ce_2O_7$, and $Dy_2Ce_2O_7$, have hence been investigated in terms of their promising thermophysical characteristics **[14-16]**.

A typical pyrochlore material takes the form of $A_2B_2O_7$ with A a trivalent lanthanide cation (A^{3+}) and B a tetravalent cation (B^{4+}) **[17-18]**. The structure may crystallise in either an ordered pyrochlore or disordered fluorite form, depending on the ionic radius ratio, $R_i^r = R_i(A^{3+})/R_i(B^{4+})$. When $R_i^r \leq 1.45$, the structure generally adopts a defect-fluorite configuration with cation disorder, though some studies suggest a lower boundary near 1.26**[19-22]**. Neodymium cerate ($Nd_2Ce_2O_7$) has a cubic fluorite structure, which is stable at temperatures above 1400 °C, and has several desirable properties at high temperature that make it desirable in high-temperature TBC. Its thermal conductivity (1.6 W m^{-1} K^{-1} at 1423 K) is more than 30 % lower than that of YSZ,[34] while its TEC (12.5–13 × 10^{-6} K^{-1} in the range 373–1523 K) is higher than that of YSZ (10.5–11.5 × 10^{-6} K^{-1}, 293–1273 K) and zirconates such as $Nd_2Zr_2O_7$ and $La_2Zr_2O_7$**[23-25]**. The higher TEC helps reduce thermally induced stresses at the bond coat/top coat interface. Although $Nd_2Ce_2O_7$ exhibits a longer thermal-cycling life than zirconate counterparts, its life remains shorter than that of YSZ; this limitation can be mitigated by constructing double-ceramic-layer or composition-gradient coatings combining $Nd_2Ce_2O_7$ with YSZ **[26,27]**.

In the present work, a $Nd_2Ce_2O_7$ + 8YSZ composite coating was deposited on a nickel-based superalloy substrate using air plasma spraying, incorporating a Co–NiCrAlY bond coat. This composite structure emulates a layer of a gradient-type TBC system. The hot corrosion behaviour of the $Nd_2Ce_2O_7$+ 8YSZ topcoat was systematically examined in three molten salt environments: pure Na_2SO_4, Na_2SO_4+ $MgSO_4$, and Na_2SO_4 + V_2O_5 at elevated temperatures. Although the thermophysical properties of $Nd_2Ce_2O_7$ have been explored previously for TBC applications, comprehensive comparative studies addressing its corrosion resistance against these different sulphate and vanadate-based environments have not yet been reported.

7.3 Results and Discussion

7.3.1 Experimental Procedure

Hot corrosion experiments were conducted on composite $Nd_2Ce_2O_7$ + 8YSZ thermal barrier coating (TBC) specimens to assess their resistance to degradation in various molten salt environments. Three corrosive environments were investigated: pure Na_2SO_4, an equimolar mixture of Na2SO4 and MgSO4, and an equimolar mixture of Na2SO4 and V_2O_5. For each test, pre-weighed salt tablets (0.3 mg) were carefully placed at the centre of the coating surface to minimise edge effects and ensure uniform salt coverage. The specimens were heated in a laboratory furnace with a heating rate of 10 °C min $^{-1}$ kept at 920 °C until the salts melted. The tests were briefly interrupted after 1, 4, and 10 hours to monitor early-stage corrosion processes and then continued in 24-hour exposure cycles. The total exposure time was set to 168 hours for both the pure Na_2SO_4 and Na_2SO_4 + $MgSO_4$ environments, whereas exposure in the more aggressive Na_2SO_4 + V_2O_5 medium was restricted to 48 hours. The specimens were cooled slowly in the furnace after every exposure stage to prevent thermal shock and maintain the integrity of the coating. Scanning electron microscopy (SEM, Hitachi 3400N) was used to analyse the surface morphology, and the energy-dispersive spectroscopy (EDS) was used to analyse localised elements using post-exposure characterization. Additionally, X-ray diffraction (XRD, Phillips X'Pert³ with Cu Kα radiation, λ = 1.54178 Å) was carried out over the 2θ range of 10°–90° to identify phase transformations and corrosion products formed within the $Nd_2Ce_2O_7$ + 8YSZ composite coating during the hot corrosion process.

7.3.2 Phase and Microstructural Features of As-Sprayed TBCs

Figure 7.1 presents the X-ray diffraction (XRD) pattern of the as-sprayed $Nd_2Ce_2O_7$ + 8YSZ composite thermal barrier coating. The diffraction peaks correspond to three distinct phases: the cubic fluorite phase of $Nd_{0.5}Ce_{0.5}O_{1.75}$ (JCPDS 28-0267), the cubic YSZ phase of

$Zr_{0.9}Y_{0.1}O_{1.95}$ (JCPDS 82-1241), and a minor fraction of monoclinic ZrO_2 (JCPDS 37-1484). The dominant reflections associated with the cubic fluorite and YSZ phases confirm the successful deposition and structural stability of both components during plasma spraying. The appearance of weak monoclinic ZrO_2 peaks suggests that the metastable tetragonal YSZ phase was partially converted because of localised overheating in the spraying process. Overall, the XRD analysis reveals that the as-sprayed coating maintains a dual phase composite structure, where $Nd_2Ce_2O_7$ and 8YSZ coexist in their stable cubic forms, ensuring desirable phase compatibility and high-temperature stability for thermal barrier coating applications.

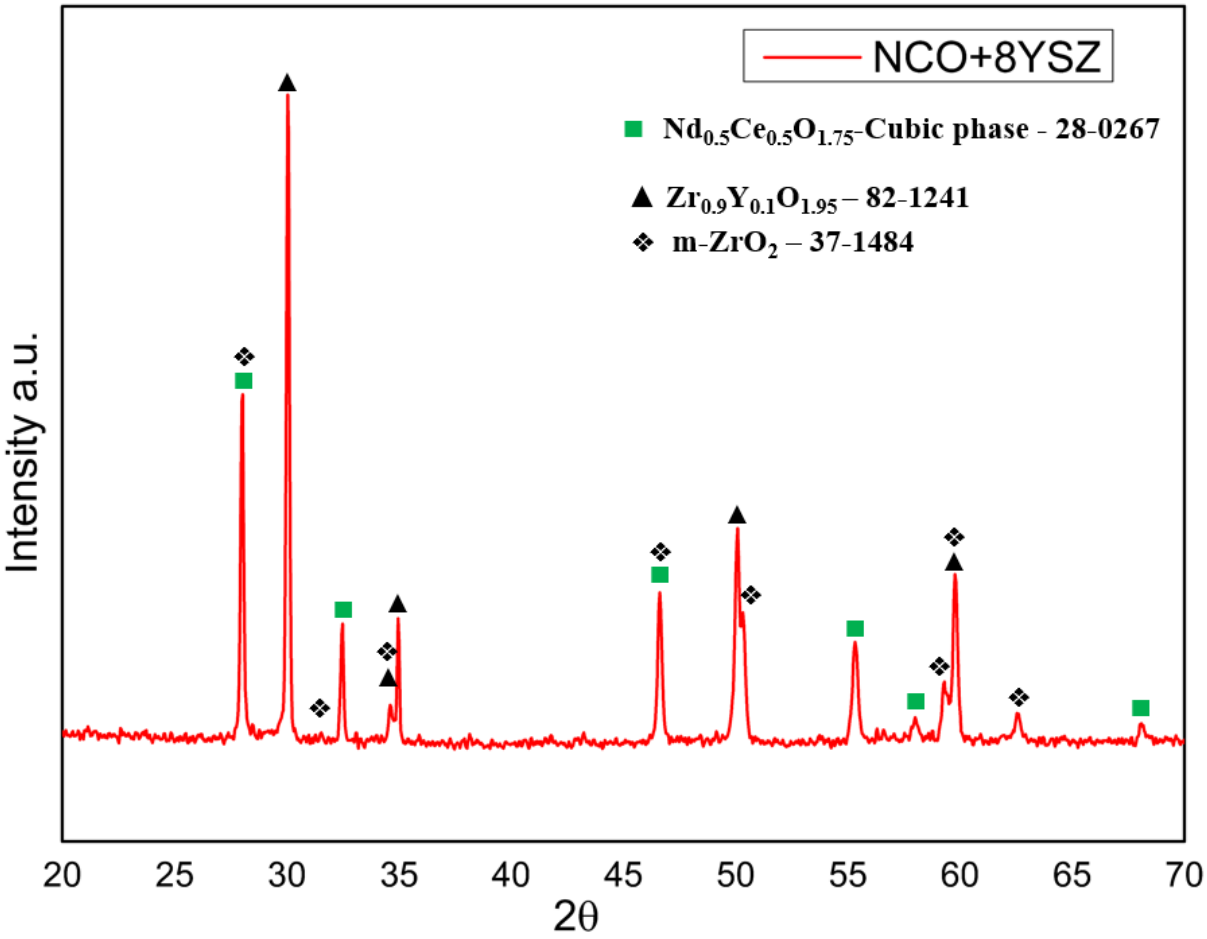

Figure 7.1: XRD pattern of the as-sprayed $Nd_2Ce_2O_7$ + 8YSZ composite thermal barrier coating

Fig 7.2 shows the surface and cross-sectional SEM micrographs of the as-sprayed $Nd_2Ce_2O_7$ + 8YSZ composite thermal barrier coating (TBC) deposited by the air plasma spraying (APS) process. The surface morphology **Fig 7.2(a, b)** reveals the characteristic lamellar splat-based structure formed during the rapid solidification of molten particles. There are regions of partial melting, intersplat pores, and a small number of unmelted particles that are evenly distributed throughout the coating, which are characteristic of APS-deposited ceramics. These

characteristics add to the poor thermal conductivity of the layer, which facilitates the scattering of phonons and heat resistance. The cross-sectional image **(Fig. 7 .2c)** displays a well-adhered multilayer architecture, consisting of the $Nd_2Ce_2O_7$ + 8YSZ topcoat, an intermediate NiCrAlY bond coat, and the Inconel 625 substrate. The upper layer has a dense lamellar structure, characterised by fine microcracks and interlamellar fractures, which help relieve thermal stresses when exposed to high temperatures. In general, the interface bonding and structural integrity of the coating are satisfactory, which demonstrates the effectiveness of the APS deposition procedure.

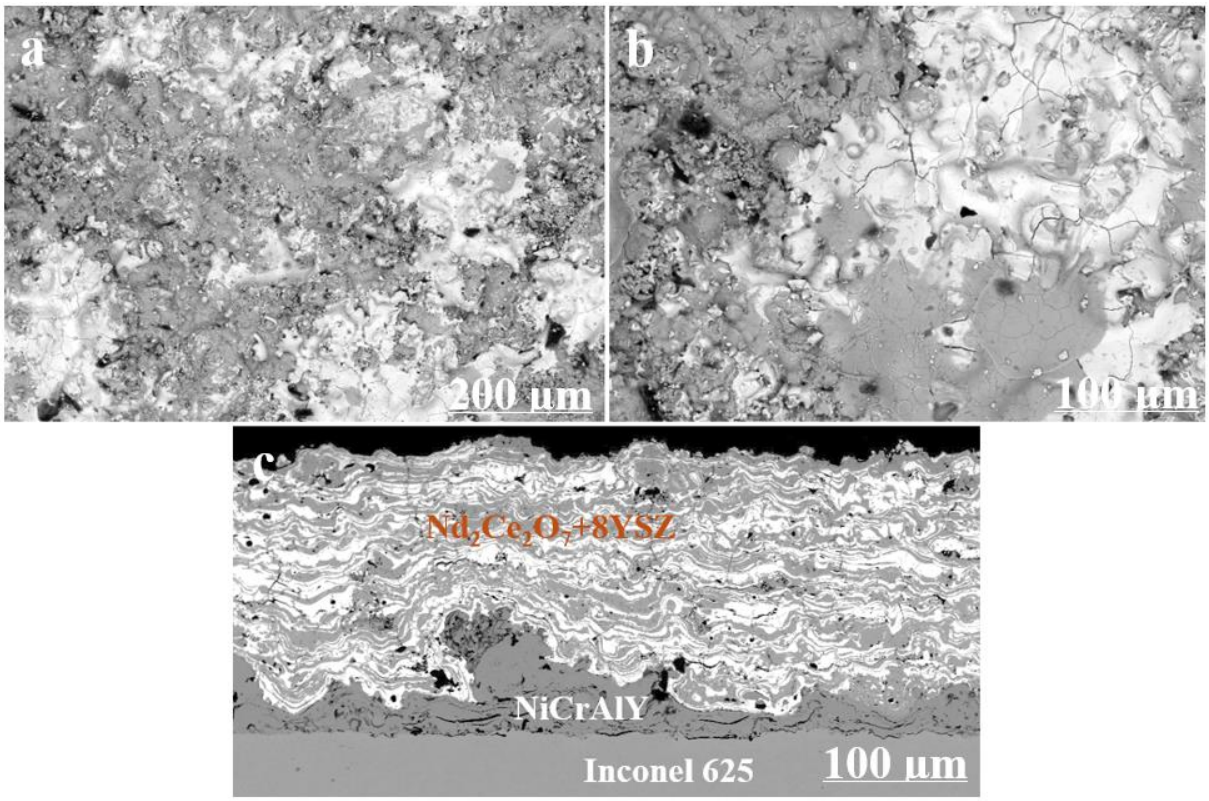

Figure 7.2: Surface and cross-sectional SEM views of the APS-deposited $Nd_2Ce_2O_7$ + 8YSZ coating.

7.3.3 Hot Corrosion Behavior of $Nd_2Ce_2O_7$ + 8YSZ Coating in Pure Na_2SO_4 Environment

Fig. 7.3 shows the XRD analysis of the $Nd_2Ce_2O_7$ + 8YSZ composite thermal barrier coating exposed to molten Na_2SO_4 at 920 °C for 168 h, which reveals that the major diffraction peaks correspond to the cubic fluorite phases of $Nd_{0.5}Ce_{0.5}O_{1.75}$ (JCPDS 28-0267) and cubic YSZ ($Zr_{0.9}Y_{0.1}O_{1.95}$, JCPDS 82-1241). The persistence of these strong cubic reflections indicates that both phases retained their crystallographic stability and resisted severe sulfate-induced

decomposition during prolonged exposure. In addition to these primary peaks, the appearance of weak reflections associated with $Nd_2O_2SO_4$ (JCPDS 48-1829) suggests the formation of neodymium oxysulphates as a secondary corrosion product. This phase originates from a surface-limited reaction between $Nd_2Ce_2O_7$ and molten Na_2SO_4, where Nd^{3+} ions react with sulfate species at the coating–salt interface.

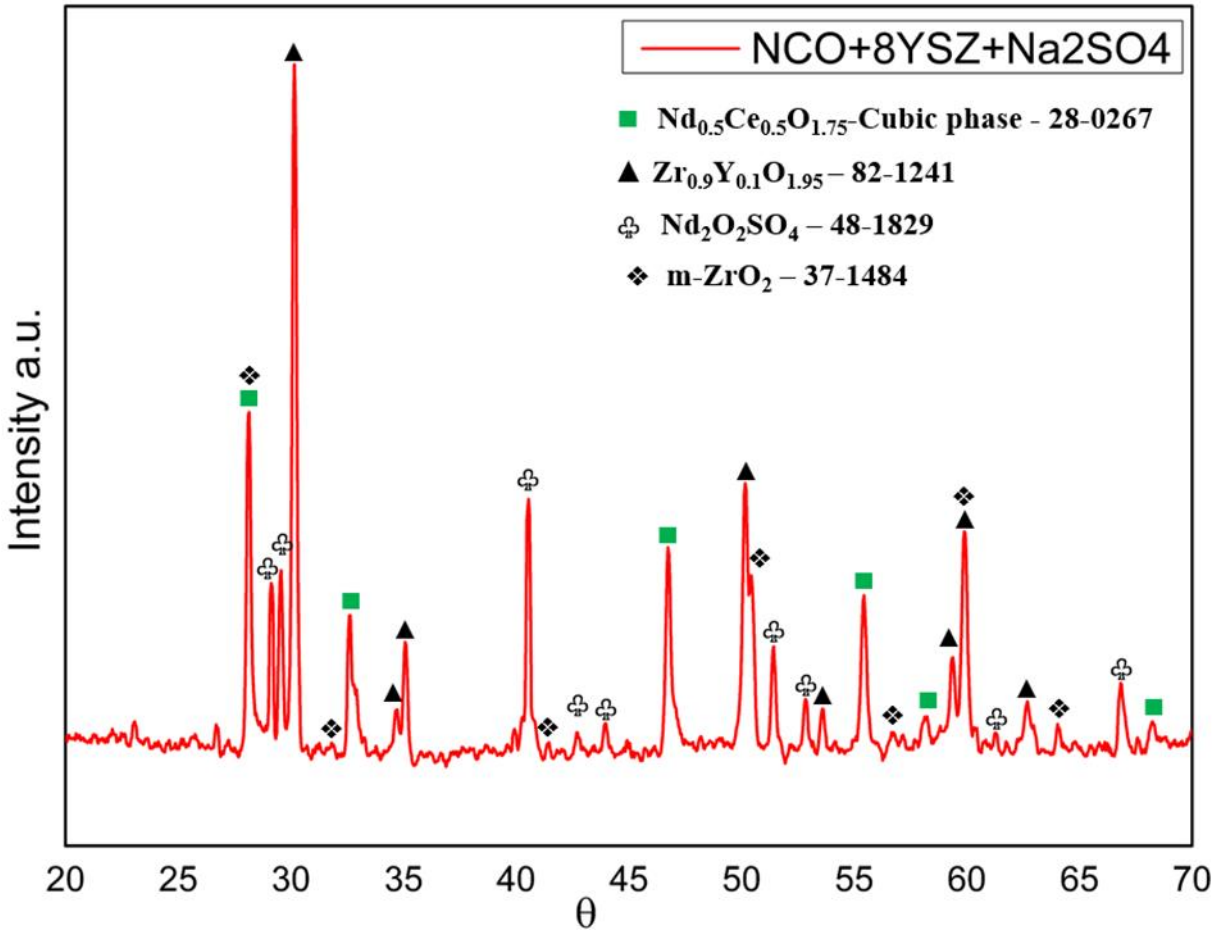

Figure 7.3: XRD pattern of the $Nd_2Ce_2O_7$ + 8YSZ coating after hot corrosion in molten Na_2SO_4 at 920 °C for 168 h.

A few minor peaks corresponding to monoclinic ZrO_2 (JCPDS 37-1484) were also identified, implying partial destabilisation of the YSZ component in localised regions due to Na^+ infiltration or thermal stresses during long-term exposure. The strength of these peaks, however, is of low magnitude, which indicates that the tetragonal cubic structure of YSZ remained intact mainly during the corrosion process. The coexistence of stable fluorite and YSZ phases, along with limited formation of $Nd_2O_2SO_4$ and negligible monoclinic transformation, demonstrates that the $Nd_2Ce_2O_7$ + 8YSZ composite coating exhibits high thermochemical stability and strong

resistance to sulfate attack. Overall, these findings suggest that the coating retains its structural integrity and effectively shields the underlying layers despite exposure to 168 hours at 920 °C in a pure Na_2SO_4 atmosphere.

The surface morphology and elemental distribution of the $Nd_2Ce_2O_7$ + 8YSZ composite TBC after 168 h exposure to molten Na_2SO_4 at 920 °C reveal distinct microstructural degradation features caused by sulfate attack. As shown in Figure **7.4(a–b),** the surface exhibits a dense accumulation of plate-like and flaky corrosion products, corresponding to a mixture of sulfate reaction compounds and partially degraded coating constituents. The uppermost region displays clusters of mixed $Nd_2Ce_2O_7$+ YSZ + sulfate phases, while certain localised zones are enriched with $Nd_2Ce_2O_7$-derived corrosion products, indicating preferential reaction of neodymium-containing regions with molten salt. The elongated and needle-like features observed correspond to Nd-rich oxysulphates crystals ($Nd_2O_2SO_4$), formed due to the interaction between $Nd_2Ce_2O_7$ and sulfate ions. High-magnification micrographs (**Figure 7.4b**) reveal regions rich in m-ZrO_2, indicating that localised tetragonal-to-monoclinic phase transformation of YSZ occurred during exposure. This transformation likely results from oxygen loss and cation diffusion induced by the corrosive sulfate melt. The corresponding EDS point analyses (Figure **7.4c** and table) confirm the chemical composition of the corroded surface. Points 1 and 2 show significant concentrations of O, S, Nd, and Ce, consistent with the formation of $Nd_2O_2SO_4$and residual $Nd_2Ce_2O_7$. The high S (6–10 at%) and Nd (15–19 at%) contents strongly support the formation of neodymium-based sulphates and oxysulphates as the dominant corrosion products in these regions. Point 3, in contrast, exhibits a high Zr (23.4 at%) and lower Nd content, suggesting areas dominated by ZrO_2 and YSZ remnants that were less affected by sulfate attack. The EDS elemental maps further substantiate these observations. The homogeneous oxygenation of the scanned area proves the oxidised character of the corrosion layer, and the concentration of sulphur in the separate clusters on the surface, as shown in the images of sulfate-rich deposits. The maps of Nd and Ce show strong co-localisation, indicating that these elements participate together in the formation of Nd, Ce, and sulphate compounds. The distribution of Zr is more dispersive, with localised enrichment areas related to the m-ZrO_2 regions in the SEM images. This segregation pattern demonstrates that YSZ underwent partial destabilisation, forming small monoclinic pockets amid the sulphate-rich layer.

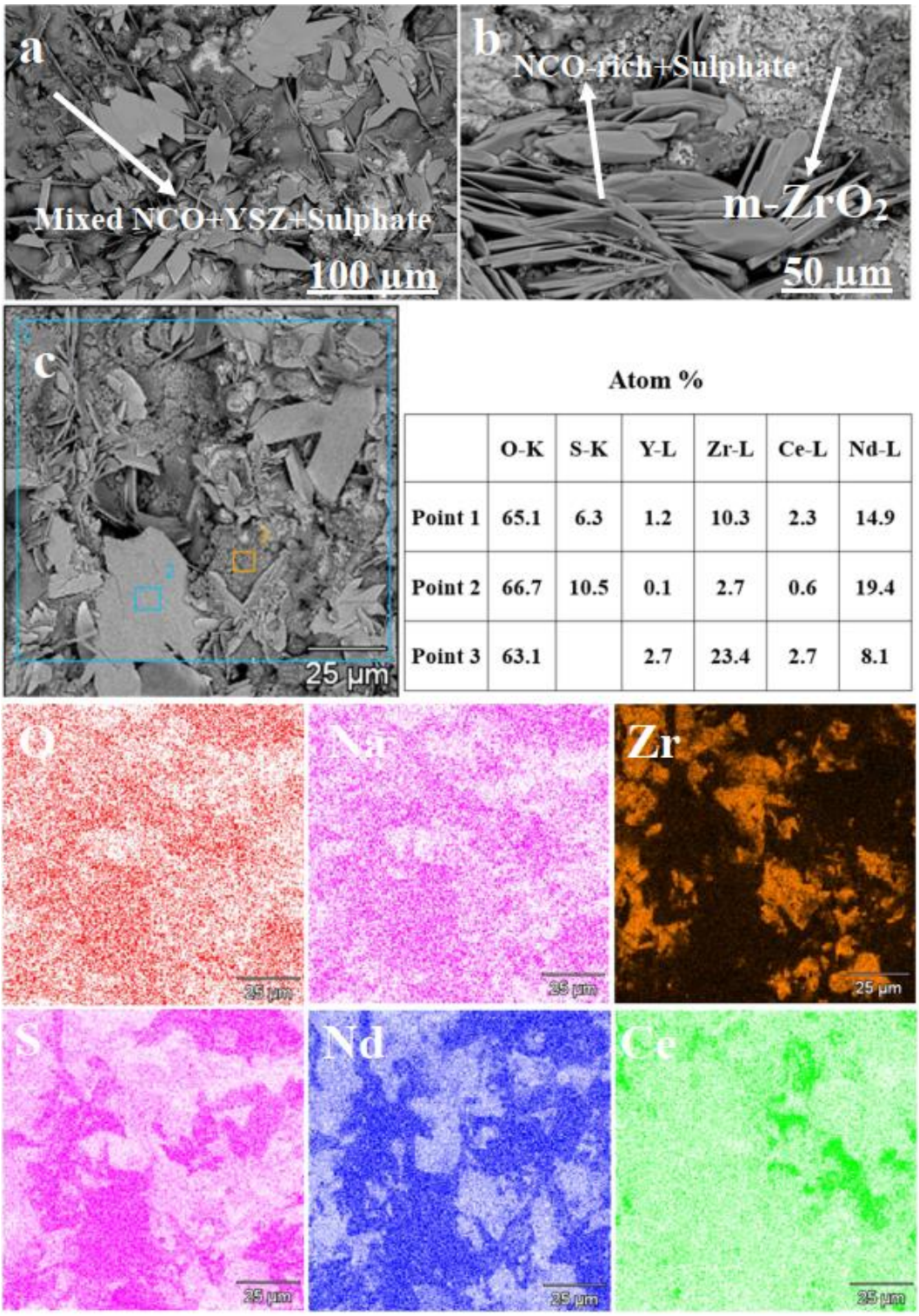

Atom %

	O-K	S-K	Y-L	Zr-L	Ce-L	Nd-L
Point 1	65.1	6.3	1.2	10.3	2.3	14.9
Point 2	66.7	10.5	0.1	2.7	0.6	19.4
Point 3	63.1		2.7	23.4	2.7	8.1

Figure 7.4: SEM and EDS analysis of the $Nd_2Ce_2O_7$ + 8YSZ coating after hot corrosion in molten Na_2SO_4 at 920 °C for 168 h.

In general, the analysis of the combined SEM and EDS indicates that the corrosion process in pure Na_2SO_4 occurs in two consecutive stages, where surface oxides are dissolved and a subsequent $Nd_2O_2SO_4$ scale is created, which partially covers the underlying material. The

$Nd_2Ce_2O_7$ component is primarily affected by the reaction, while YSZ remains relatively unaffected, experiencing only a slight structural change. The limited diffusion of sulphur into deeper layers and the retention of major fluorite and YSZ phases (as confirmed by XRD) indicate that the $Nd_2Ce_2O_7$ + 8YSZ composite TBC exhibits excellent resistance to sulfate-induced degradation. The presence of an Nd-rich sulfate layer as a chemical barrier limits additional inward attack, which underscores the viability of the composite structure in preventing long-term hot corrosion of thermal barrier coatings in the presence of Na_2SO_4.

Microstructural examination of the NCO-8YSZ TBC system subjected to corrosion in a liquid Na_2SO_4 salt environment, shown in **Figure 7.5(a-f).** Demonstrated the preservation of the overall integrity of the ceramic layer. No deep vertical and horizontal cracks were observed, and single vertical cracks penetrated the ceramic layer to a depth of approximately 50 μm. Areas of pore clusters are also visible, but these do not represent massive porosity. Examination of the coating microstructure reveals the presence of areas of varying colour, which, in the context of the BSE imaging method used, indicates the presence of at least three structural components. Chemical composition studies in microregions using EDS suggest the presence of parent phases: NCO (light) and 8YSZ (dark), as well as a grey phase, whose chemical composition indicates the mutual dissolution of both initial components. Based on the morphology of this phase, which is characterized by elongated and irregular strands, it can be inferred that it was formed during the plasma melting stage of the spraying process. Assessment of the interface between the NiCrAlY primer and the ceramic layer indicates the presence of a thin (approx. 1-2 μm) layer of TGO oxides.

Detailed microstructural examination of the individual structural components revealed the presence of interaction effects between the NCO and 8YSZ phases (excluding the NCO-8YSZ intermediate phase mentioned previously). In the dark areas corresponding to the 8YSZ phase, thin hairline microcracks filled with a light area are visible, suggesting the NCO phase has penetrated deeper into the 8YSZ. Analysis of the light regions corresponding to the NCO phase also revealed very fine voids (similar to those in the SZO+8YSZ and GZO+8YSZ systems), resulting from the initial stages of decomposition of the NCO phase into non-stoichiometric structures **[28,29]**.

Chemical composition studies did not reveal the presence of areas containing sulfur and sodium within the ceramic layer. Only on the surface of the ceramic layer were areas containing components derived from liquid sulfate salts located.

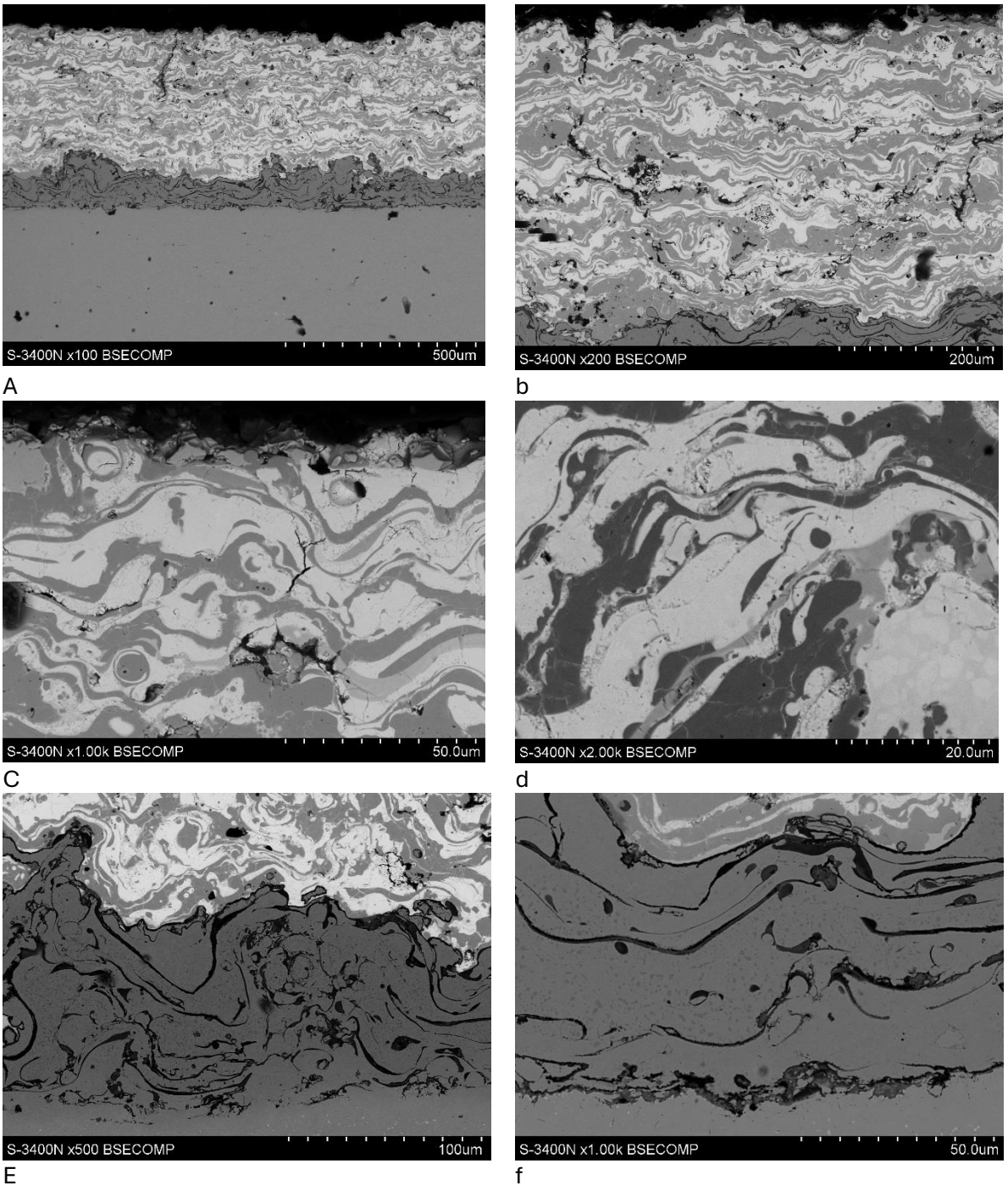

Figure 7.5: Cross-sectional SEM and EDS analysis of the $Nd_2Ce_2O_7$ + 8YSZ coating after hot corrosion in molten Na_2SO_4 at 920 °C for 168 h.

7.3.4 Hot Corrosion Behavior of $Nd_2Ce_2O_7$ + 8YSZ Coating in Equimolar Na_2SO_4–$MgSO_4$ Environment

Fig. 7.6 shows the XRD pattern of the $Nd_2Ce_2O_7$ + 8YSZ composite thermal barrier coating after exposure to a Na_2SO_4–$MgSO_4$ (1:1) molten salt mixture at 920 °C for 168 h. Compared with the coating exposed to pure Na_2SO_4, noticeable phase evolution is observed, indicating enhanced chemical interactions in the mixed-sulfate environment. The dominant diffraction peaks corresponding to cubic fluorite $Nd_{0.5}Ce_{0.5}O_{1.75}$ (JCPDS 28-0267) and cubic YSZ ($Zr_{0.9}Y_{0.1}O_{1.95}$, JCPDS 82-1241) remain clearly visible. This confirms that the primary coating phases maintain their crystalline integrity during prolonged high-temperature corrosion exposure, demonstrating good bulk phase stability of the composite system. In addition to the major phases, several low-intensity peaks are detected, which are indexed to Nd2O2SO4 (JCPDS 48-1829), monoclinic ZrO_2 (JCPDS 37-1484), and MgO (JCPDS 43-1102). The appearance of Nd2O2SO4 suggests that neodymium participates in sulfate-related reactions at the coating surface, leading to the formation of rare-earth oxysulphates compounds. The presence of monoclinic ZrO_2 indicates partial destabilization of the YSZ phase. However, the relatively weak intensity of these peaks suggests that this transformation is localized rather than representing complete bulk degradation of the coating.

Overall, the XRD analysis demonstrates that while the major cubic phases of $Nd_{0.5}Ce_{0.5}O_{1.75}$ and YSZ remain structurally stable, the Na_2SO_4–$MgSO_4$ molten salt environment promotes increased secondary phase formation. This reflects a higher degree of chemical interaction and corrosion activity at the coating surface compared to pure Na_2SO_4 exposure, highlighting the complex thermochemical behaviour induced by the mixed-sulfate system.

The surface morphology and elemental composition of the $Nd_2Ce_2O_7$ + 8YSZ composite thermal barrier coating after hot corrosion in a Na_2SO_4–$MgSO_4$ (1:1) molten salt environment at 920 °C for 168 h show pronounced changes compared with pure Na_2SO_4 exposure. As observed in **Fig. 7.7(a)** and **(b)**, the surface is extensively covered with compact and partially sintered corrosion products, displaying a rough and uneven appearance with visible reaction layers. Fine grained deposits and numerous platelet like structures are present across the surface, indicating the formation of mixed oxide and sulfate compounds. This altered morphology suggests that the addition of $MgSO_4$ does not suppress corrosion but instead promotes more intense chemical reactions and stronger molten salt attack.

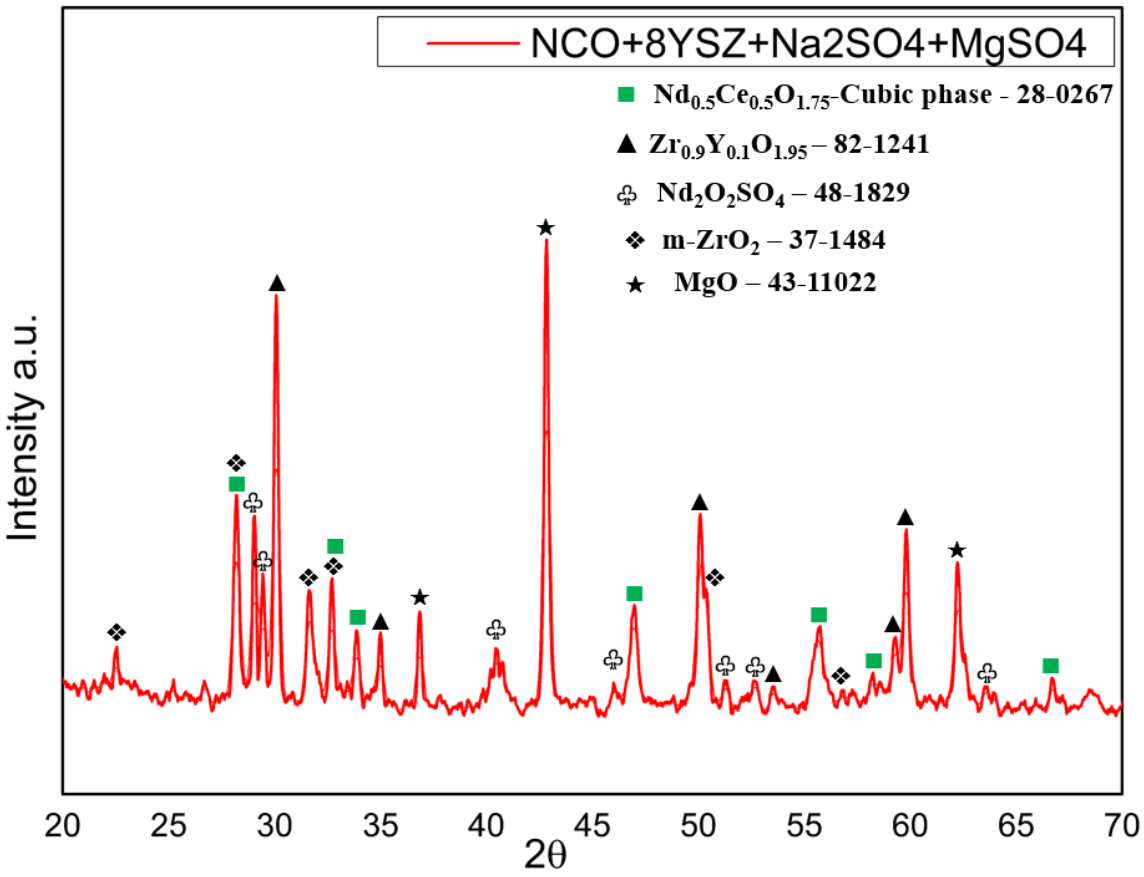

Figure 7.6: XRD pattern of the $Nd_2Ce_2O_7$+ 8YSZ coating after hot corrosion in an equimolar Na_2SO_4–$MgSO_4$ mixture at 920 °C for 168 h.

The high magnification micrograph in Figure 7.7(c) reveals distinct Mg rich zones together with Nd–Ce–S containing regions, confirming the formation of MgO and rare earth oxysulphates. EDS analysis identifies oxygen, magnesium, sulphur, neodymium, and cerium as the dominant elements on the corroded surface, demonstrating extensive surface reactions and compound formation. The high oxygen and magnesium signals indicate the thermal decomposition of $MgSO_4$ into MgO, which contributes to the buildup of thick reaction layers rather than providing effective protection. Unlike the pure Na_2SO_4 case, sulphur is detected in multiple surface regions, suggesting deeper penetration of sulfate species.

Elemental mapping further supports these observations. Oxygen and magnesium maps show strong overlap, confirming the widespread presence of MgO across the coating surface. Sulphur distribution is relatively broad, indicating continuous sulfate related reactions rather than isolated patches. The zirconium map confirms that YSZ is still present; however, localized destabilization is evident near reaction zones. Cerium and neodymium maps show strong co-

localization with sulphur rich areas, indicating their active involvement in sulfate reactions. Overall, the mixed sulfate environment.

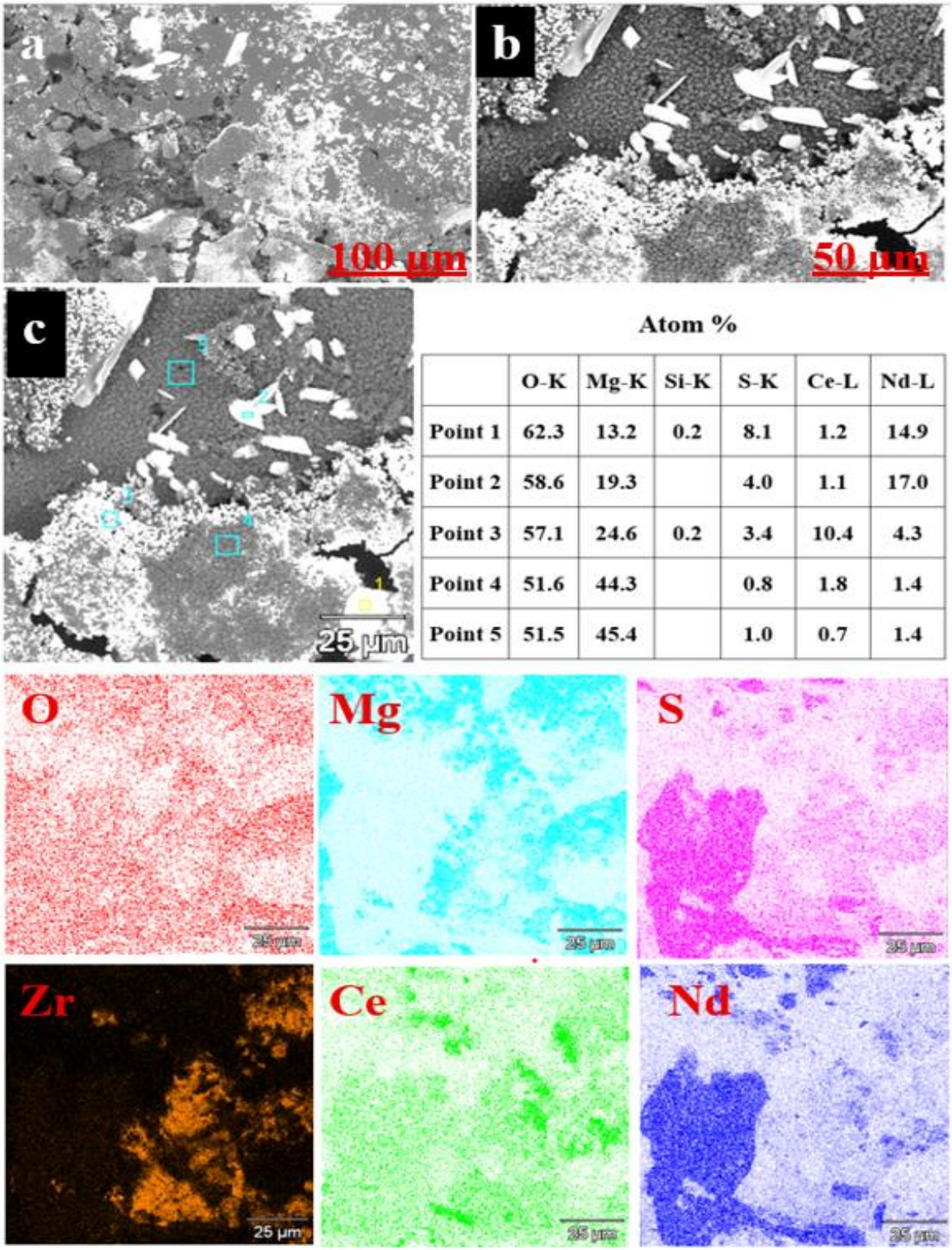

Atom %

	O-K	Mg-K	Si-K	S-K	Ce-L	Nd-L
Point 1	62.3	13.2	0.2	8.1	1.2	14.9
Point 2	58.6	19.3		4.0	1.1	17.0
Point 3	57.1	24.6	0.2	3.4	10.4	4.3
Point 4	51.6	44.3		0.8	1.8	1.4
Point 5	51.5	45.4		1.0	0.7	1.4

Figure 7.7: SEM and EDS analysis of the $Nd_2Ce_2O_7$+ 8YSZ coating after hot corrosion in an equimolar Na_2SO_4–$MgSO_4$ mixture at 920 °C for 168 h.

Overall, the SEM and EDS analyses indicate that the addition of $MgSO_4$ does not suppress corrosion but instead enhances chemical interactions between the molten salt and the coating. The formation of MgO contributes to the development of thick reaction layers however, these layers are non-protective and allow continued sulphur transport, leading to intensified molten salt attack and increased surface degradation compared with pure Na_2SO_4 exposure. The $Nd_2Ce_2O_7$ + 8YSZ coating retains overall structural integrity under Na_2SO_4–$MgSO_4$ exposure; however, the extent of surface degradation and reaction product formation is greater than that observed in pure Na_2SO_4, indicating increased corrosion severity in the mixed sulfate environment.

From a microstructural perspective, the NCO+8YSZ TBC system corroded in a mixture of Na_2SO_4 and $MgSO_4$ sulfate salts is very similar to the TBC system corroded solely in liquid Na_2SO_4 salt, as illustrated in **Figure 7.8 (a-f)**. As in the previous case, the coating integrity was maintained. No vertical or horizontal cracks were observed. As before, three basic structural components were identified: NCO (light), 8YSZ (dark), and NCO+8YSZ (grey), with the same morphology as before. Similar microstructural effects associated with the degradation process were also identified, with a clearly higher intensity of these processes. This is particularly concerning the presence of very fine voids within the NCO phase, as well as hairline cracks in the 8YSZ phase, which are filled with light areas (like NCO). The increased severity of such processes is due to the lower melting temperature of the sodium and magnesium salt mixture than that of pure sodium salt **[30]**. This must result in a lower viscosity of the liquid sulfate mixture, which facilitates the penetration of this agent through the network of voids in the ceramic layer. This likely results in a thicker TGO zone, reaching approximately 4 μm in thickness.

Chemical composition analysis using EDS revealed the presence of magnesium and sulfur within the ceramic layer, but the presence of sodium could not be identified.

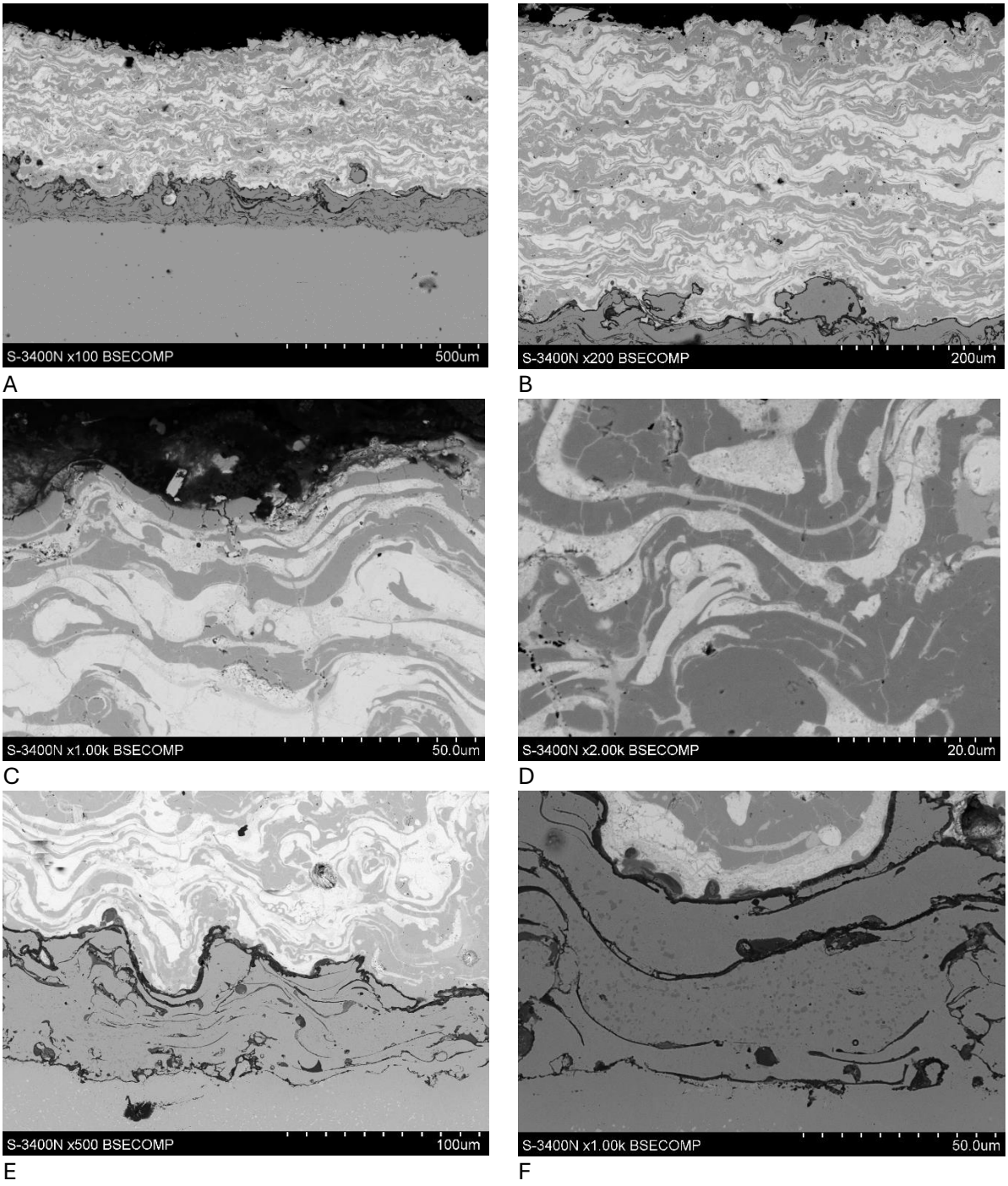

Figure 7.8: Cross-sectional SEM and EDS analysis of the $Nd_2Ce_2O_7$ + 8YSZ coating after hot corrosion in an equimolar Na_2SO_4–$MgSO_4$ mixture at 920 °C for 168 h.

7.3.5 Hot Corrosion Behavior of $Nd_2Ce_2O_7$ + 8YSZ Coating in Equimolar Na_2SO_4–V_2O_5 Environment

Fig. 7.9 presents the X-ray diffraction (XRD) analysis of a $Nd_2Ce_2O_7$ + 8YSZ composite coating subjected to hot corrosion in equimolar amounts of Na_2SO_4 and V_2O_5 at 920°C for 48 hours. The XRD peaks indicate the formation of several phases resulting from the reaction between the composite coating and corrosive salts at elevated temperatures. The primary phases identified are $NdVO_4$, $Ce_{0.2}Y_{0.79}O_{1.6}$, m-ZrO_2, and $Nd_{0.4}Ce_{0.6}O_{1.8}$.

The $NdVO_4$ (neodymium vanadate) phase forms as a result of the interaction between neodymium oxide (Nd_2O_3) from the neodymium cerate and vanadium pentoxide (V_2O_5) from the corrosive salts. The reaction proceeds as follows **[31,32]**:

$$Na_2SO_4 \rightarrow Na_2O + SO_3 \quad (1)$$

$$Na_2O + V_2O_5 \rightarrow 2NaVO_3 \quad (2)$$

$$Nd_2Ce_2O_7 + 4NaVO_3 \rightarrow 2NdVO_4 + CeVO_4 + 2Na_2O + \frac{3}{2}O_3 \quad (3)$$

The $Ce_{0.2}Y_{0.79}O_{1.6}$ (cerium-yttrium oxide) phase appears as a mixed oxide of cerium and yttrium, which likely forms due to the interaction between cerium and yttrium oxides in the YSZ matrix with the corrosive salts.

The $Nd_{0.4}Ce_{0.6}O_{1.8}$ (neodymium cerium oxide, PDF 75-0155) phase forms as a result of the transformation of the initial $Nd_{0.5}Ce_{0.5}O_{1.75}$ (neodymium cerium oxide, JCPDS 28-0267) phase, which is a cubic fluorite structure, into a more modified composition under the hot corrosion conditions. This change reflects the interaction of neodymium cerate with the corrosive salts, leading to a shift in the stoichiometry and the incorporation of more cerium. These results confirm the transformation and formation of various phases in the $Nd_2Ce_2O_7$ + 8YSZ composite coating as a result of the hot corrosion process in the sulfate-vanadate environment at high temperatures.

Figure 7.10 presents the SEM and EDS analysis of the $Nd_2Ce_2O_7$ + 8YSZ composite thermal barrier coating (TBC) after exposure to hot corrosion in a Na_2SO_4+V_2O_5 mixture at 920°C for 48 hours. In **Fig. 7.10 (a)**, the surface morphology of the coating is shown, revealing the presence of monoclinic m-ZrO_2. This phase transformation occurs due to the exposure of zirconia to an aggressive, corrosive environment, where tetragonal zirconia (t-ZrO_2) converts to monoclinic zirconia (m-ZrO_2), a well-known response to corrosive conditions at high temperatures. The morphology includes rectangular and angular-shaped crystals, reflecting this phase change. In **Fig. 7.10 (b)**, the image zooms in on the $NdVO_4$ crystals, which appear as

elongated and needle-like structures. The formation of these crystals is due to the aggressive environment of corrosion formed by the interaction of the Na_2SO_4+V_2O_5 mixture and neodymium cerate phase ($Nd_2Ce_2O_7$) present in the coating. The corrosive environment enhances the disintegration of $Nd_2Ce_2O_7$, resulting in the production of $NdVO_4$, a major degradation product during the aggressive interaction. The existence of $NdVO_4$ in this manner is therefore an indicator of the corrosive salts disintegrating the neodymium cerate phase **[33]**.

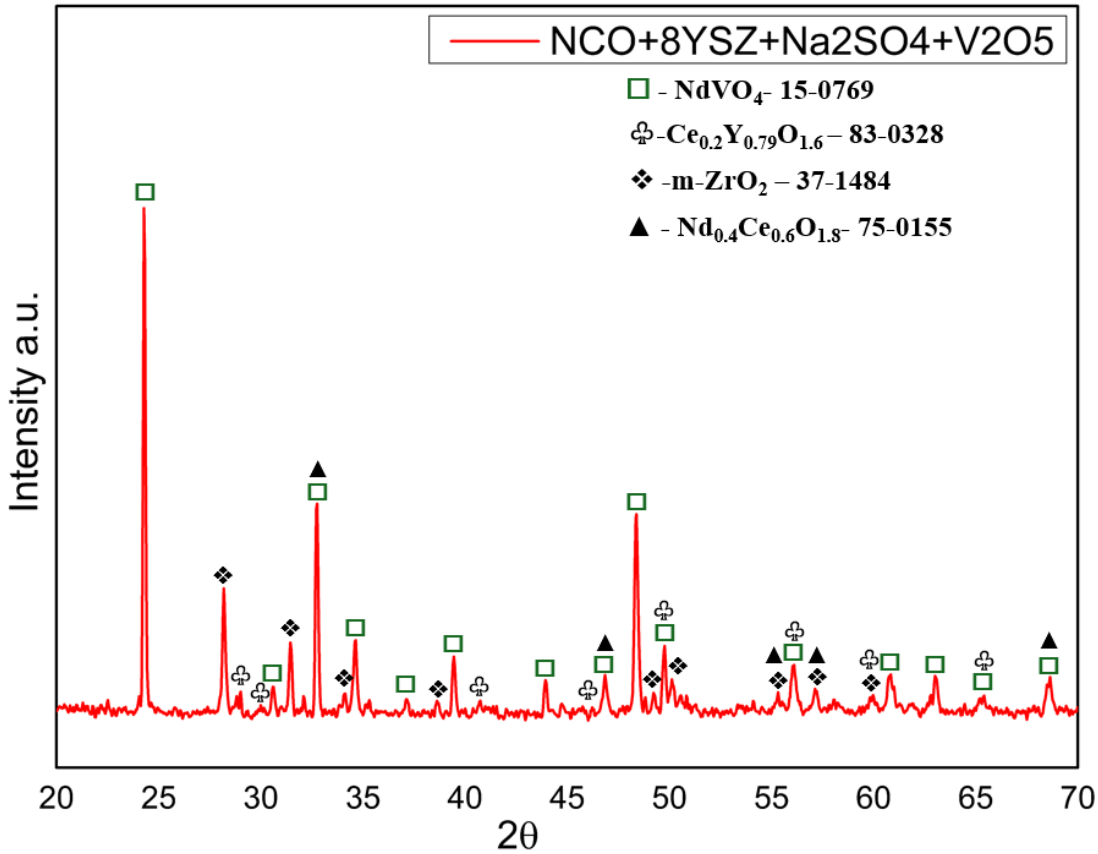

Figure 7.9: XRD pattern of the $Nd_2Ce_2O_7$+ 8YSZ coating after hot corrosion in an equimolar Na_2SO_4–V_2O_5 mixture at 920 °C for 48 h.

Fig. 7.10(c) provides a detailed elemental composition from EDS analysis, with data from six different points on the surface, as shown in the table. The atomic percentages of elements that include oxygen (O), sodium (Na), aluminium (Al), sulphur (S), vanadium (V), yttrium (Y), zirconium (Zr), cerium (Ce) and neodymium (Nd) are given, indicating the distribution of the elements in the coating. The fact that the oxygen content is high and the contents of sodium, vanadium, zirconium, cerium, and neodymium are different indicates that the corrosion products are a mixture of oxide and vanadate. The elemental maps at the bottom show the distribution of these key elements, confirming that cerium and vanadium are concentrated in

the corrosion products, with $NdVO_4$ being a primary product formed during the interaction with the corrosive environment.

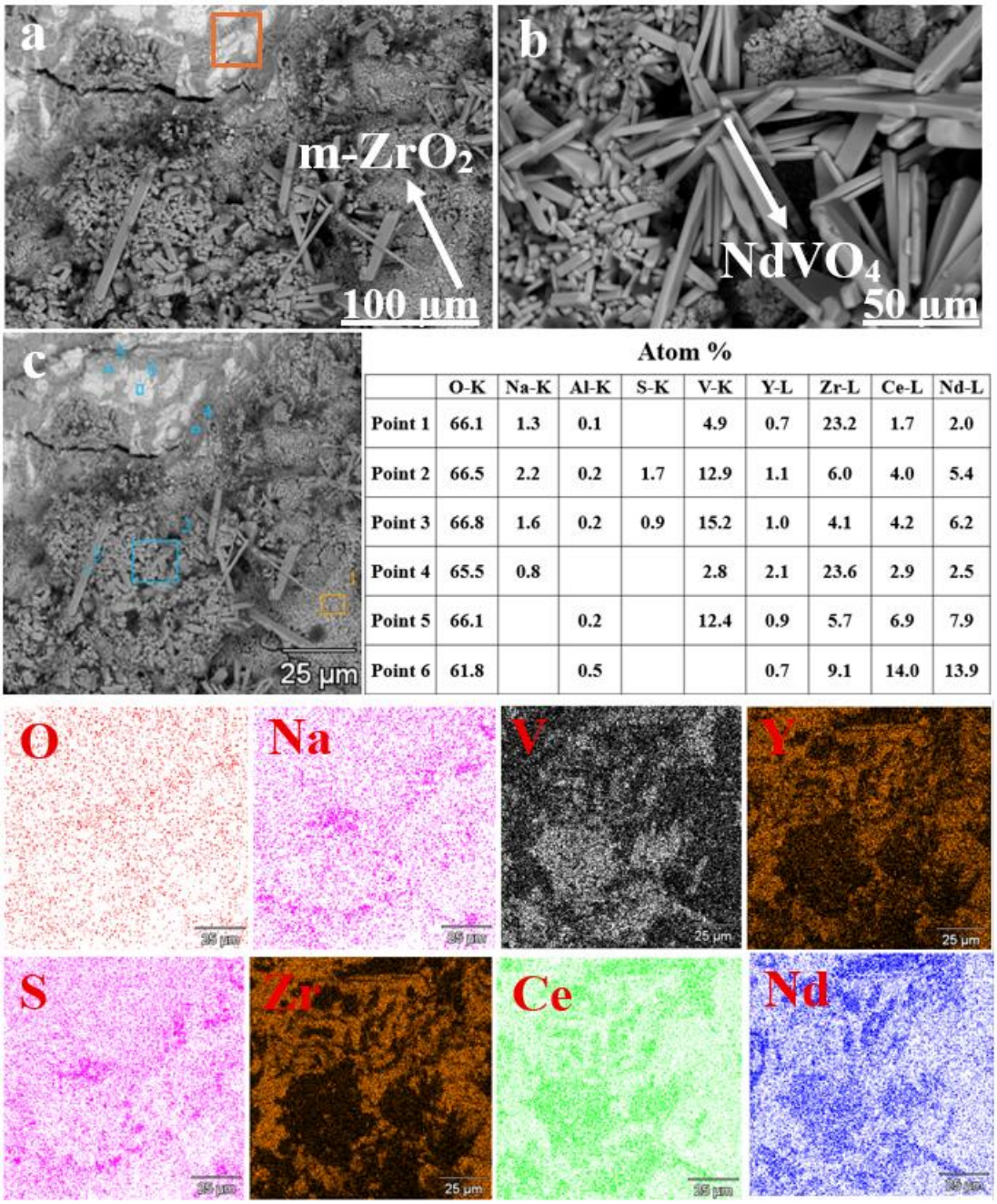

Atom %

	O-K	Na-K	Al-K	S-K	V-K	Y-L	Zr-L	Ce-L	Nd-L
Point 1	66.1	1.3	0.1		4.9	0.7	23.2	1.7	2.0
Point 2	66.5	2.2	0.2	1.7	12.9	1.1	6.0	4.0	5.4
Point 3	66.8	1.6	0.2	0.9	15.2	1.0	4.1	4.2	6.2
Point 4	65.5	0.8			2.8	2.1	23.6	2.9	2.5
Point 5	66.1		0.2		12.4	0.9	5.7	6.9	7.9
Point 6	61.8		0.5			0.7	9.1	14.0	13.9

Figure 7.10: SEM and EDS analysis of the $Nd_2Ce_2O_7$+ 8YSZ coating after hot corrosion in an equimolar Na_2SO_4–V_2O_5 mixture at 920 °C for 48 h.

In summary, **Fig. 7.10 (a-c)** illustrates the significant degradation of the $Nd_2Ce_2O_7$+ 8YSZ composite coating due to the aggressive sulfate-vanadate corrosion environment. The SEM and EDS analysis reveal the formation of m-ZrO_2 and $NdVO_4$, with detailed insights into the elemental composition and distribution of the corrosion products. These findings attest to the corrosiveness of the Na_2SO_4+V_2O_5 mixture, which enhances the degradation of the TBC and

emphasises the importance of the aggressive corrosion environment in the degradation of TBCs at high temperatures.

7.4 Conclusion

The microstructural studies conducted, along with those characterising the behaviour of the TBC coating system type 50 $Nd_2Ce_2O_7$ + 50 8YSZ, under the conditions of sulphate salts in the presence of vanadium oxide, revealed the following:

- The $Nd_2Ce_2O_7$ + 8YSZ composite thermal barrier coating retained a stable dual-phase structure composed of cubic fluorite $Nd_2Ce_2O_7$ and cubic YSZ, demonstrating good phase compatibility after high-temperature exposure.
- In the pure Na_2SO_4 environment, the coating showed relatively mild degradation, with limited formation of $Nd_2O_2SO_4$ and minor monoclinic ZrO_2, indicating good resistance to sulphate attack.
- In the Na_2SO_4–$MgSO_4$ molten salt environment, more pronounced surface reactions were observed, with extensive formation of reaction products and increased sulphur penetration, indicating that the addition of $MgSO_4$ intensified chemical interactions and enhanced molten salt corrosion rather than suppressing it.
- Exposure to the Na_2SO_4–V_2O_5 environment caused severe coating degradation, characterized by the formation of $NdVO_4$ and monoclinic ZrO_2, extensive surface damage, and increased porosity due to aggressive vanadate attack.
- SEM–EDS analysis confirmed that corrosion reactions predominantly affected the $Nd_2Ce_2O_7$ phase, while the YSZ phase exhibited comparatively higher chemical stability and contributed to partial retention of coating integrity.
- The coating substrate interface remained well bonded under all corrosion conditions, with only a thin thermally grown oxide (TGO) layer observed, indicating good adhesion and thermal compatibility of the multilayer system.

Reference

[1] S. M. Naga, M. Awaad, H. F. El-Maghraby, A. M. Hassan, M. Elhoriny, A. Killinger, *et al.*, "Effect of La2Zr2O7 coat on the hot corrosion of multi-layer thermal barrier coatings," *Mater. Des.*, vol. 102, pp. 1–7, 2016.

[2] Z.-G. Liu, W.-H. Zhang, J.-H. Ouyang, and Y. Zhou, "No vel double-ceramic-layer (La0.8Eu0.2)2Zr2O7/YSZ thermal barrier coatings deposited by plasma spraying," *Ceram. Int.*, vol. 40, pp. 11277–11282, 2014.

[3] Z.-G. Liu, W.-H. Zhang, J.-H. Ouyang, and Y. Zhou, "Novel thermal barrier coatings based on rare-earth zirconates/YSZ double-ceramic-layer system deposited by plasma spraying," *J. Alloy Compd.*, vol. 647, pp. 438–444, 2015.

[4] A. H. Pakseresht, A. H. Javadi, E. Ghasali, A. Shahbazkhan, and S. Shakhesi, "Evaluation of hot corrosion behavior of plasma-sprayed thermal barrier coatings with graded intermediate layer and double ceramic top layer," *Surf. Coat. Technol.*, vol. 288, pp. 36–45, 2016.

[5] Z. Xu, L. He, R. Mu, and Z. Xin, "(Y0.05La0.95)2(Zr0.7Ce0.3)2O7 ceramics as a thermal barrier coating material for high-temperature applications," *Mater. Lett.*, vol. 116, pp. 182–184, 2014.

[6] G. Di Girolamo, C. Blasi, L. Pagnotta, and M. Schioppa, "Phase evolution and thermophysical properties of plasma-sprayed thick zirconia coatings after annealing," *Ceram. Int.*, vol. 36, pp. 2273–2280, 2010.

[7] X. Q. Cao, R. Vassen, and D. Stoever, "Ceramic materials for thermal barrier coatings," *J. Eur. Ceram. Soc.*, vol. 24, pp. 1–10, 2004.

[8] M. R. Loghman-Estarki, R. Shoja Razavi, H. Edris, S. R. Bakhshi, M. Nejati, and H. Jamali, "Comparison of hot corrosion behavior of nanostructured ScYSZ and YSZ thermal barrier coatings," *Ceram. Int.*, vol. 42, pp. 7432–7439, 2016.

[9] M. R. Loghman-Estarki, M. Nejati, H. Edris, R. S. Razavi, H. Jamali, and A. H. Pakseresht, "Evaluation of hot corrosion behavior of plasma-sprayed scandia and yttria co-stabilized nanostructured thermal barrier coatings in the presence of molten sulfate and vanadate salt," *J. Eur. Ceram. Soc.*, vol. 35, pp. 693–702, 2015.

[10] W. Ma, D. E. Mack, R. Vaßen, and D. Stöver, "Perovskite-type strontium zirconate as a new material for thermal barrier coatings," *J. Am. Ceram. Soc.*, vol. 91, pp. 2630–2635, 2008.

[11] W. Ma, M. O. Jarligo, D. E. Mack, D. Pitzer, J. Malzbender, R. Vaßen, *et al.*, "New generation perovskite thermal barrier coating materials," *J. Therm. Spray Technol.*, vol. 17, pp. 831–837, 2008.

[12] J. Yu, H. Zhao, S. Tao, X. Zhou, and C. Ding, "Thermal conductivity of plasma-sprayed $Sm_2Zr_2O_7$ coatings," *J. Eur. Ceram. Soc.*, vol. 30, pp. 799–804, 2010.

[13] R. Gadow and M. Lischka, "Lanthanum hexaaluminate—novel thermal barrier coatings for gas turbine applications—materials and process development," *Surf. Coat. Technol.*, vol. 151, pp. 392–399, 2002.

[14] X. Wang, L. Guo, H. Zhang, S. Gong, and H. Guo, “Structural evolution and thermal conductivities of (Gd1-xYbx)2Zr2O7 (x = 0–0.1) ceramics for thermal barrier coatings,” *Ceram. Int.*, vol. 41, pp. 12621–12625, 2015.

[15] N. Schlegel, D. Sebold, Y. J. Sohn, G. Mauer, and R. Vaßen, “Cycling performance of a columnar-structured complex perovskite in a temperature gradient test,” *J. Therm. Spray Technol.*, vol. 24, pp. 1205–1212, 2015.

[16] M. Li, L. Guo, and F. Ye, “Phase structure and thermal conductivities of Er2O3-stabilized ZrO_2-toughened Gd2Zr2O7 ceramics for thermal barrier coatings,” *Ceram. Int.*, vol. 42, pp. 16584–16588, 2016.

[17] T. Liu, X. Chen, G.-J. Yang, and C.-J. Li, “Properties evolution of plasma-sprayed La2Zr2O7 coating induced by pore structure evolution during thermal exposure,” *Ceram. Int.*, vol. 42, pp. 15485–15492, 2016.

[18] S. Mahade, N. Curry, S. Björklund, N. Markocsan, and P. Nylén, “Failure analysis of $Gd_2Zr_2O_7$/YSZ multi-layered thermal barrier coatings subjected to thermal cyclic fatigue,” *J. Alloy Compd.*, vol. 689, pp. 1011–1019, 2016.

[19] B. Paul, K. Singh, T. Jaroń, A. Roy, and A. Chowdhury, “Structural properties and the fluorite–pyrochlore phase transition in La2Zr2O7: the role of oxygen to induce local disordered states,” *J. Alloy Compd.*, vol. 686, pp. 130–136, 2016.

[20] Z. Xiaofeng, C. Xiangzhong, X. Min, B. Jinxiao, S. Xiwen, and A. Shengli, “Evolution of microstructure and cyclic life of La2(Ce0.3Zr0.7)2O7–3 wt.% Y2O3 coatings,” *Surf. Coat. Technol.*, vol. 307, pp. 951–956, 2016.

[21] C. Xiaoge, T. An, Z. Hongsong, L. Yanxu, Z. Haoming, and Z. Yongde, “Thermal conductivity and expansion coefficient of Ln2LaTaO7 (Ln = Er and Yb) oxides for thermal barrier coating applications,” *Ceram. Int.*, vol. 42, pp. 15749–15754, 2016.

[22] D. Zhang, Z. Zhao, B. Wang, S. Li, and J. Zhang, “Investigation of a new type of composite ceramics for thermal barrier coatings,” Mater. Des., vol. 112, pp. 27–33, 2016.

[23] H.-F. Liu, X. Xiong, X.-B. Li, and Y.-L. Wang, “Hot corrosion behavior of Sc2O3–Y2O3–ZrO2 thermal barrier coatings in presence of Na_2SO_4 + V_2O_5 molten salt,” Corros. Sci., vol. 85, pp. 87–93, 2014.

[24] H. Z. Hongsong, J. Li, G. Li, Z. Zheng, and X. Wang, “Investigation about thermophysical properties of Ln2Ce2O7 (Ln = Sm, Er, and Yb) oxides for thermal barrier coatings,” Mater. Res. Bull., vol. 47, pp. 4181–4186, 2012.

[25] X. Q. Cao, R. Vassen, W. Jungen, S. Schwartz, F. Tietz, and D. Stöver, “Thermal stability of lanthanum zirconate plasma-sprayed coating,” J. Am. Ceram. Soc., vol. 84, pp. 2086–2090, 2001.

[26] F. Zhang, C. Tracy, M. Lang, and R. C. Ewing, “Stability of fluorite-type La2Ce2O7 under extreme conditions,” J. Alloy Compd., vol. 674, pp. 168–173, 2016.

[27] H. Zhang, S. Liao, X. Dang, S. Guan, and Z. Zhang, “Preparation and thermal conductivities of Gd2Ce2O7 and (Gd0.9Ca0.1)2Ce2O6.9 ceramics for thermal barrier coatings,” J. Alloy Compd., vol. 509, pp. 1226–1230, 2011.

[28] G. Moskal, S. Jucha, M. Mikuśkiewicz, D. Migas, and A. Jasik, “Atypical decomposition processes of Sm2Zr2O7 + 8YSZ dual-phase TBCs during hot corrosion,” *Corros. Sci.*, vol. 170, no. December 2019, p. 108681, 2020, doi: 10.1016/j.corsci.2020.108681.

[29] A. Iqbal, G. Moskal, and B. Witala, “Degradation mechanism of dual-phase thermal barrier coatings Gd2Zr2O7 + 8YSZ under hot corrosion in pure Na2SO4,” *J. Therm. Anal. Calorim.*, vol. 150, no. 1, pp. 151–165, 2025, doi: 10.1007/s10973-024-13784-3.

[30] H. Du, “Thermodynamic assessment of the K2SO4–Na2SO4–MgSO4–CaSO4 system,” *Journal of Phase Equilibria*, vol. 21, Feb. 2000, doi: 10.1361/105497100770340363.

[31] K. P. Jonnalagadda *et al.*, “Hot Corrosion Mechanism in Multi-Layer Suspension Plasma Sprayed Gd2Zr2O7 /YSZ Thermal Barrier Coatings in the Presence of V2O5 + Na2SO4,” *J. Therm. Spray Technol.*, vol. 26, no. 1–2, pp. 140–149, 2017, doi: 10.1007/s11666-016-0486-5.

[32] P. G. Lashmi, P. V. Ananthapadmanabhan, Y. Chakravarthy, G. Unnikrishnan, N. Balaji, and S. T. Aruna, “Hot corrosion studies on plasma sprayed bi-layered YSZ/La2Ce2O7 thermal barrier coating fabricated from synthesized powders,” *J. Alloys Compd.*, vol. 711, pp. 355–364, 2017, doi: 10.1016/j.jallcom.2017.04.022.

[33] N. Ejaz, L. Ali, A. Ahmed, A. Rafiq, G. H. Awan, and K. Mehmood, “Sulfate-vanadate hot corrosion of neodymium cerate/yttria stabilized zirconia composite coating,” *Int. J. Appl. Ceram. Technol.*, vol. 16, no. 3, pp. 931–942, 2019, doi: 10.1111/ijac.13143.

Chapter 8: Conclusion and future work

8.1 Conclusion

Single-phase thermal barrier coating systems based on neodymium zirconate demonstrate excellent resistance to the corrosive effects of environments containing liquid sulfate salt deposits, both Na_2SO_4 and $Na_2SO_4/MgSO_4$ mixtures.

The primary degradation mechanism of $Nd_2Zr_2O_7$ TBC coatings is related to their high susceptibility to temperature and environmentally induced microcracks, as well as aggressive corrosive environments. The presence of microcracks and a high Young's modulus favours the generation of unfavorable stress states, resulting in ceramic layer spallation.

This indicates the need to increase the deformation tolerance (fracture toughness) of the ceramic layer, which should ensure increased operational durability in aggressive sulfate salt environments. The two-phase composite coatings of the $Nd_2Zr_2O_7$ + 8YSZ and $Nd_2Ce_2O_7$ + 8YSZ types demonstrated not only very favorable behaviour under the influence of liquid sulfate salts and their mixtures, but also maintained the overall integrity of the coating despite the formation of voids and microcracks in the ceramic layer's microstructure. This is due to the increased tolerance to deformation of the two-phase microstructure of the TBC coating.

Corrosion degradation processes in the tested TBC systems were associated with the interaction of liquid sulfate salts with neodymium zirconate or cerate, and the formation of neodymium sulfates or oxysulphates as primary corrosion products (to a limited extent).

The dominating second identified mechanism was the decomposition of neodymium zirconate with a pyrochlore lattice into non-stoichiometric zirconates with a fluorite lattice. In the case of neodymium cerate, the formation of non-stoichiometric compounds was observed only during corrosion in a mixture of liquid sodium and magnesium sulfate salts. The generation of numerous voids within the zirconate and cerate phases accompanies these processes.

Studies also showed that the mixture of Na_2SO_4 and $MgSO_4$ sulfate salts exhibited significantly higher levels of corrosion aggressiveness, resulting from the formation of a eutectic with a substantially lower melting point than the individual sulfates. This also reduces the viscosity of the liquid salt deposits, which intensifies the process of penetration into the porous structure of the TBC ceramic layer.

The introduction of V_2O_5 oxide into the corrosive environment rapidly accelerates the corrosion process of the tested TBC systems, regardless of their variant. This is due to the strong tendency

to form neodymium vanadate, as well as yttrium vanadates, in the case of two-phase composite coatings.

8.2 Future Work

Further planned work will include a detailed characterization of the microstructural phenomena associated with the decomposition of the $Nd_2Zr_2O_7$ pyrochlore phase into non-stoichiometric forms, induced by temperature and the processing environment. Particular emphasis will be placed on the role of yttrium oxide Y_2O_3, derived from the 8YSZ component. Its release from tetragonal ZrO_2 is assumed to cause the tetragonal-to-monoclinic phase transformation, as demonstrated by XRD studies. Simultaneously, free Y_2O_3 acts as a doping agent for the $Nd_2Zr_2O_7$ pyrochlore phase, replacing Nd^{3+} cations with smaller Y^{3+} cations. Consequently, the $r(Nd^{3+}, Y^{3+})/r(Zr^{4+})$ ratio decreases to below 1.46, indicating greater thermodynamic stability of fluorite-type phases. To verify this assumption, phase stability studies are planned for the systems $Nd_2Zr_2O_7$ + monoclinic ZrO_2, Nd_2Zr2O_7 + tetragonal 3% mol $Y_2O_3{\times}ZrO_2$, and $Nd_2Zr_2O_7$ + cubic 8% mol $Y_2O_3{\times}ZrO_2$. Phase composition studies are planned to be performed using XRD in powder systems, as well as studies utilising the capabilities of Raman spectroscopy.